Title
Gas Evolution Studies on Emerging Cathode Materials for Lithium-Ion Batteries

Author
Kaufman, Lori

Publication Date
2022

Peer reviewed|Thesis/dissertation

Gas Evolution Studies on Emerging Cathode Materials for Lithium-Ion Batteries

by

Lori Kaufman

A dissertation submitted in partial satisfaction of the

requirements for the degree of

in

Chemical Engineering

in the

Graduate Division

of the

University of California, Berkeley

Committee in charge:

Professor Bryan D. McCloskey, Chair
Professor Nitash Balsara
Professor Kristin Persson

Summer 2022

Gas Evolution Studies on Emerging Cathode Materials
for Lithium-Ion Batteries

Lori Kaufman

Abstract

Gas Evolution Studies on Emerging Cathode Materials
for Lithium-Ion Batteries

by

Lori Kaufman

Doctor of Philosophy in Chemical Engineering

University of California, Berkeley

Professor Bryan D. McCloskey, Chair

Lithium-ion batteries have had a huge societal impact in the last fifty years, playing an important role in the widespread availability of mobile electronics and with them unprecedented global access to information. Now as the effects of anthropogenic climate change have become evident in weather patterns across the globe, and therefore the impetus to address them even more dire, lithium-ion batteries again have the potential to change the world.

Once considered an antiquated technology, electric vehicles have had a massive resurgence in the past few decades, supported in a large part by developments in lithium-ion battery technology. First demonstrated in the Tesla Roadster (2008), lithium-ion batteries for electric vehicles are the first type of battery with the ability to rival fossil fuels in performance while drastically reducing emissions from the transportation sector.

Despite their adoption as the industry standard for electric vehicles, lithium-ion batteries still have inadequacies that need to be addressed before they can replace fossil fuels as the optimal vehicle power source. Principal among these issues is the inability to match the energy density of gasoline. This significant drawback is the origin of the phenomenon of range anxiety, in which consumers fear that the battery will run out of charge before reaching a refueling station, resulting in their vehicle becoming stranded. While the issue can be partially mitigated by adding more batteries to the vehicle, cost and weight considerations limit the effectiveness of this solution. Modifications to the chemistry of the battery itself will be required to address this problem while maintaining a low cost and weight.

As the limiting component in terms of energy density, the cathode has been the subject of intense research in recent years. In this dissertation, two major research branches in emerging cathode materials are addressed: lithium-excess and high-nickel. Both of these categories of cathode material use the same components as commercial materials (lithium, a combination of transition metals, and oxygen) with slight variations in their ratio, so they are expected to be ready for production at industrial scale within a shorter time frame of a few years as opposed to a few decades for those technologies that require a complete cathode redesign.

This work is unique in the field of battery research due to its use of gas evolution techniques, which measure gases evolved from a battery during or after operation. Conclusions can be drawn about the degradation mechanisms responsible for the observed outgassing based on the identity, amount, and state-of-charge at which gases are evolved. The two major sources of cathode instability addressed in this work are (i) cathode reactivity with the carbonate electrolyte, which often produces CO_2 gas and deposits degradation products onto the cathode surface; and (ii) inherent cathode instabilities at high voltage, which are often characterized by permanent alteration of the cathode structure via the oxidation of the oxide component of the cathode into O_2 gas.

After an introduction to energy storage research and the goals of this dissertation in Chapter 1, chapters 2 and 3 focus on lithium-excess cathode materials. These materials are designed to contain more lithium than can be compensated for by the transition metals, resulting in increased capacity and oxygen redox activity (a phenomenon previously seen in lithium-air batteries). Novel isotope tagging techniques and titration methods are also introduced. This work shows that stable oxygen redox can occur in lithium-excess materials but that oxidation of residual carbonate on the cathode surface triggers irreversible oxygen activity. Only irreversible oxygen activity is detected for Li_2MnO_3, a material that represents the maximum lithium to transition metal ratio while maintaining a layered structure. Further work is needed to determine whether stable manganese redox occurs in Li_2MnO_3, a process that could make Li_2MnO_3 a viable cathode material.

Chapters 4 and 5 focus on high-nickel cathode materials. The advantage of these materials is based on the superior charge compensation ability of nickel compared to other transition metals, resulting in enhanced capacity and attainable energy density. However, as a result of nickel's reactivity, they are structurally unstable, undergoing phase transitions that have consequences in terms of outgassing and cathode structure. This work shows that outgassing is closely linked with particle cracking, with the onset of gas evolution occurring at the same voltage at which cracks which originated inside the particle extend to the cathode/electrolyte interface. In addition, the unique capability of an ex-situ acid titration developed to study surface contaminants to separately detect contaminants located inside particles is demonstrated. Lastly, single crystal morphologies are addressed as a possible solution to structural instability in high-nickel materials. While the change in morphology partially mitigates cracking and outgassing, particle agglomerates show the same degradation issues as polycrystalline materials, with cracks propagating from stacking faults where two single crystal particles have merged. Additional studies are necessary to produce single crystal materials that are well-dispersed to take full advantage of their enhanced stability compared to polycrystalline materials.

While this work is rooted in scientific discovery more so than development of industrially relevant materials, it demonstrates that the commercialization of both of these types of emerging cathode materials is within reach. Gas evolution studies on these materials, as well as those that involve more drastic changes to the cathode structure, are integral to the progression of these technologies from ideas to practice.

To my parents, with grad-itude

Contents

List of Figures

List of Tables

Acknowledgments

I acknowledge the immense suffering of both humans and animals which, in the convoluted way of fate, has given me the opportunity to obtain a PhD. With this acknowledgement I also include my greatest wish, that my achievement of this degree might allow me to ease that suffering for those who come next.

1 Li-ion batteries and gas evolution techniques used to study them

1.1 Lithium-ion batteries

The Li-ion battery enables storage and transport of large amounts of energy in a compact, lightweight form. Today, such batteries are used to power virtually all mobile electronic devices. With improvements, batteries could enable the abundant availability of energy from intermittent renewable sources [1]. Li-ion batteries are especially promising for transportation applications such as electric vehicles because they deliver the most energy for their size and weight out of all currently available battery chemistries [2]. One remaining challenge in this area is to improve the energy density of Li-ion batteries even further to rival that of fossil fuels without compromising battery lifetime and reliability [3]. *

1.1.1 Li-ion battery components

The major components of a lithium-ion battery are the two electrodes (anode and cathode) and the electrolyte. The electrodes are each responsible for storing lithium, either in its neutral, metallic form or as a positive ion, for the anode and cathode, respectively. The electrolyte transports lithium ions between the two electrodes, either from the cathode to the anode during charge or from the anode to the cathode during discharge. Note that the cathode and anode are defined here as the positive and negative electrode, as has become standard in the battery community, rather than using the electrochemical definition based on the direction of the flow of current (in which case the same electrode would be called cathode or anode depending on whether the battery is being charged or discharged). Concurrently with the transport of lithium ions through the electrolyte, electrons are transported to or from the external circuit.

The state-of-the-art materials used are graphite for the anode, a liquid mixture of carbonates containing a lithium salt for the electrolyte, and layered metal oxide for the cathode (Figure 1.1). To increase power rates and energy density, cathodes and anodes are porous, being comprised of powders of their respective active materials and a high electronic conductivity carbon additive that are bound together using a polymer, typically poly(vinylidene fluoride). While each battery component has its own engineering challenges, the cathode is the focus of this work because it is the limiting factor in terms of reversible capacity (Table 1.1). The battery also includes a separator, which physically separates the two electrodes from each other, and two current collectors, each of which interfaces between an electrode and the external circuit. Separators are usually thin layers of plastics such as polypropylene.

*Portions of this chapter are adapted from the author's qualifying exam (presented August 22, 2019) and colloquium (presented February 16, 2022).

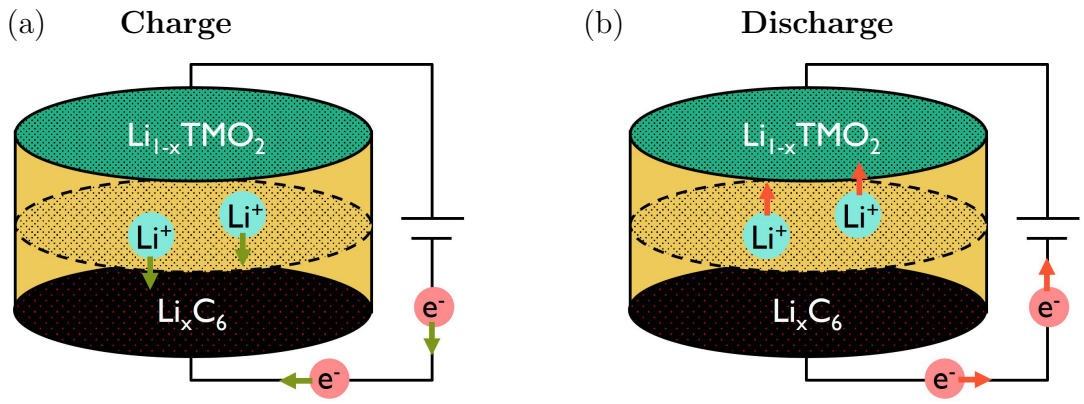

Figure 1.1: Schematics of battery charge (a) and discharge (b) showing a layered lithium transition metal oxide cathode (green), liquid electrolyte (yellow), and graphite anode (black) as well as the movement of lithium ions (blue) and electrons (pink).

Table 1.1: Typical reversible capacities for each electrode

Electrode	Reversible capacity
Anode (graphite)	350 µmol/g *
Cathode (metal oxide)	180-200 µmol/g *

* Values from [2]

Current collectors are made of metal sheets onto which the electrodes are cast; typically, anodes are cast onto copper foil and cathodes onto aluminum foil.

Lithium-ion cells can be found in many different form factors including the simpler coin cells and pouch cells as well as the more complex cylindrical cell commonly used in electric vehicles. All of these contain one or more layers of electrodes with separators between them. In this work, cells with one layer of each electrode with a separator in the middle are constructed as simple models for industrially relevant cells.

1.1.2 Function of the cathode

In modern Li-ion batteries, the cathode active material is a metal oxide in which the crystal structure composed of alternating layers of lithium, which allows facile lithium diffusion within the cathode material, and transition metal oxides, which compensate for the movement of lithium ions by changing oxidation state (Figure 1.2). This structure is described crystallographically as α-$NaFeO_2$ -type, a variation on the rocksalt structure (in which positive and negatively charged atoms alternate along each plane similar to the salt NaCl).

During charge, lithium ions are de-intercalated from the cathode:

$$\mathrm{LiTMO_2} \rightarrow x\mathrm{Li^+} + \mathrm{Li_{1-}}_x\mathrm{TMO_2} \tag{1.1}$$

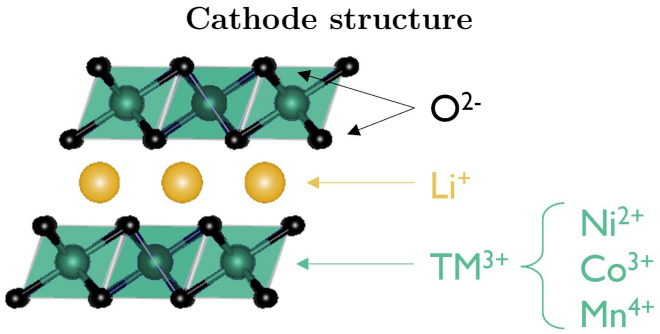

Figure 1.2: Schematic showing the location of oxygen (black), lithium (yellow) and transition metal (green) atoms in the layered NCM cathode structure. Image generated using the Materials Project [4].

Concurrently, one electron for each lithium ion is accepted from the external circuit and the two react at the anode to form neutral lithium, either stabilized within a host structure such as graphite (generalized as A in the equation) or as metallic lithium:

$$x\mathrm{Li}^+ + xe^- + x\mathrm{A} \rightarrow x\mathrm{LiA} \tag{1.2}$$

During discharge, the flow of ions is reversed and lithium ions are re-intercalated into the cathode:

$$x\mathrm{Li}^+ + \mathrm{Li}_{1-x}\mathrm{TMO}_2 \rightarrow \mathrm{LiTMO}_2 \tag{1.3}$$

Again, an anode process occurs as well: neutral lithium is broken into electrons and lithium ions, with the electron released to the external circuit and the lithium ion transported to the cathode:

$$x\mathrm{LiA} \rightarrow x\mathrm{Li}^+ + xe^- + x\mathrm{A} \tag{1.4}$$

The variable x is included in equations 1.1 through 1.4 to show that not all of the lithium initially available in the cathode can be reversibly transported between the electrodes due to the inherent structural instability of the cathode when most of the lithium has been removed. In an ideal cathode material, x remains close to one throughout extended cycling to achieve a high reversible capacity.

1.2 Emerging cathode materials

State-of-the art cathodes contain three transition metals: nickel, whose accessible oxidation states in the voltage range of operation include 2+, 3+ and 4+; cobalt, with accessible oxidation states 3+ and 4+; and manganese, which with only one accessible oxidation state of 4+ does not participate in charge compensation. This type of cathode, abbreviated NCM or NMC, was designed as a compromise between pure lithium metal oxides by combining the high energy density of $LiNiO_2$, the cycling stability of $LiCoO_2$, and the structural stability provided by the high oxidation-state manganese in Li_2MnO_3 (which does not show reversible capacity by itself). [5].

1.2.1 Lithium-excess cathode materials

One method to increase the capacity of an NMC cathode is to add additional lithium and adjust the proportion of the transition metals to contain more manganese. The amount of these two components is linked because the average transition metal charge must be 2+ to form a neutral compound together with the oxide, so adding additional lithium in the 1+ state necessitates adjusting the ratio of the other metals to a higher average oxidation state. Additional metals with higher accessible oxidation states have been studied as well as ways to facilitate Li-excess cathode materials, but these metals present their own obstacles [6].

The main advantage of Li-excess cathode materials is that the increased proportion of lithium yields a higher energy density because lithium is the component of the cathode that allows electron transfer [7, 8]. Interestingly, as a side effect of increasing both lithium and manganese content, the transition metals present in a Li-excess cathode material are insufficient to supply charge compensation for all of the lithium ions in the cathode material. As a result, the oxygen component also participates in charge compensation [9], resulting in the production of new oxygen species with oxidation states between 2- (lattice oxide) and 0 (oxygen gas) [10, 11]. The participation of oxygen in charge compensation is analogous to the operating mechanism of lithium-air batteries, where lithium peroxide is formed/oxidized during battery operation, which presents reactivity issues with the carbonate electrolyte typically used in Li-ion batteries [12, 13].

In chapters 2 and 3, Li-excess and pure Li_2MnO_3 cathode materials are studied to determine what oxygen activity occurs in these cathode materials and whether this activity results in increased electrolyte reactivity. In both cases, O_2 gas is evolved as a result of oxygen redox, resulting in irreversible changes to the cathode material as lost oxygen causes phase changes in the remaining structure. However, Li-excess cathode materials (which still contain other redox-active metals such as nickel and cobalt) also show another oxygen redox process resulting in the production of peroxo-like (O_2^{2-}) oxygen species, which can be reversibly oxidized back to lattice oxygen (O^{2-} or O_2^{4-}) in some cases. Lithium carbonate, which is present on the cathode because it is a precursor used in excess in synthesis and forms upon air exposure or reaction with the carbonate electrolyte, also plays an important role in the degradation processes in these materials as explained in detail in the next two chapters.

1.2.2 High-nickel cathode materials

Another method to increase the capacity of NMC materials is to adjust the proportion of the transition metals to contain more nickel. Nickel contains more accessible oxidation states in the electrolyte voltage stability window, so it provides higher capacity than Co or other metals [14]. However, increasing nickel content in NMC cathodes to a high percentage ($\geq$ 80%) causes the material to suffer from unique issues due to its structural instability [15]. Physical expansion and contraction that occurs during charge makes this type of material susceptible to micro-cracking [16], which results in decreased capacity due to electrolyte reactions within the cracks as well as the electrical disconnection of active material over extended cycling [17].

In chapters 4 and 5, the degradation mechanisms of high-Ni cathode materials are investigated. The materials studied in chapter 4 have coatings and dopants applied to stabilize the physical structure, while those studied in chapter 5 have a single crystal morphology designed to prevent micro-cracking. However, both types of material still show gas evolution and micro-crack development. Again, surface contaminant Li_2CO_3 factors into the dominant degradation processes, as it can be deposited on the outside surface or inside micro-cracks as a result of electrolyte degradation, likely resulting in additional structural instability and possibly also producing pressurized CO_2 gas inside the cracks. These two chapters demonstrate that despite the strong push from industry to commercialize high-Ni cathode materials, additional methods to mitigate degradation from outgassing and micro-cracking are still needed.

1.3 Gas evolution techniques

While cycling data and spectroscopic measurements have proved invaluable in the study of emerging cathode materials, gas evolution techniques have provided the key to further understanding of degradation processes in these materials. Initially developed by McCloskey et al. to study lithium-air batteries, our differential electrochemical mass spectrometry (DEMS) capabilities can also be used to study lithium-ion battery systems. DEMS systems modified to study lithium-ion systems [18, 19] were used extensively in this work. In order to detect the gases evolved from a battery in real time, the cell is designed with a spacer to create a controlled volume of headspace as well as two capillaries used as a gas inlet and outlet. The cell also contains upper and lower electrical contacts connected to the cathode and anode, respectively, which are used by the potentiostat to control the voltage or current. Meanwhile, evolved gas is contained in the headspace for a set amount of time (usually ten minutes) and then the headspace is opened to a coil with a set volume (not shown). The cell is closed off after the gas from the headspace fills the coil so as not to pull vacuum on the headspace itself, and the gas in the coil is analyzed using the mass spectrometer. The setup of the DEMS system is depicted in Figure 1.3a.

In addition to DEMS, its counterpart technique of titration mass spectrometry (TiMS) has also been crucial to many of the discoveries presented in this work. The same gas

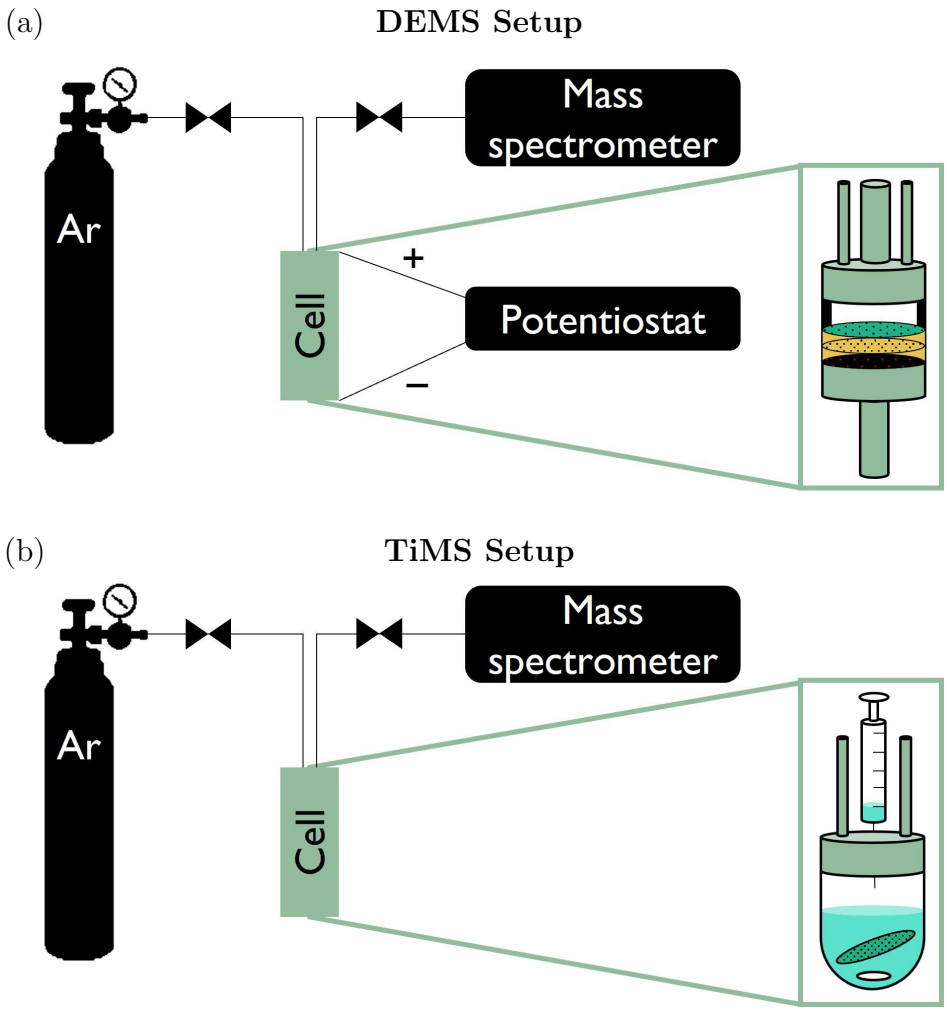

Figure 1.3: Diagrams for DEMS (a) and TiMS (b) setup showing the gas handling system on the left and a close-up of the cell configuration on the right for both techniques.

handling system is used, but the potentiostat is unnecessary because TiMS is a chemical technique. After baselines are recorded for each mass channel, acid is injected into a sealed glass vessel containing the electrode of interest and a stir bar. The gases resulting from the reaction of the acid and the electrode components are detected using the mass spectrometer. Since the rate of diffusion of gas to the mass spectrometer is slow due to the large headspace volume as compared to the carrier gas flow rate, gas might evolve for many hours after acid is injected even if the reaction occurs quite rapidly. The setup of the TiMS system is depicted in Figure 1.3b. This technique is still being developed and its capabilities greatly expanded by McCloskey lab members.

2 Surface lithium carbonate influences electrolyte degradation via reactive oxygen attack in lithium-excess cathode materials

2.1 Abstract

Lithium-excess layered oxide cathode materials ($Li_{(1+x)}TM_{(1-x)}O_2$) for lithium-ion batteries achieve high specific capacities ($\geq$250 mAh/g) via redox participation of both transition metals and oxygen anions. While oxygen is initially present as O^{2-} in the cathode, oxidized oxygen species such as peroxo-like oxygen (O_2^{2-}) and oxygen gas (O_2) are known to form on charge. In this work, differential electrochemical mass spectrometry (DEMS) is used to study the mechanisms by which lithium carbonate, a common impurity, influences how these oxygen species form and react within the battery. We first show, in agreement with prior studies, that Li_2CO_3 oxidizes electrochemically on charge to evolve CO_2, but not O_2, implying that reactive oxygen species form instead that then react with cell components to form non-volatile products. To study the effect of Li_2CO_3 on degradation processes at the cathode surface, Li-excess cathode material $Li_{1.17}(Ni_{0.2}Mn_{0.6}Co_{0.2})_{0.83}O_2$ (NMC) is synthesized using a method that prevents formation of carbonate impurities in the synthesized material. Isotopically tagged lithium carbonate is then deposited on the NMC surface through controlled exposure to $^{13}CO_2$ or $C^{18}O_2$ gas. DEMS results show that when lithium carbonate is present on the cathode surface, organic fragments containing diatomic oxygen are formed on the cathode surface during charge above 4.2 V vs. Li/Li^+. Isotopic analysis indicates that the diatomic oxygen within these fragments primarily originates from the NMC lattice, with only a minor fraction originating from the Li_2CO_3 itself. Our results therefore suggest that reactive oxygen release from the NMC lattice is triggered by the oxidation of surface lithium carbonate.*

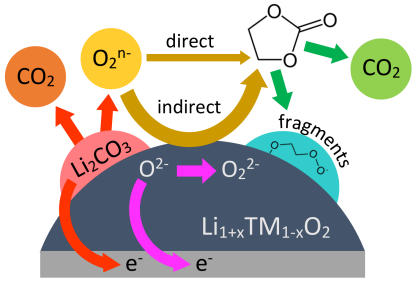

*This chapter adapted with permission from previously published work in: Kaufman, L. A. and McCloskey, B. D. *Chem. Mater.* **33**, 4170–4176 (2021).

2.2 Introduction

The phenomenon of oxygen redox in lithium-excess cathode materials for lithium-ion batteries has been the subject of many studies [20–25]. Though this phenomenon offers the intriguing possibility of increased energy density by mixing traditional transition metal redox with oxygen electrochemistry, it also introduces unique degradation pathways that inhibit the long-term cyclability of lithium-excess cathode materials. Capacity and voltage fade are known to occur in these materials, accompanied in early cycles by the evolution of oxygen and carbon dioxide gases. [7, 26, 27] Prior studies indicate that evolution of these gases is a result of processes occurring at the cathode-electrolyte interface that cause degradation of the carbonate electrolyte. [9–11, 28]

Many possible sources exist for the observed gas evolution. To compensate for the removal of lithium ions, up to two electrons per oxygen can be removed from the transition metal oxide cathode during charge, which can produce oxygen gas at high degrees of delithiation. When considering carbon dioxide evolution, sources of carbon include the conductive carbon and binder in the cathode, the carbonate electrolyte, and residual lithium carbonate. Each of these sources would need to be oxidized to produce CO_2 gas, either through direct electrochemical oxidation or through attack from reactive species produced at high voltage. It is important to differentiate between these sources in order to determine the mechanism(s) responsible for causing gas evolution in lithium-excess lithium-ion batteries.

Previous studies have shown that there is significant involvement of lithium carbonate in gas-evolving processes [29–31]. In theory, lithium carbonate oxidizes starting at 3.8 V vs. Li/Li^+ via equation 2.1:

$$Li_2CO_3 \rightarrow 2Li^+ + 2e^- + CO_2 + \frac{1}{2}O_2 \tag{2.1}$$

Our lab has previously used isotopic tagging techniques to show that residual lithium carbonate contributes significantly to CO_2 evolution during the first charge in lithium-excess [29] and lithium-stoichiometric [30] NMC cathodes. Prior work by McCloskey et al. [13, 32] showed the same process above 4.0 V vs. Li/Li^+ in lithium-air batteries. The absence of O_2 evolution coincident with CO_2 evolution in all of these studies leaves open the question of what other oxygenated species might be produced from Li_2CO_3 oxidation. Recent work used a chemical probe, 9.10-dimethylanthracene (DMA), to show that lithium carbonate oxidation produces singlet oxygen in an ether electrolyte. [33] While this result does not prove that the same process occurs in carbonate electrolytes, both singlet oxygen [34] and superoxide [35] are highly reactive towards carbonate electrolytes as demonstrated by computational studies. Other laboratories (e.g., Gasteiger et al.[36]) have suggested that Li_2CO_3 does not oxidize electrochemically at all, and instead only evolves CO_2 once the electrolyte degrades to form H^+ during oxidation. Clearly, there are many open questions that remain regarding the influence of Li_2CO_3 on electrolyte stability.

When using traditional synthesis and handling methods, cathode active materials universally have a residual 0.1-0.5 wt% carbonate content [37], complicating assignment of CO_2 evolution mechanisms. Here, a lithium-excess cathode material, $Li_{1.17}(Ni_{0.2}Mn_{0.6}Co_{0.2})_{0.83}O_2$ (NMC), is synthesized with the express objective of minimizing residual lithium carbonate content. After synthesis, controlled amounts of lithium carbonate can be introduced on the NMC material surface via via CO_2 gas exposure, allowing the creation of materials that are identical except for their residual lithium carbonate content. These materials are charged at 0.1C while employing differential electrochemical mass spectrometry (DEMS) to analyze gas evolution in real time. Together with acid titrations of extracted cathodes, these data show experimental evidence for electrolyte degradation caused by reactive oxygen that is correlated with the presence of lithium carbonate but primarily originates from the transitional metal oxide lattice. We suggest a mechanism for this process that is consistent with computational studies.

2.3 Experimental methods

2.3.1 Synthesis procedure

$Li_{1.17}(Ni_{0.2}Mn_{0.6}Co_{0.2})_{0.83}O_2$ (NMC) is synthesized using lithium hydroxide as a lithium precursor [38] instead of the more common lithium carbonate [39]. Lithium hydroxide and transition metal acetates were dissolved in water along with citric acid and ammonium hydroxide. The solution was heated to 100°C to yield a gel and then a powder as water evaporates off. This procedure was completed using a Schlenk line under a nitrogen atmosphere in order to prevent formation of lithium carbonate via reaction of the cathode material with the air.

The NMC powder obtained from the wet synthesis was subjected to two heating steps. Since the environment must be oxygen-rich in order to oxidize the transition metals in the material, dry air (a combination of nitrogen and oxygen only) was used instead of exposing the material to atmosphere. The material was first heated to 600°C to remove remaining organics, then to 900°C to form the final crystalline material [40]. NMC produced using this procedure showed the expected transition metal ratio, a particle size of around 250 nm, and an expected mixture of C2/m and $R\bar{3}m$ phases (Figure 2.1). No Li_2CO_3 was detected during an acid titration (see Offgassing Analysis section below) of the as-synthesized material. The resolution of our acid titration method is roughly 0.01 wt%.

2.3.2 CO_2 exposure

In order to deposit Li_2CO_3 on the cathode surface without allowing degradation from air exposure, samples of around 100 mg NMC powder were exposed to pure CO_2 at room temperature inside a tube furnace. Isotopically-tagged $^{13}CO_2$ (99% ^{13}C) and $C^{18}O_2$ gas (95% ^{18}O) were both used in this study to track decomposition of lithium carbonate separately from other processes. Various exposure times were tested (Table 2.1) and the lowest exposure time (two hours) chosen in order to affect the least amount of change on the electrochemistry of the NMC material.

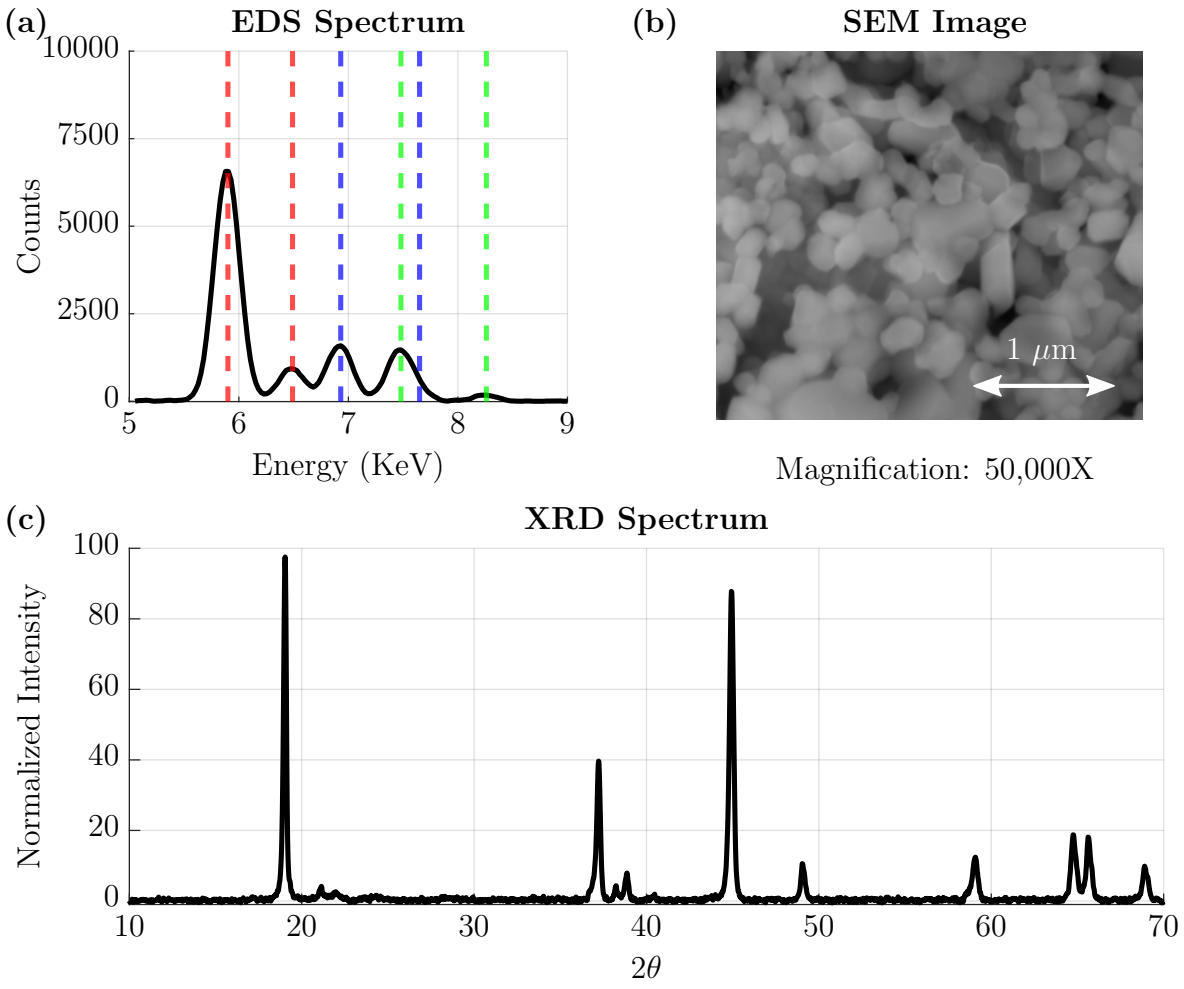

Figure 2.1: Characterization of the synthesized Li-excess layered cathode material $Li_{1.17}(Ni_{0.2}Mn_{0.6}Co_{0.2})_{0.83}O_2$ (NMC). The EDS spectrum (a) shows the presence of Mn (red lines), Co (blue lines), and Ni (green lines) in the sample at a ratio of 60:20:20. The SEM image (b) shows a fairly homogeneous particle size of around 250 nm. The XRD spectrum (c) shows the coexistence of C2/m ($Li(Li_{1/3}Mn_{2/3})O_2$) and R$\bar{3}$m ($LiTMO_2$) phases as expected for a lithium-excess layered material [7]. Intensity data was normalized to the peak at 18°. Carbonate titrations show a Li_2CO_3 content lower than the measurement threshold of 0.01 wt% in this material, an order of magnitude less than in commercial materials [31].

Table 2.1: Li_2CO_3 Deposition as a Function of CO_2 Exposure Time

CO_2 Exposure Time	Li_2CO_3 Deposited*
0 hours	0 wt%
2 hours	0.015 wt%
4 hours	0.069 wt%
6 hours	0.071 wt%

* Li_2CO_3 was measured via acid titration (see Offgassing Analysis section).

Table 2.2: Reactivity of simple Li-containing species with CO_2 (2-hour exposure)

Material	Li Reacted
LiOH	50 mol%
Li_2O	10 mol%

Control 2-hour CO_2-exposure experiments were performed on pure LiOH and Li_2O powders to represent lithium-containing surface contaminants and lattice lithium, respectively (Table 2.2). We believe that the addition of surface Li_2CO_3 does not significantly alter the lithium content of the NMC lattice because the lithium-containing surface contaminants, such as LiOH and Li_2O, are both easier to access and more reactive towards CO_2 gas. In addition, we would expect a reduction in capacity if there was significant delithiation of the lattice due to this procedure, which is not the case, as will be discussed in the results section.

2.3.3 Cell construction

Swagelok-type cells were assembled with cathodes composed of 90 wt% active material, 5 wt% carbon black (Super P), and 5 wt% polyvinylene fluoride binder coated onto stainless steel mesh and lithium metal anodes. The electrolyte used was 1 M $LiPF_6$ in a 1:1 mixture by weight of ethylene carbonate and diethyl carbonate (Gotion). Cells were assembled with two separators, one polypropylene (Celgard 2500) and one glass fiber (Whatman), with the Celgard in direct contact with the cathode. Lithium metal (FMC) was used as the anode. AvCarb P50 carbon gas diffusion substrates were purchased from the Fuel Cell Store.

For the three-separator cell used to study the possible chemical evolution of CO_2 from Li_2CO_3 induced by electrolyte degradation, 99% ^{13}C-tagged lithium carbonate was dissolved in water and pipetted onto a glass fiber separator. Heat and vacuum were used to ensure that all of the water was evaporated off. After removal of the water, the $Li_2^{13}CO_3$ powder was visible in the glass fiber matrix. Approximately 1 mg of $Li_2^{13}CO_3$ was added as confirmed by acid titration (additional amounts resulted in a separator too stiff to handle without breaking). The $Li_2^{13}CO_3$-impregnated glass fiber separator was placed between two polypropylene separators in order to electrically isolate the $Li_2^{13}CO_3$ from both electrodes.

2.3.4 Offgassing analysis

Differential electrochemical mass spectrometry (DEMS) is used to detect gases evolved from a battery during cycling [12]. In order to achieve quantifiable results, calibrations are performed to relate the ion current detected by the mass spectrometer to the partial pressure of the gas of interest in argon. Additionally, a similar setup can be used to monitor gases evolved during an acid titration of cathodes extracted from cycled batteries [30]. During these titrations, in which an extracted cathode is placed in a vessel attached to the DEMS gas handling unit, followed by injection of 10 M H_2SO_4, carbonates on the cathode surface react with acid to produce CO_2 gas:

$$Li_2CO_3 + 2H^+ \rightarrow 2Li^+ + H_2O + CO_2 \tag{2.2}$$

In addition, peroxo-like species (O_2^{2-}) on the cathode react to form O_2 gas in a similar fashion to the reaction between lithium peroxide and acid:

$$Li_2O_2 + 2H^+ \rightarrow 2Li^+ + H_2O + \frac{1}{2}O_2 \tag{2.3}$$

Control experiments confirm that these surface species react to form stoichiometric amounts of gas as detected by the mass spectrometer. [29]

2.4 Results and discussion

2.4.1 Gas evolution from Li_2CO_3

In order to confirm that lithium carbonate electrochemically oxidizes on charge to form CO_2 but not O_2 gas, cathodes were made with lithium carbonate as the only active material. These cathodes consisted of 10% lithium carbonate, 10% polyvinylene fluoride (PVdF) binder, and 80% conductive carbon (Super P) by weight. Two isotopically labeled variants of Li_2CO_3 were used in this study, as described below, to confirm the origin of the O and C in evolved CO_2. Cells were assembled using a Li metal counter electrode and 1M $LiPF_6$ in 1:1 ethylene carbonate:diethyl carbonate (EC:DEC) as described in the Experimental Methods section. In order to mimic the charge protocol used for NMC materials, a lithium carbonate cathode with 7% ^{18}O content (approximately 15:1 mol:mol ratio of ^{16}O:^{18}O) was charged at a constant current of 0.1C based on the theoretical 2 e^- per Li_2CO_3 capacity (as shown in equation 2.1) to 4.8 V vs. Li/Li^+, after which the voltage was held at 4.8 V and the current allowed to decay. The evolution of CO_2 follows the same shape as the current (Figure 2.2a) with a ratio of approximately $2e^-$ per CO_2. The constant ratio of 15:1 between $C^{16}O_2$ and $C^{18}O_2$ confirms that lithium carbonate, rather than electrolyte oxidation, is the primary source of CO_2 evolution throughout both the constant current and constant voltage portions of the charge.

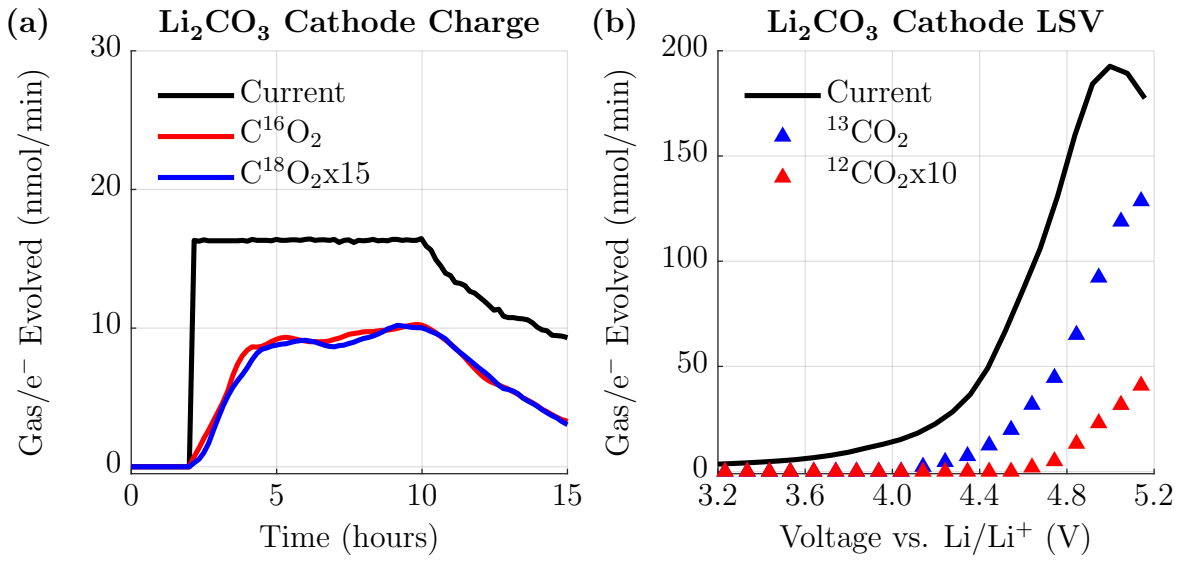

Figure 2.2: Current and CO_2 gas evolution for a lithium carbonate cathode during a 0.1C constant current charge followed by a voltage hold at 4.8 V vs. Li/Li^+ (a) and 10 mV/min linear sweep voltammetry to 5.2 V vs. Li/Li^+ (b). Both show a roughly $2e^-/CO_2$ process based on the CO_2 evolved from lithium carbonate, which is distinguished from other sources using isotope tagging (7 mol% ^{18}O in panel a and 99 mol% ^{13}C in panel b).

In order to clarify the voltage at which CO_2 evolution begins on charge, a 99% ^{13}C labeled lithium carbonate cathode was charged using linear sweep voltammetry at a rate of 10 mV/min from 3.2 to 5.2 V vs. Li/Li^+ (Figure 2.2b). $^{13}CO_2$ evolves in tandem with the current at a ratio of approximately $2e^-$ per CO_2 starting around 4.0 V vs. Li/Li^+. In contrast, evolution of $^{12}CO_2$ at $m/z = 44$ begins around 4.6 V vs. Li/Li^+, suggesting that lithium carbonate degradation begins at a significantly lower voltage than electrolyte degradation. No oxygen evolution was detected in either experiment. Of course, it is possible that CO_2 evolution from lithium carbonate is a result of a chemical reaction with protons formed via ethylene carbonate dehydrogenation rather than direct electrochemical oxidation. In fact, ethylene carbonate dehydrogenation has been observed at NMC811 surfaces at potentials as low as 3.8 V vs. Li/Li^+ [41]. We now discuss additional controls to show that this mechanism does not substantively contribute to CO_2 evolution from lithium carbonate at carbon electrodes, and therefore confirm that direct electrochemical oxidation of lithium carbonate occurs in carbonate-based electrolytes.

Additional control experiments were run using carbon cathodes to confirm that the CO_2 evolved starting around 4.0 V vs. Li/Li^+ is from electrochemical lithium carbonate oxidation rather than a chemical reaction with protons formed from electrolyte degradation. A 10 mV/min linear sweep voltammetry run on a P50 carbon cathode (without added Li_2CO_3) shows no $^{13}CO_2$ evolution, as expected, but $^{12}CO_2$ evolves starting around 4.8 vs. Li/Li^+ (Figure 2.3a). This experiment shows that little current or gas is generated without the

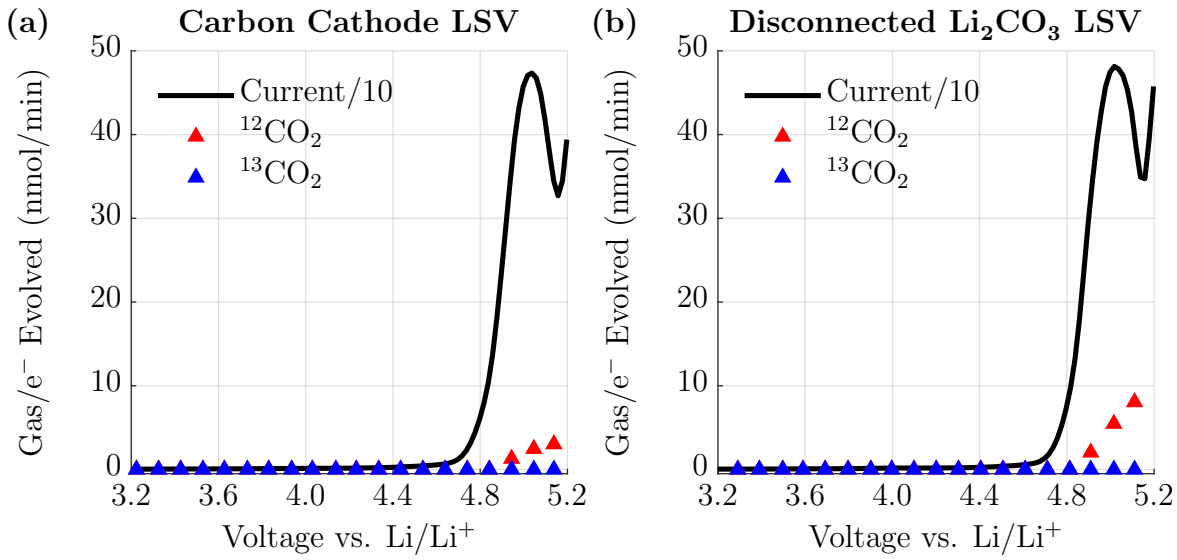

Figure 2.3: Linear sweep voltammetry at a porous carbon cathode (a) and a porous carbon cathode with 99% ^{13}C-labeled lithium carbonate contained within the middle separator of a three-separator cell such that it is electrically isolated (b). In both cases, CO_2 evolution occurs starting at 4.8 V vs. Li/Li$^+$ as a result of electrolyte degradation, in contrast to the CO_2 evolution at lower voltages as a result of lithium carbonate degradation as confirmed by isotope labeling in Figure 2.2.

presence of Li_2CO_3 below 4.8 V vs. Li/Li$^+$, suggesting that the $^{13}CO_2$ evolution observed starting at 4.0 V vs. Li/Li$^+$ in Figure 2.2b originates from direct electrochemical oxidation of lithium carbonate. To examine this finding further, a three-separator cell was constructed in which ^{13}C-labeled lithium carbonate was dissolved into a glass fiber separator, which was then sandwiched between two polypropylene separators. This configuration disallows electrical contact between the lithium carbonate and cathode, but allows any species formed at the cathode to diffuse to the lithium carbonate through the electrolyte. In this cell configuration, $^{12}CO_2$ evolution is observed starting at around 4.8 V vs. Li/Li$^+$, but no $^{13}CO_2$ occurs, verifying that lithium carbonate decomposes electrochemically when in direct electric contact with the electrode, and not chemically due to proton evolution from electrolyte degradation, on charge (Figure 2.3b). Again, no oxygen evolution was detected in either experiment. Note that hydrogen evolution was observed in both of these experiments starting around 4.8 V vs. Li/Li$^+$ coincident with CO_2 from electrolyte oxidation (Figure S1), implying that protons are formed as a result of electrolyte degradation and react at the anode to form hydrogen gas. However, this high voltage process clearly cannot account for the lower voltage evolution of CO_2 from lithium carbonate shown in Figure 2.2b, supporting the conclusion that lithium carbonate decomposes via electrochemical oxidation.

2.4.2 Control of surface Li_2CO_3 content on NMC

Lithium-excess NMC was synthesized with the express goal of minimizing residual lithium carbonate. The synthesis was performed (as described in the Experimental methods section) in an air-free environment in order to prevent H_2O and CO_2 exposure, which are known to cause deposition of new surface species and reduce cell performance in high-Ni [42, 43] and Li-excess (Figure S2) materials. In order to separately track decomposition of lithium carbonate versus that of the electrolyte or conductive carbon, isotopically tagged lithium carbonate is deposited on the cathode surface in a method similar to that used by Hatsukade et al. [43] via exposure to either $^{13}CO_2$ (99% ^{13}C) or $C^{18}O_2$ gas (95% ^{18}O). Since these cathode materials are synthesized with the express goal of minimizing residual lithium carbonate, a large proportion of the surface carbonate (the as-prepared material contained no quantifiable Li_2CO_3, with a measurement threshold of 0.01 wt%) is isotopically tagged after CO_2 exposure. Acid titration of pristine cathode powders after CO_2 exposure show that a measurable quantity of $Li_2C^{18}O_3$ is added and can be controlled using exposure time (Table 2.1).

The first cycle charge capacity and voltage profiles of the NMC material are not significantly altered by a two-hour CO_2 exposure (Figure 2.4a). Gas evolution data shows slight differences between the pristine materials and those exposed to CO_2 (Figure 2.4b-d). O_2 evolution (m/z = 32) from the NMC lattice has a slightly earlier onset in the CO_2-exposed material (Figure 2.4b). CO_2 evolution originating from electrolyte degradation (Figure 2.4c, m/z = 44) and ^{18}O-labeled lithium carbonate degradation (Figure 2.4d, m/z = 46+48) are notably higher for the CO_2-exposed sample, with the former implying that lithium carbonate oxidation results in enhanced electrolyte degradation, and the latter providing additional evidence of direct electrochemical lithium carbonate oxidation, both in agreement with our prior studies [37].

2.4.3 Observation of electrolyte fragments containing O_2 via acid titration

Acid titration of cathodes extracted from charged cells allows for quantification of solid carbonate surface species on the cathode as well as peroxo-like oxygen that results from lattice oxide oxidation [29–31]. If either of these species are present, they will evolve CO_2 (carbonate) or O_2 (peroxo-like oxygen) gas when exposed to strong acid via equations 2.2 and 2.3 (see Experimental Methods section).

We note that while equation 2.3 is written for lithium peroxide, any oxide oxidation will result in a stoichiometric equivalent of oxygen gas evolution during the titration as shown in the equation. For these measurements, we compare a pristine NMC sample to one that has been exposed to ^{13}C-labeled CO_2 for two hours. Titrations confirm that carbonates and peroxo-like oxygen build up on the cathode during charge (Figure 2.5), with slightly more of each species deposited on the CO_2-exposed NMC. The increasing amount of surface carbonates (Figure 2.5a) detected in both materials is likely due to electrolyte degradation processes that evolve CO_2 at similar potentials, as shown in Figure 2.4c. Note that ^{13}C-labeled carbonate was partially removed from the surface during charge, evolving CO_2 gas

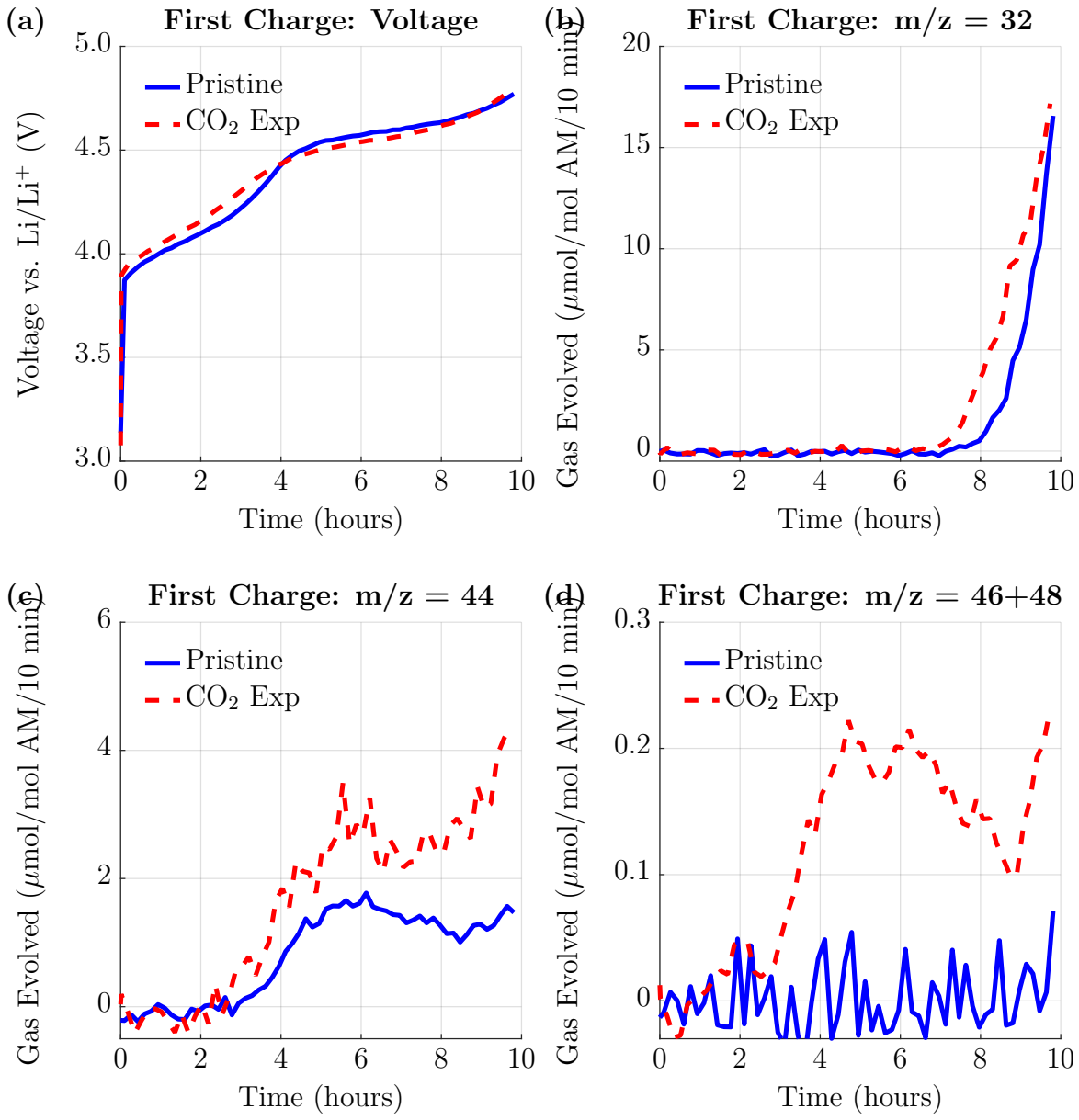

Figure 2.4: Gas evolution during first charge at 0.1C for pristine (blue) and $C^{18}O_2$ gas exposed (red) NMC samples. While the overall capacity and voltage profiles are similar between samples (a), there are slight alterations to the gas evolution due to the deposition of $Li_2C^{18}O_3$ on the surface including a slight lowering of the onset potential of oxygen evolution (b), an increase in the amount of $C^{16}O_2$ evolution (c), and the appearance of $C^{18}O_2$ evolution (d) which approximately mirrors the pattern of $C^{16}O_2$ evolution.

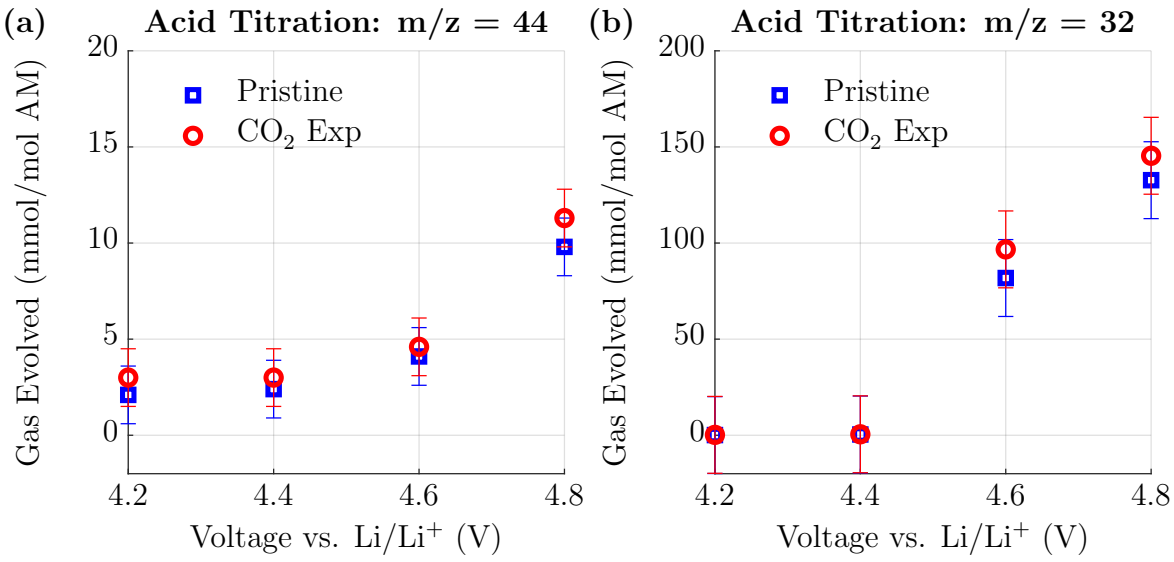

Figure 2.5: Gas evolution during acid titration at m/z = 44 (a) and m/z = 32 (b) showing the amount of surface carbonates and peroxo-like oxygen, respectively, on the cathode after 0.1C charge to various voltages for the pristine material (blue squares) and the material after exposure to CO_2 gas (red circles). These data show slight to no change in electrolyte degradation products deposited on each cathode. Error bars are based on three separate titrations after charge to 4.8 V vs. Li/Li^+.

as shown in Figure 2.4d, and not deposited back onto the surface (Figure S3). Additionally, a linear increase is observed in surface peroxo-like oxygen formation above 4.4 V vs. Li/Li^+ (Figure 2.5b). From these values, we calculate that the charge capacity above 4.4 V vs. Li/Li^+ can be entirely attributed to the formation of peroxo-like oxygen (Tables 2.3 and 2.4), in agreement with our prior studies [31].

Interestingly, additional surface species at m/z = 47 and 77 are detected during acid titration for the CO_2-exposed cathodes starting at 4.4 V vs. Li/Li^+ (Figure 2.6). These are the only signals observed after acid titration within the scan range of m/z = 1 to 80 that are not attributable to O_2, CO_2, or their fragments. Cross-referencing the atoms present in the system with the m/z ratios detected yields most probable identities for both m/z= 47 and 77, each of which consist of electrolyte fragments attached to diatomic oxygen (Figure 2.7). While theoretical studies have predicted that carbonate solvents (particularly EC) are susceptible to attack by reactive oxygen species [34, 35], these fragments provide the first direct experimental evidence for oxygen attack on the electrolyte. We propose the mechanism shown in Figure 2.8 to explain the detection of these fragments after the addition of acid.

These electrolyte fragments are expected to be quite unstable, so it is unsurprising that the detected signals show high variation from sample to sample and low signal-to-noise ratios. However, it is clear that the formation of these fragments is influenced by surface lithium

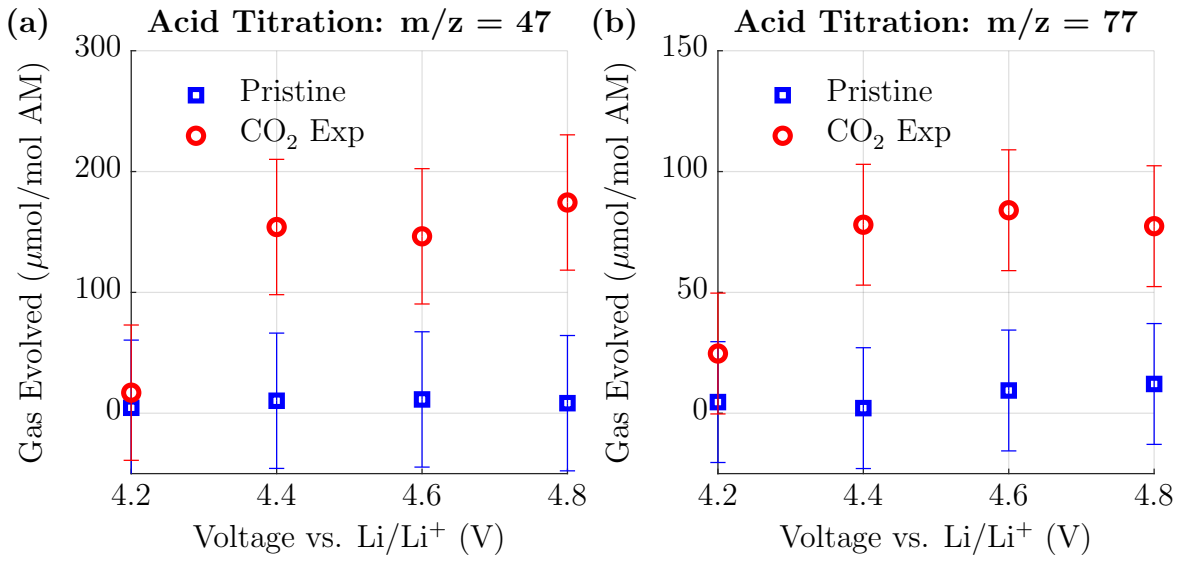

Figure 2.6: Gas evolution at m/z = 47 (a) and m/z = 77 (b) during acid titration of cathodes extracted after 0.1C charge to various voltages for the pristine NMC (blue squares) and the NMC material after exposure to CO_2 gas (red circles). The only species with these masses that can be present in the system consist of electrolyte fragments attached to diatomic oxygen. Error bars are based on three separate titrations after charge to 4.8 V vs. Li/Li^+.

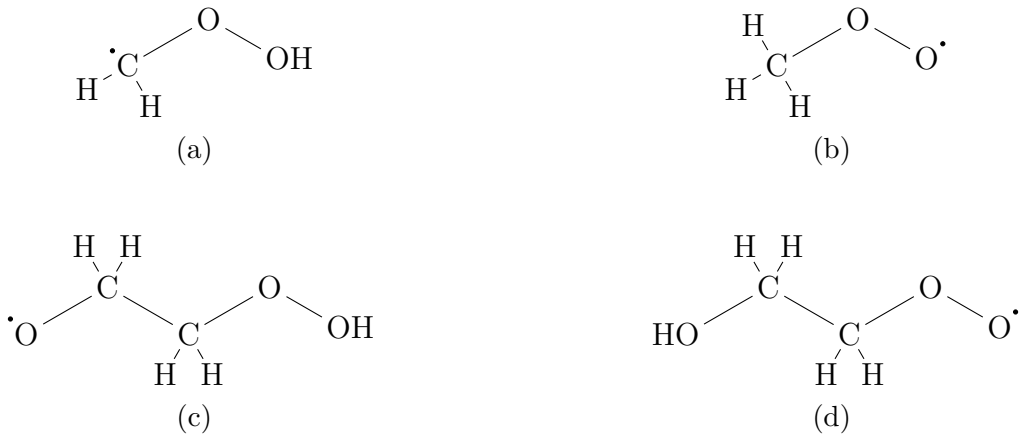

Figure 2.7: Possible configurations for the species at m/z = 47 (a and b) and m/z = 77 (c and d). In all cases, the species consist of electrolyte fragments bonded to diatomic oxygen.

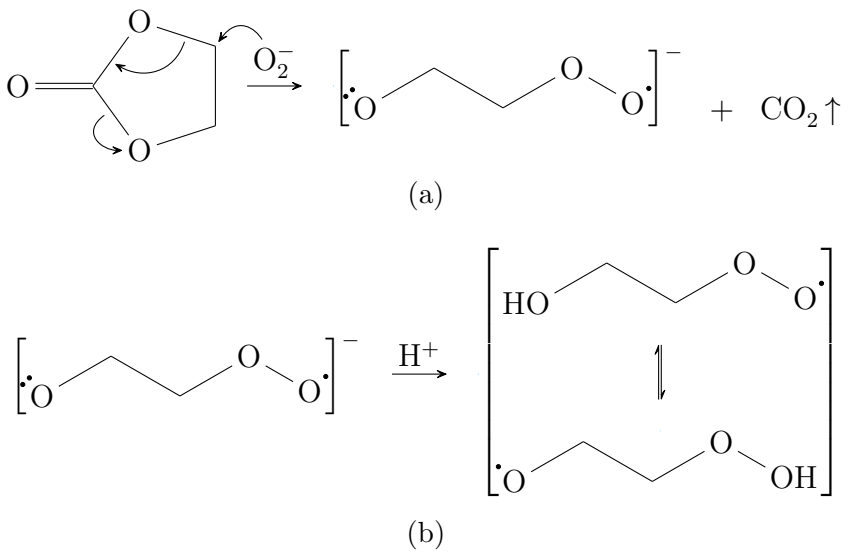

Figure 2.8: Proposed mechanism for production of the species detected at m/z = 77 after charge and acid titration. Reactive oxygen species react with electrolyte component ethylene carbonate (a) to release CO_2 gas and a surface-bound species. Acid titration (b) causes release of the species from the surface. Note that the species detected at m/z = 47 is expected to be a major fragment of this species as shown in Figure 2.7 (a) and (c).

carbonate because of the significant increase in signals at m/z = 47 and 77 in the CO_2-exposed sample as compared to the pristine sample. Additionally, in $C^{18}O_2$-exposed samples, the appearance of new signals at m/z = 49 and 79 are observed at much higher amounts than in the pristine samples (Figure 2.9). These signals represent the same fragments but with one oxygen isotopically labeled with ^{18}O, for which $Li_2C^{18}O_3$ is the only source. Oddly, no signal was observed at m/z = 51 and 81, implying a complex interaction of reactive oxygen from lithium carbonate oxidation with oxygen in the NMC lattice as opposed to direct electrolyte attack by lithium carbonate oxidation products. It is worth noting that no such electrolyte fragments were observed after acid titration of cathodes similar to those studied in Figure 2.2, which only contain carbon, binder, and Li_2CO_3. Combined, these observations suggest that while the deposition of Li_2CO_3 on NMC results in enhanced reactive oxygen release, most of this oxygen originates from the NMC lattice and not Li_2CO_3 itself.

While the oxidation state of the reactive oxygen involved in this reaction has not been directly detected, the mechanism implies it to be superoxide. Recent computational work [44] corroborates this theory, suggesting that a superoxide-like moiety is produced during lithium carbonate decomposition and then decays into peroxide and singlet oxygen. This work suggests that while various forms of oxygen are present in the system including peroxo-like oxygen resulting from lattice oxygen redox, reactive oxygen produced via lithium carbonate oxidation is the trigger for electrolyte degradation processes.

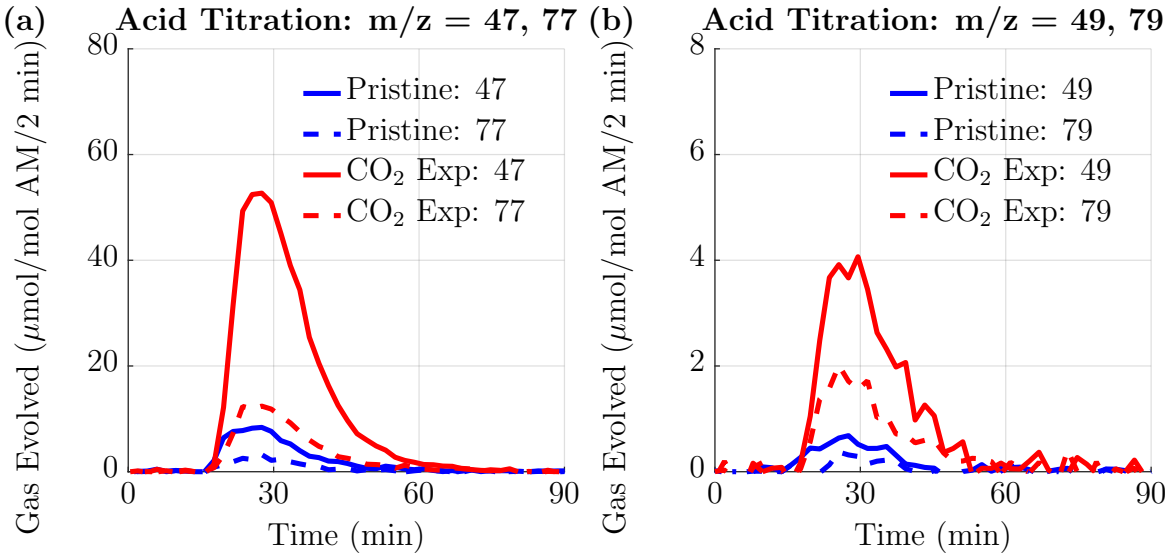

Figure 2.9: Gas evolution during acid titration at m/z = 47 (solid line) and m/z = 77 (dotted line) as well as corresponding ^{18}O-containing species m/z = 49 (solid line) and m/z = 79 (dotted line) for pristine (blue) and $C^{18}O_2$ gas exposed (red) samples. Samples were charged at 0.1C and held at 4.8V until the current decayed to 5% of the initial current. Exposure to $C^{18}O_2$ increases electrolyte fragments containing diatomic oxygen on the cathode surface including those containing ^{18}O, indicating complex involvement of $Li_2C^{18}O_3$ during charge.

2.5 Conclusion

In this work, controlled addition of lithium carbonate to Li-excess NMC cathodes via CO_2 exposure has been shown to promote electrolyte degradation processes that result in the formation of detectable electrolyte fragments on the cathode surface. Control experiments confirm that the degradation of lithium carbonate is electrochemical, not chemical, and that it produces a reactive oxygen species other than oxygen gas. The oxygen species produced as a result of electrochemical lithium carbonate oxidation participates both directly and indirectly in forming electrolyte degradation products as demonstrated using isotopic tags.

The mechanism of interaction between electrochemical lithium carbonate oxidation and bulk oxygen redox remains unclear, and it appears likely that reactive oxygen species from both the oxide surface of the NMC cathode and lithium carbonate participate in electrolyte degradation processes in Li-excess NMC materials. The mechanism by which lithium carbonate oxidation triggers instability in the lattice is unknown, but we propose two possible routes for this interaction: 1) removal of lithium carbonate from the surface via oxidation leaves behind an NMC surface from which Li and O have been removed, which may be unstable; or 2) reactive oxygen generated by lithium carbonate oxidation catalyzes a process that destabilizes the NMC surface. The first route seems unlikely given that other work [45, 46] has shown that removal of Li and O from the surface of a Li-excess cathode material

actually results in better stability. Therefore, we believe the second route is more likely the cause of the destabilization of the NMC surface. We conjecture that the mechanism behind this process is similar to the one proposed by Houchins et al. [44] but where the direct route to electrolyte degradation by lithium carbonate oxidation products is less likely than an indirect route involving lattice oxygen. Further studies analyzing the effect of lithium carbonate oxidation in cathode materials that do not undergo bulk oxygen redox activity (for example, high-Ni NMC materials) are needed to fully understand the relationship between these processes.

Previous studies from our group have already demonstrated that the removal of surface lithium carbonate from NMC cathode materials via washing has a beneficial effect on outgassing [37] and cyclability [31]. This work underscores the importance of developing such procedures in order to realize the implementation of state-of-the-art high-energy cathode materials in commercial systems.

2.6 Supporting Information

2.6.1 Hydrogen evolution during control experiments

In order to further clarify that CO_2 evolution from lithium carbonate is the result of direct electrochemical oxidation rather than a chemical reaction with electrolyte decomposition products (such as protons), H_2 evolution at m/z = 2 is shown during charge at 10 mV/min along with $^{12}CO_2$ evolution at m/z = 44 (also plotted in Figure 2.3) for a carbon cathode (Figure 2.10a) as well as a carbon cathode isolated from a $Li_2^{13}CO_3$-impregnated glass fiber separator by additional polypropylene separators (Figure 2.10b). In both cases, H_2 evolves along with $^{12}CO_2$ starting around 4.8 V vs. Li/Li^+, indicating the onset of electrolyte degradation. H_2 is presumably formed at the anode via a reaction with protons, which are likely produced via ethylene carbonate dehydrogenation. However, H_2 does not evolve until a much higher voltage than the onset of $^{13}CO_2$ from lithium carbonate when electrically connected as shown in Figure 2.2b. These results strongly suggest that electrolyte degradation processes do not cause lithium carbonate degradation, in support of the conclusion that lithium carbonate is decomposed by direct electrochemical oxidation.

2.6.2 Effect of air exposure via Warder titration

NMC powder samples were exposed to ambient air for controlled amounts of time and then immersed in nitrogen-sparged water in an argon atmosphere and titrated with hydrochloric acid in a two-step Warder titration. [47] In the first titration, phenolphthalein is used to detect the endpoint of around 8.2, at which lithium hydroxide is completely neutralized to form water and lithium carbonate is partially neutralized to lithium bicarbonate:

$$LiOH + H^+ \rightarrow Li^+ + H_2O \tag{2.4}$$

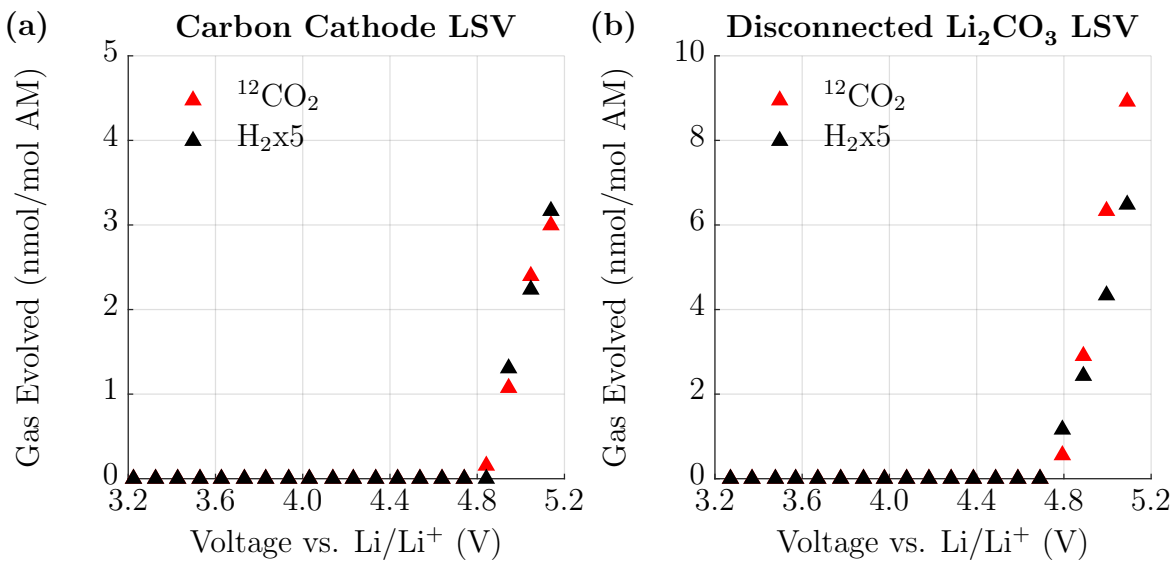

Figure 2.10: H_2 (black) and $^{12}CO_2$ (red) evolution during a 10 mV/min charge from a carbon cathode (a) and a carbon cathode with electrically disconnected $Li_2^{13}CO_3$ in the separator (b). Note that the $^{12}CO_2$ evolution shown here is also plotted in Figure 2.3.

$$Li_2CO_3 + H^+ \rightarrow Li^+ + LiHCO_3 \tag{2.5}$$

In the second titration, mixed indicator methyl red/bromocresol green is used to detect the endpoint of around 4.5, at which lithium bicarbonate is reacted to form carbonic acid:

$$LiHCO_3 + H^+ \rightarrow Li^+ + H_2CO_3 \tag{2.6}$$

Using this two-step titration procedure, the amounts of lithium carbonate and lithium hydroxide are separately calculated as shown for a Li-excess NMC provided by LG Chem that has been exposed to air for various amounts of time (Figure 2.11a). Over time, lithium carbonate builds up and lithium hydroxide is removed from the surface. Air exposure clearly has a negative impact on battery performance even in the first few cycles (Figure 2.11b), so an inert atmosphere should be maintained during material synthesis and handling.

2.6.3 Capacity from O_2^{2-} at high voltage

At high voltage, peroxo-like oxygen (O_2^{2-}) builds up on the cathode surface and can be measured by an acid titration after cathode extraction in an analogous fashion as lithium peroxide quantification via oxygen evolution:

$$Li_2O_2 + 2H^+ \rightarrow 2Li^+ + H_2O + \frac{1}{2}O_2 \tag{2.7}$$

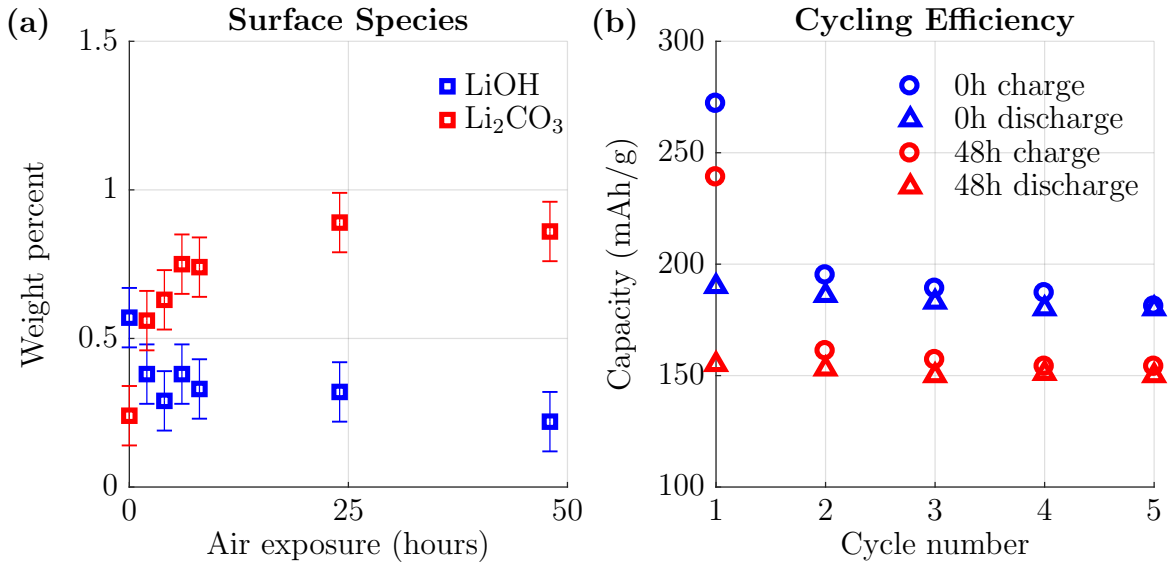

Figure 2.11: Chemical titration (a) and cycling efficiency at C/10 (b) of Li-excess NMC (LG Chem) with various air exposure times. Exposure times are provided in the figure legend.

Table 2.3: Capacity above 4.4 V from O_2^{2-} as measured using an acid titration and total measured capacity from 4.4V to the cutoff voltage indicated for pristine NMC.

Voltage	O_2^{2-} capacity	Total capacity over 4.4 V
4.4 V	0 mAh/g	0 mAh/g
4.6 V	101 mAh/g	91 mAh/g
4.8 V	163 mAh/g	168 mAh/g

The amount of peroxo-like oxygen can then be converted to a capacity based on the two-electron process in which lattice oxygen reacts to form peroxo-like oxygen:

$$2O^{2-} \rightarrow 2e^- + O_2^{2-} \tag{2.8}$$

Based on the charge curve (Figure 2.4) and peroxo-like oxygen titrated (Figure 2.5), the capacity attributed to oxygen redox can be compared to the total capacity at voltages above 4.4 V vs. Li/Li^+ (when peroxo-like oxygen is initially detected). For both the pristine (Table 2.3) and two-hour CO_2-exposed (Table 2.4) samples, all of the capacity above 4.4 V vs. Li/Li^+ can be attributed to oxygen redox. The error in titration measurements for peroxo-like oxygen is around 22 mAh/g based on repeat measurements.

Table 2.4: Capacity above 4.4 V from O_2^{2-} as measured using an acid titration and total measured capacity from 4.4V to the cutoff voltage indicated for two-hour CO_2-exposed NMC.

Voltage	O_2^{2-} capacity	Total capacity over 4.4 V
4.4 V	1 mAh/g	0 mAh/g
4.6 V	119 mAh/g	114 mAh/g
4.8 V	179 mAh/g	164 mAh/g

2.6.4 Titrations of isotopically labeled surface carbonates

Acid titrations of cathodes extracted from cells charged at 0.1C to various cutoff voltages show that $Li_2^{13}CO_3$ (added via two-hour $^{13}CO_2$ exposure of the NMC powder) is removed from the cathode surface during charge (Figure 2.12). This data confirms that the added surface carbonates are oxidized during charge to form CO_2 gas as shown in Figure 2.4d and do not contribute to the carbonates deposited on the surface as shown in Figure 2.5a.

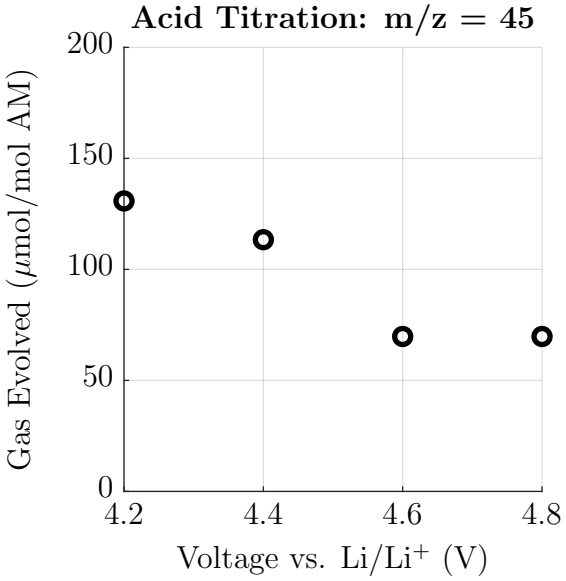

Figure 2.12: Isotopically labeled lithium carbonate (in this case, $Li_2^{13}CO_3$) is removed from the cathode surface during charge. In this sample, 250 μmol $Li_2^{13}CO_3$ was deposited on the surface via $^{13}CO_2$ exposure of the cathode powder before battery assembly.

3 Surface coatings partially mitigate interfacial instability of Li_2MnO_3

3.1 Abstract

As the cost of cathode materials like nickel and cobalt continues to increase, the research community has shown renewed interest in layered lithium manganese oxide (Li_2MnO_3) as a cheaper and more abundant cathode material. While Li_2MnO_3 has been studied to better understand lithium-rich cathode materials, which contain Li_2MnO_3 to increase the ratio of lithium to transition metal, it presents significant stability issues and very low reversible capacity on its own. This work investigates ball-milling as a surface stabilization technique to address the high reactivity of the LMO surface with the electrolyte. While ball-milling by itself did not significantly decrease the outgassing of LMO, addition of a graphitic fluoride coating during the ball-milling process suppressed O_2 evolution. This work highlights the importance of well-designed surface coatings to reduce side reactions and promote manganese redox in order to achieve a stable LMO cathode material.

3.2 Introduction

Layered lithium manganese oxide (Li_2MnO_3, abbreviated LMO) is of great interest, both as one of the phases present in lithium-rich transition metal oxide cathode materials along with $LiTMO_2$ and as a cathode material in its own right which evades the cost and availability concerns of other transition metals like nickel and cobalt. Recent work studying LMO as a cathode material [5, 48, 49] has shown that lithium de-insertion from this material is largely irreversible, with significant gas evolution and capacity loss occurring during cycling. However, the ability of LMO to access reversible manganese redox is still of great interest and has been observed to some extent by Zhuo et al. [50].

In order to create a stable LMO cathode, surface protection is necessary to suppress surface reactivity and potentially allow reversible bulk redox at high voltages. To that end, this work explores ball-milling as a method to incorporate surface protection through additive inclusion of graphitic fluoride or ZrO_2 during the ball milling process. While ball milling by itself did not substantially affect the stability of the cathode as measured by gas evolution, the graphitic fluoride coating suppressed O_2 evolution but increased CO_2 evolution. These results show that surface coatings can significantly alter the behavior of LMO, leaving open the possibility for a well-designed surface coating to reduce side reactions and promote reversible manganese redox. *

*This chapter includes with permission data and ideas that are also utilized in the following publications: Papp, J. K. et al. *Electrochim. Acta* **368** (2021) and Rana. J. et al. *ACS Energy Lett.* **5**, 634-641 (2020).

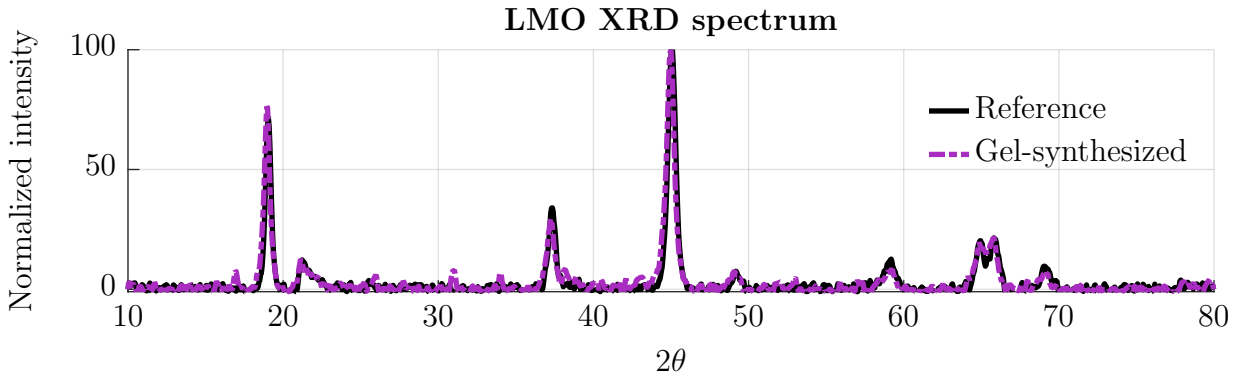

Figure 3.1: XRD spectrum showing the gel-synthesized LMO (purple dotted line) in comparison to a reference spectrum (black) reproduced with permission from [5].

3.3 Experimental methods

3.3.1 Synthesis procedure

Li_2MnO_3 (LMO) was prepared by combining solutions of manganese acetate, citric acid, and lithium hydroxide in water. The water was boiled off to form a gel, which was then freeze dried to produce a dry powder. The powder was subjected to a two-step calcination process, heating first at 450 °C for 10 h followed by 700 °C for 20 h under dry air (nitrogen and oxygen only). XRD results (Figure 3.1) show that layered LMO was successfully synthesized.

A separate batch of LMO prepared by collaborators [†] via a solid-state route was used for the ball-milled LMO measurements. This LMO was synthesized by mixing Li_2CO_3 and MnO_2 (Sigma-Aldrich) followed by calcination at 800 °C for 10 hours under an air atmosphere. For the ball milling process, 1.0 g pristine Li_2MnO_3 was added into the milling jar with ZrO_2 as the milling media, with a 1:15 material to ball mass ratio. In the case of the BM-C-F material, 100 mg graphitic fluoride [$(CF_x)_n$, x 1.1, Sigma-Aldrich] was used as an additive in the ball milling procedure.

3.3.2 Cell construction

Swagelok-type cells [12] were assembled for outgassing measurements. For the gel-synthesized LMO, cathodes were composed of active material, acetylene black, and PTFE at a weight ratio of 75:15:10. The electrolyte used was 1 M $LiPF_6$ in a 1:1 mixture by weight of ethylene carbonate and diethyl carbonate (Gotion). For the solid-state LMO, active material, carbon black (Super P C65) and polyvinylidene fluoride (PVdF) were mixed in a 70:20:10 weight ratio with a few drops of N-methyl-2-pyrrolidone (NMP) added to produce a thick, homogeneous slurry. The electrolyte used was 1 M $LiPF_6$ in 3:7 ethylene carbonate (EC): ethyl methyl carbonate (EMC) (LP57 from Gotion). For both types of LMO, cathodes were

[†]The author acknowledges Jianan Xu of Rice University for synthesizing these materials.

coated onto stainless steel mesh and assembled into lithium half-cells with two separators, one polypropylene (Celgard 2500) and one glass fiber (Whatman), with the Celgard in direct contact with the cathode. Lithium metal (FMC) was used as the anode.

3.3.3 Offgassing analysis

Off-gassing measurements were conducted using a custom-built differential electrochemical mass spectrometer as described by McCloskey et al. [12]. To achieve quantifiable results, calibrations were performed for each gas of interest (O_2 and CO_2) to relate the ion current detected by the mass spectrometer to the partial pressure of the gas of interest in argon. A similar setup as that used for DEMS measurements was used to monitor the gases evolved during an acid titration of cathodes extracted from cycled batteries. During this titration, in which an extracted cathode (washed 3x with DMC and vacuum dried) is placed in a vessel attached to the DEMS gas handling unit followed by injection of 10 M H_2SO_4, carbonates on the cathode surface react with acid to produce CO_2 gas:

$$Li_2CO_3 + 2H^+ \rightarrow 2Li^+ + H_2O + CO_2 \tag{3.1}$$

In addition, peroxo-like species (O_2^{2-}) on the cathode react to form O_2 gas in a similar fashion to the reaction between lithium peroxide and acid:

$$Li_2O_2 + 2H^+ \rightarrow 2Li^+ + H_2O + \frac{1}{2}O_2 \tag{3.2}$$

Control experiments confirm that these surface species react to form stoichiometric amounts of gas as detected by the mass spectrometer. [29]

3.3.4 Warder titrations

In order to measure carbonate content more quickly than the above mass spectrometer method, a chemical titration was also employed. In this titration, DMC-rinsed and dried cathodes are sealed inside a septum-cap vial filled with argon. Nitrogen-sparged water is added to the sample. Five minutes are allowed for surface species present on the sample to dissolve in the water. Then phenolphthalein indicator is added, turning the solution bright pink due to the dissolved basic salts (pH 11). The solution is titrated with dilute hydrochloric acid until it turns clear (pH = 8.2). Then mixed bromocresol green-methyl red indicator is added, turning the sample blue. The solution is titrated again until it turns pink (pH = 4.5). The entire process is conducted under air-free conditions.

In the first titration, lithium hydroxide is completely neutralized, and lithium carbonate is partially neutralized to lithium bicarbonate in solution:

$$LiOH + H^+ \rightarrow Li^+ + H_2O \tag{3.3}$$

$$Li_2CO_3 + H^+ \rightarrow Li^+ + LiHCO_3 \tag{3.4}$$

In the second titration, lithium bicarbonate is neutralized:

$$LiHCO_3 + H^+ \rightarrow Li^+ + H_2CO_3 \tag{3.5}$$

Calibrations were performed on both Li_2CO_3 and LiOH to ensure quantifiable results.

3.3.5 Closed-cell pressure measurements

Pressure measurements were conducted using a similar setup to outgassing measurements, but instead of sweeping gas from the cell to a mass spectrometer, the cell was kept isolated and the headspace pressure monitored. The headspace volume was calibrated using capillary loops of known volume, thereby allowing molar evolution of total gas to be quantified from pressure rise and decay measurements.

3.4 Results and Discussion

3.4.1 First charge gas evolution

The first-charge gas evolution results for the gel-synthesized LMO, shown in Figure 3.2, are consistent with those reported in the literature [5, 48, 49]. Immediately upon the start of charge, CO_2 evolution begins, followed by O_2 evolution at higher voltage. O_2 evolution continues during the voltage hold portion of the CCCV (constant-current constant-voltage) charge, mirroring the decrease in current. The gas evolution results are presented as currents instead of moles of gas by assuming two-electron-per-CO_2 and four-electron-per-O_2 processes. While the exact mechanism of the gas-evolving processes is unknown, the evolved CO_2 must be a result of the oxidation of either surface Li_2CO_3 or the carbonate electrolyte via a two-electron process. Similarly, the evolved O_2 must be a result of oxidation of lattice oxide via a four-electron process.

By using the stoichiometry of these generalized equations, gas evolution can be converted to current to more clearly show the contribution of each gas-evolving process to the overall current. As shown in Figure 3.2, gas-evolving processes contribute significantly to the total current passed during the first charge (as tabulated in Table 3.1, left column), but they do not account for all of the current, indicating that other processes are also occurring which contribute to the overall current (for example, carbonate deposition onto the cathode surface as a result of electrolyte degradation). Nevertheless, O_2 and CO_2 evolution are irreversible

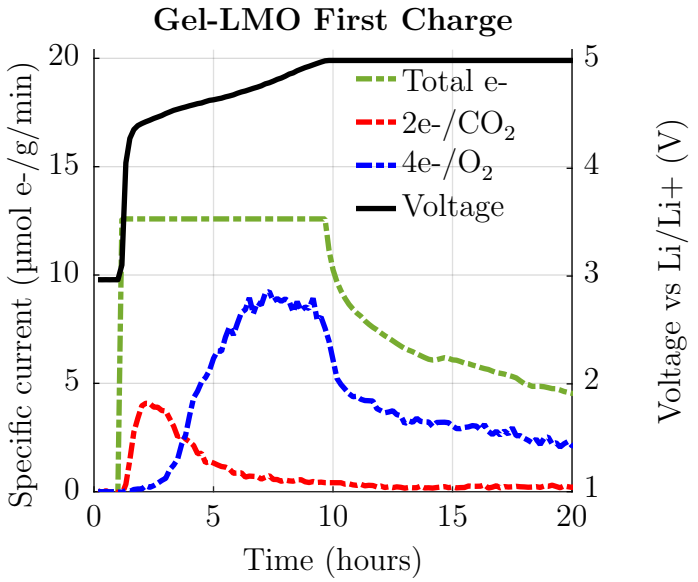

Figure 3.2: Gas evolution results for the first CCCV charge at 20 mA/g with a voltage hold at 5 V vs. Li/Li^+ of the gel-synthesized LMO showing CO_2 and O_2 evolution converted to currents assuming 2 electron-per-CO_2 (red) and 4-electron-per-O_2 (blue) processes, respectively, for comparison to the total current (green).

processes that cause capacity fade of the battery, motivating the use of surface coatings to improve LMO interfacial stability.

To investigate the effect of surface coatings on LMO interfacial stability, LMO powder was ball-milled with and without graphitic fluoride (C-F) before mixing into a slurry and coating onto a current collector as described in the Experimental methods section. The ball-milled LMO samples were charged using a similar technique, except that a longer OCV period (12 hours) was used along with a slower (10 mA/g) charge rate for the constant-current part of the charge. The sample with no C-F coating, BM-LMO (Figure 3.3a), shows similar O_2 evolution results as the gel-synthesized LMO, but markedly different CO_2 evolution. The absence of CO_2 at the beginning of charge is likely related to a ZrO_2 surface coating formed as a result of ball-milling using ZrO_2 balls. In contrast, the C-F coated sample, BM-C-F-LMO (Figure 3.3b) shows almost no O_2 evolution but greatly increased CO_2 evolution at high voltage. The increase in CO_2 evolution is unlikely to be related to electrolyte decomposition, as the surface is protected by the C-F coating, so it is likely due to oxidation of additional surface carbonates that were deposited as a result of decomposition of the C-F coating (the increased carbonate content is confirmed later using acid titrations). The contributions of each outgassing process to the overall capacity as shown in Figures 3.2 and 3.3 are tabulated for each of the three LMO samples in Table 3.1.

To better understand the effect of surface carbonates on the chemical reactivity and gas evolution results for each of these materials, carbonate titrations were performed be-

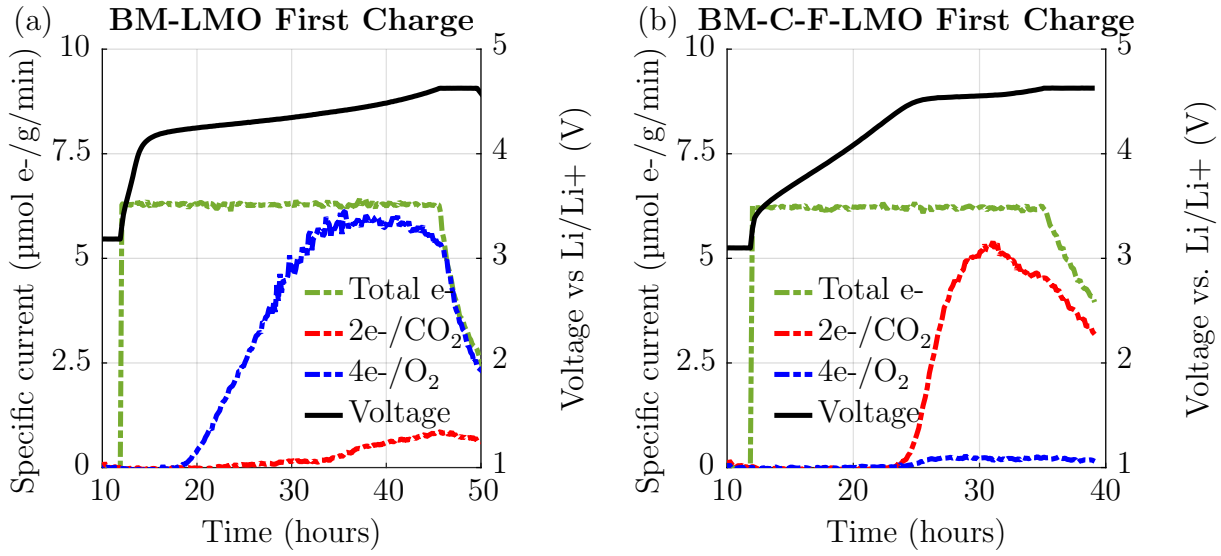

Figure 3.3: Gas evolution results for the first charge at 10 mA/g of the ball milled LMO (a) and the ball milled LMO with a C-F coating (b) showing CO_2 and O_2 evolution converted to currents assuming 2 electron-per-CO_2 and 4-electron-per-O_2 processes, respectively. A voltage hold was included at the upper cutoff voltage of 4.6 V vs. Li/Li^+.

Table 3.1: First charge capacity contributions from evolved gases

Material	Gel-LMO	BM-LMO	BM-C-F-LMO
O_2 gas capacity	101.1 mAh/g (45%)	215.3 mAh/g (60%)	5.5 mAh/g (2%)
CO_2 gas capacity	23.2 mAh/g (10%)	19.8 mAh/g (5%)	104.3 mAh/g (40%)
Total capacity *	225.8 mAh/g	364.5 mAh/g	263.8 mAh/g

* Using an upper cutoff voltage of 5.0 V vs. Li/Li^+ at 20 mA/g (Gel-LMO) or 4.6 V vs. Li/Li^+ at 10 mA/g (BM- and BM-C-F-LMO) with a 4-hour voltage hold. Percentages in parentheses show how much capacity is attributable to each gas.

fore and after each material was exposed to electrolyte for 12 hours (Table 3.2). For the gel-synthesized LMO, a moderate increase in carbonate content is observed after soaking in electrolyte, showing that the LMO surface is chemically unstable to the electrolyte. The increase in carbonates after electrolyte exposure is more pronounced for the BM-LMO and BM-C-F-LMO, the latter of which shows an extremely high carbonate content even before electrolyte exposure, likely due to carbonate formation during the C-F coating procedure. Interestingly, the BM-LMO and BM-C-F-LMO also show less hydroxide content after electrolyte exposure (hydroxide was not measured for the gel-LMO), implying that hydroxide is a reactant in a reaction that produces surface carbonates during electrolyte exposure. While the ball-milling process does not protect the LMO surface from reacting chemically with the electrolyte to produce new surface carbonates, it does delay CO_2 evolution as shown in Fig-

Table 3.2: Effect of 12-hour electrolyte exposure on LMO surface species

Material	Gel-LMO	BM-LMO		BM-C-F-LMO	
Surface species	Carbonate *	Carbonate **	Hydroxide **	Carbonate **	Hydroxide **
Before exposure	0.9 wt%	1.0 wt%	10 wt%	14 wt%	15 wt%
After exposure	1.5 wt%	3.1 wt%	8.2 wt%	16 wt%	3.7 wt%

* Measured by mass spectrometer acid titration
** Measured by Warder titration

ure 3.3. Since CO_2 evolution does occur later during charge for these materials, the surface carbonate present before the start of charge likely plays a role in protecting the surface from CO_2 evolution at low voltage but is oxidized away to produce CO_2 at high voltage.

3.4.2 First discharge and second charge

While the first charge of LMO is largely characterized by gas-evolving degradation processes, the dramatic surface transformations caused by evolution of O_2 and CO_2 and deposition of new carbonates during the first charge likely result in different degradation processes in subsequent cycles. In order to probe discharge processes that may occur as a result of consumption of the gas evolved during the first charge, a closed setup was used such that the pressure could be monitored as a proxy for gas consumption.

Figure 3.4 shows gas evolution and consumption results for the first cycle in a closed system for the ball-milled LMO samples. The closed system was comprised of an isolated cell headspace of roughly 2 mL and an in-line pressure transducer to monitor headspace pressure as a function of time. For both ball-milled materials, the pressure increases during charge due to gas evolution and then decreases during discharge due to gas consumption. Table 3.3 tabulates the amount of gas evolved and consumed on charge and discharge, respectively, for each material. The gas evolution results agree well with the DEMS results for the first charge, with 2577 and 1542 µmol/g evolved for BM-LMO and BM-C-F-LMO, respectively, compared to the 2379 and 1997 µmol/g observed from the DEMS experiments shown in Figure 3.3.

While gas is consumed on discharge for both materials, consistent with previous work [5], DEMS results showed that the majority of gas evolved in the case of BM-LMO is O_2, while for BM-C-F-LMO it is CO_2. Along with the hump in the discharge curve for BM-LMO characteristic of oxygen gas reduction to peroxide, these results imply that O_2 is reduced to peroxide during discharge of BM-LMO, while CO_2 is reduced to carbonate during discharge of BM-C-F-LMO. Note that peroxide is highly reactive with the carbonate electrolyte and is likely to immediately chemically react to form additional carbonates [12].

In addition to the closed system pressure measurements, carbonate titrations of BM-LMO and BM-C-F-LMO cathodes at the top of charge (4.6 V vs. Li/Li^+) as well as at

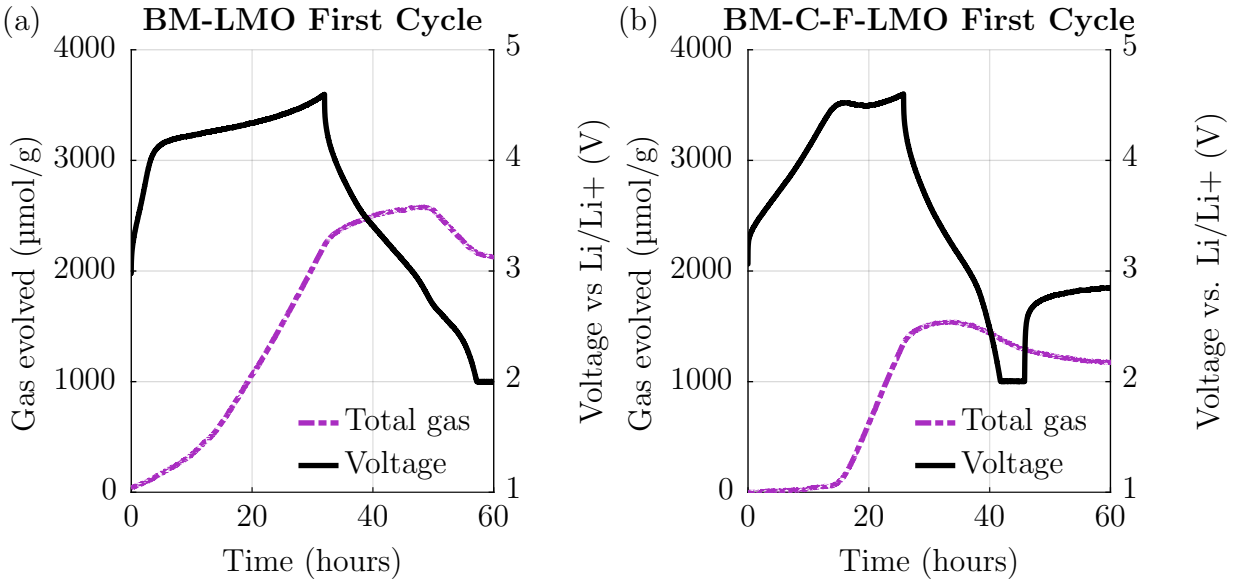

Figure 3.4: Closed system pressure measurement for the first cycle at 10 mA/g of the ball milled LMO (a) and the ball milled LMO with a C-F coating (b) showing total gas evolution and consumption.

Table 3.3: Gas evolution and consumption during the first cycle in a closed system

Material	BM-LMO	BM-C-F-LMO
Gas evolved *	2577 umol/g	1542 umol/g
Gas consumed **	463 umol/g	369 umol/g

* Calculated from the difference between the initial and highest pressures measured

** Calculated from the difference between the highest and final pressures measured

the bottom of discharge (2.0 V vs. Li/Li^+) show that large amounts of carbonates are deposited during discharge (Table 3.4). Note that there is a decrease in carbonate content during charge, as demonstrated by the difference between the electrolyte-soaked cathodes shown in Table 3.2 and the charged cathodes shown in Table 3.4, due to the oxidation of surface carbonates during charge. Together, these data show cyclic behavior of carbonate oxidation and deposition during cycling, which contributes a modest amount of capacity on both charge and discharge. Note that the mass spectrometer acid titration is also capable of measuring peroxo-like oxidized oxygen, but these species were not detected in agreement with previous work [5, 50].

The second-charge gas evolution results for BM-LMO and BM-C-F-LMO (Figure 3.5) show significantly reduced gas evolution as well as a much lower capacity than the ini-

Table 3.4: Carbonate content at end of first charge and discharge

Material	BM-LMO	BM-C-F-LMO
Charged to 4.6V *	2.7 wt%	5.6 wt%
Discharged to 2.0V *	13 wt%	12 wt%

* Measured by mass spectrometer acid titration

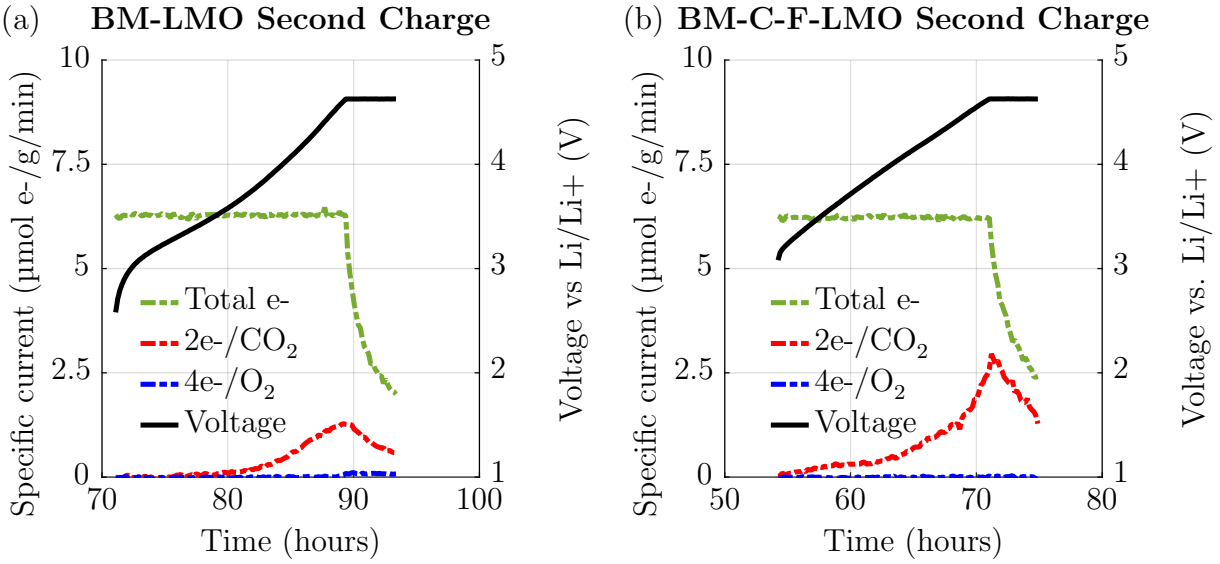

Figure 3.5: Gas evolution results for the second charge at 10 mA/g of the ball milled LMO (a) and the ball milled LMO with a C-F coating (b) showing CO_2 and O_2 evolution converted to currents assuming 2 electron-per-CO_2 and 4-electron-per-O_2 processes, respectively. A voltage hold was included at the upper cutoff voltage of 4.6 V vs. Li/Li^+.

tial charge. While no O_2 evolution was detected for either material on the second charge, continued CO_2 evolution supports the previous evidence of cyclic carbonate oxidation and deposition during cycling. In the second charge, as with the first discharge, processes involving gas evolution or consumption only account for a small fraction of the total capacity (Table 3.5), leaving open the possibility of reversible manganese redox after the first charge. However, the continued evolution of CO_2 as well as the significant loss in capacity during cycling indicate that additional processes relating to electrolyte degradation at the cathode surface are also at play. To parse out the processes responsible for the remaining capacity, additional techniques are needed to measure the manganese oxidation state during cycling.

3.5 Conclusion

This work highlights the surface reactivity of LMO with carbonate electrolytes, whether produced via gel synthesis or solid state ball-milling. Interestingly, the O_2 evolution behavior

Table 3.5: Second charge capacity contributions from evolved gases

Material	BM-LMO	BM-C-F-LMO
O_2 gas capacity	0 mAh/g (0%)	0 mAh/g (0%)
CO_2 gas capacity	17.5 mAh/g (10%)	36.3 mAh/g (20%)
Total charge capacity *	205.0 mAh/g	190.3 mAh/g

* Using a constant-current charge to an upper cutoff voltage of 4.6 V vs. Li/Li^+ at 10 mA/g followed by a 4-hour voltage hold

is quite distinct from that of lithium-rich cathode materials even though LMO is one of the two phases present in that type of cathode, leaving open questions about what conditions are necessary to facilitate the unique oxygen redox behavior of lithium-rich cathode materials.

As a cathode material by itself, LMO is quite unstable. While the O_2 evolution of LMO was suppressed by ball-milling with a graphitic fluoride coating, the continued CO_2 evolution as a result of carbonate oxidation and deposition is still a major concern. However, the ability of LMO to undergo reversible manganese redox remains an intriguing possibility and is worth pursuing using other methods to stabilize the cathode surface.

3.6 Supporting Information

Cathode materials BM-LMO and BM-C-F-LMO were also coated onto aluminum foil instead of stainless steel mesh to replicate the typical coin cell setup. Interestingly, gas evolution results for these cathodes (Figure 3.6) were quite different from those shown in Figure 3.3 using stainless steel mesh. For BM-LMO (Figure 3.6a), the O_2 evolution was significantly reduced along with the total capacity (Table 3.6) and the CO_2 evolution was increased. The CO_2 evolution was also increased compared to the stainless steel mesh for BM-C-F-LMO (Figure 3.6b), along with the overall capacity (Table 3.6), in this case even surpassing the total current. Since the current attributable to CO_2 evolution cannot by definition be greater than the total current, the two-electron-per-CO_2 assumption must be wrong, implying that some of the CO_2-evolving processes are corrosive. These results show that not only the carbonate electrolyte but also the aluminum current collector participates in degradation reactions for these cathode materials. Compared to the stainless steel mesh, the aluminum current collector seems to promote CO_2 evolution and suppress O_2 evolution. These results present an additional future consideration for the study of these materials.

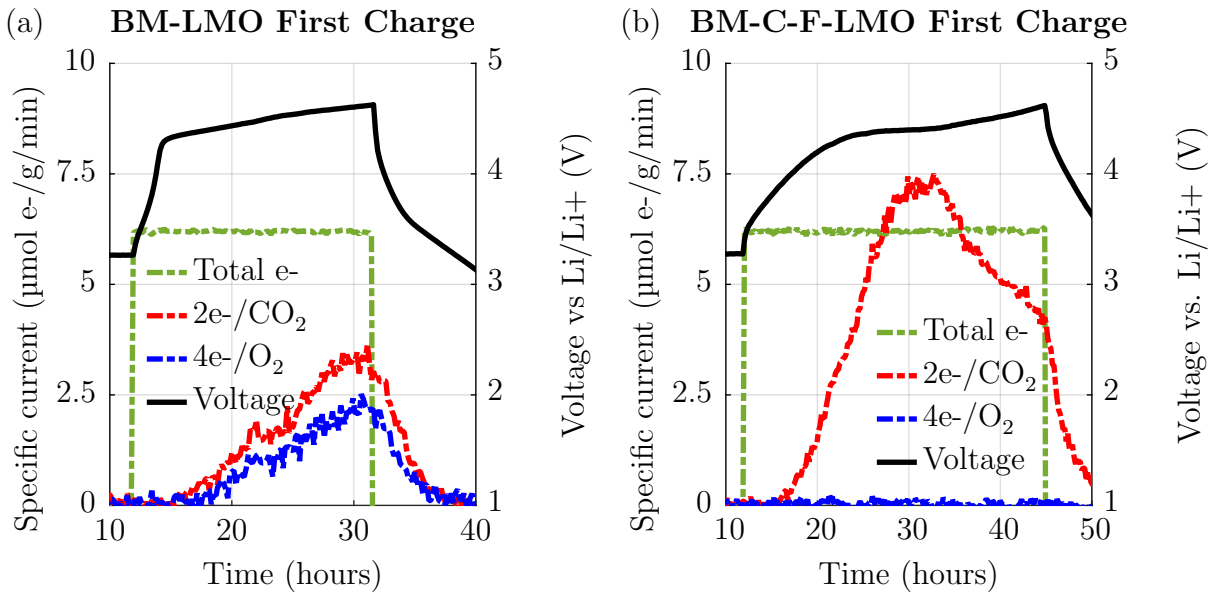

Figure 3.6: Gas evolution results for the first charge at 10 mA/g using an aluminum foil current collector of the ball milled LMO (a) and the ball milled LMO with a C-F coating (b) showing CO_2 and O_2 evolution converted to currents assuming 2 electron-per-CO_2 and 4-electron-per-O_2 processes, respectively.

Table 3.6: First charge capacity contributions from evolved gases (Al foil)

Material	BM-LMO	BM-C-F-LMO
O_2 gas capacity	30.2 mAh/g (15%)	1.6 mAh/g (0.5%)
CO_2 gas capacity	47.1 mAh/g (24%)	218.9 mAh/g (66%)
Total capacity *	196.9 mAh/g	329.8 mAh/g

* Using an upper cutoff voltage of 4.6 V vs. Li/Li^+ at 10 mA/g

4 Particle surface cracking is correlated with gas evolution in high-nickel lithium-ion cathode materials

4.1 Abstract

High-Ni layered oxide cathode materials ($LiNi_xTM_{(1-x)}O_2$ where x > 0.8) are of great interest because they offer increased capacity compared to current commercial materials within a narrow voltage range. However, recent studies have shown that these materials in their current form suffer from capacity fading when an upper cutoff voltage above 4.3 V vs. Li/Li^+ is used. While many studies have focused on the H2 → H3 transition as the primary cause of capacity fading, gas evolution studies show that degradation processes cannot be attributed to the H2 → H3 transition alone. In this work, differential electrochemical mass spectrometry (DEMS) is combined with titration mass spectrometry (TiMS) to measure gases evolved in a lithium half-cell during cycling as well as species which evolve gas upon addition of strong acid to an extracted cathode. Along with qualitative observations of particle cracking by scanning electron microscopy (SEM), these results reveal correlations between particle cracking, electrolyte reactivity, and carbonate oxidation and deposition onto the cathode during the first charge of high-Ni cathode materials.*

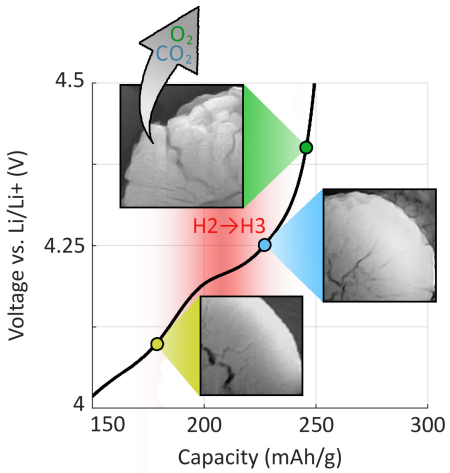

*This chapter adapted with permission from previously published work in: Kaufman, L. A., Huang, T. Y., Lee, D. H., and McCloskey, B. D. *ACS Appl. Mater. Interfaces*, in review.

4.2 Introduction

High-Ni cathode materials ($LiNi_xTM_{(1-x)}O_2$ where x > 0.8) for lithium-ion batteries are prime candidates for commercialization because of the high capacity they achieve within a relatively narrow voltage range (3.0 - 4.2 V vs. Li/Li^+). However, they still suffer from capacity fading when cycled to upper cutoff voltages over 4.3 V vs. Li/Li^+ [51], limiting their usable capacity until the degradation processes at these voltages can be identified and mitigated. Previous works have identified the cause of this capacity fading as the H2 → H3 transition, a phase transition that occurs around 4.2 V vs. Li/Li^+ during charge for materials with >80% nickel [15] and is accompanied by a severe volume contraction [14]. This volume contraction is thought to trigger micro-cracking within secondary particles [17] as well as formation of a densified NiO surface phase and oxygen gas evolution [16]. Various dopants and coating materials including aluminum [52], zirconium[53], and boron [54] have been proposed in order to mitigate these degradation processes.

In this work, we present gas evolution studies on high-Ni materials under development for commercial use by LG Energy Solution. These materials contain a boron-based surface coating designed to prevent low-voltage outgassing from surface carbonates [55, 56]. As a result, the data presented here represents the performance/outgassing expected of true optimized commercial cathode materials. Despite these measures, the materials studied still show gas evolution at high voltage which can be linked to particle cracking and electrolyte reactivity. In addition, we observe the oxidation and deposition of buried carbonates (carbonates located deep inside the secondary particle rather than near the particle surface) during charge and discharge, respectively, as a result of the opening and closing of micro-cracks. Surface processes, in cooperation with the bulk volume changes that characterize the H2 → H3 phase transition, are the primary cause of degradation in these materials.

4.3 Experimental methods

4.3.1 Cell construction

Swagelok-type cells [12, 57] were assembled with cathodes composed of 90 wt% active material, 5 wt% carbon black (Super P), and 5 wt% polyvinylene fluoride binder coated onto stainless steel mesh. The electrolyte used was 1 M $LiPF_6$ in a 1:1 mixture by weight of ethylene carbonate and diethyl carbonate (Gotion). Cells were assembled with two separators, one polypropylene (Celgard 2500) and one glass fiber (Whatman), with the Celgard in direct contact with the cathode. Lithium metal (FMC) was used as the anode.

4.3.2 Offgassing analysis

Differential electrochemical mass spectrometry (DEMS) is used to detect gases evolved from a battery during cycling [12]. The cell is designed with inlet and outlet capillaries connecting to the cell headspace. Every few minutes, the outlet is opened, allowing accumulated gases to flow to a mass spectrometer, and the cell headspace is subsequently refilled through the

inlet with a carrier gas such as argon. In order to achieve quantifiable results, calibrations are performed to relate the ion current detected by the mass spectrometer to the partial pressure of the gas of interest in argon.

Additionally, a similar setup can be used to monitor gases evolved during an acid titration of cathodes extracted from cycled batteries in a technique called titration mass spectrometry (TiMS) [30]. During these titrations, in which an extracted cathode is placed in a vessel attached to the DEMS gas handling unit, followed by injection of 10 M H_2SO_4, carbonates present on the cathode react with acid to produce CO_2 gas and peroxo-like species (O_2^{2-}) on the cathode react to form O_2 gas in a similar fashion to the reaction between lithium peroxide and acid as discussed in prior chapters.

4.3.3 Inductively coupled plasma optical emission spectroscopy

Inductively coupled plasma optical emission spectroscopy (ICP) measurements were performed using a Perkin Elmer 5300 DV optical emission ICP spectrometer with an auto sampler. To prepare for ICP measurements, post-titration H_2SO_4 solutions were diluted 250 times in 2% nitric acid. Three standard solutions were used to calibrate nickel, cobalt, and manganese between 1 and 100 mg/L (nickel) or 0.1 and 10 mg/L (cobalt and manganese). All sample measurements fell within the calibrated range.

4.3.4 Scanning electron microscopy

Surface scanning electron microscopy (SEM) measurements were performed using a JEOL scanning electron microscope. Samples were stored under argon and exposed to ambient air for less than one minute during sample preparation and transfer to the SEM.

Cross-sectional SEM measurements were performed using a Quanta 3D FEG focused-ion-beam / scanning-electron microscope (FIB/SEM). In order to obtain clean cross-sections, samples were first cut at 3 nA and then polished at 0.5 nA with a Ga^+ ion beam.

4.4 Results and discussion

4.4.1 First charge gas evolution

In this study we present data on three cathode materials with approximate chemical formulas $LiNi_{0.65}Mn_{0.17}Co_{0.18}O_2$ (Ni 65%), $LiNi_{0.85}Mn_{0.07}Co_{0.05}Al_{0.03}O_2$ (Ni 85%), and $LiNi_{0.92}Mn_{0.02}Co_{0.04}Al_{0.02}O_2$ (Ni 92%). All three materials have a boron-based surface coating designed to suppress low voltage gas evolution from surface carbonates. Of these three materials, Ni 65% does not show the 4.2V voltage plateau on charge characteristic of the H2 $\rightarrow$ H3 transition (Figure 4.1a), while both Ni 85% and Ni 92% do (Figure 4.1b). Based on the nickel content and existence of the H2 $\rightarrow$ H3 phase transition, Ni 65% is not considered a high-Ni material for the purpose of this study but is included as a useful comparison to the two high-Ni materials Ni 85% and Ni 92%.

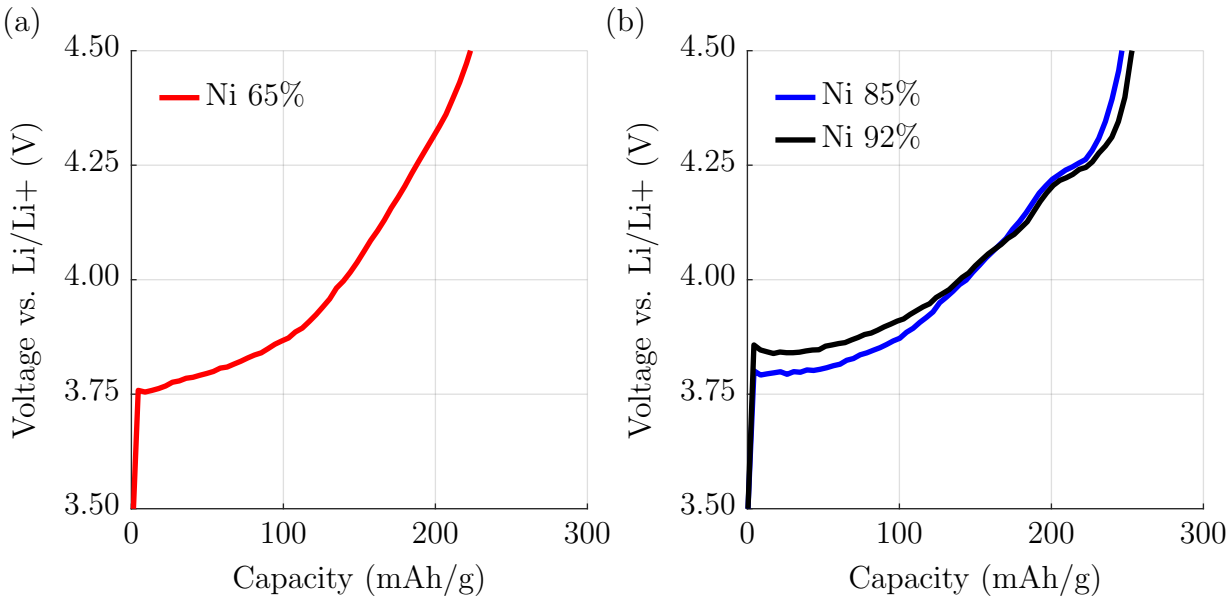

Figure 4.1: First charge at 0.1C to 4.5 V vs. Li/Li^+ for control cathode material Ni 65% (a) and high-Ni cathode materials Ni 85% and Ni 92 % (b) in lithium half-cells. For the high-Ni cathodes, the H2 $\rightarrow$ H3 transition occurs at the plateau around 200 mAh/g and 4.2 V vs. Li/Li^+.

For each material, DEMS experiments were conducted using a constant current-constant voltage (CCCV) protocol consisting of a 0.1C charge to a specified upper cutoff voltage followed by a 4-hour hold at that voltage. A variety of upper cutoff voltages were tested including values before and after the H2 $\rightarrow$ H3 transition. The voltage hold was included in order to remove any kinetic limitations and allow gas-evolving processes that occur at the upper cutoff voltage to go to completion. See the Experimental methods section for a detailed explanation of the experimental setup and data analysis involved in DEMS experiments.

For the control material Ni 65%, no gas was evolved on the first charge aside from a small amount of O_2 gas at low (3.8 - 4.1 V vs. Li/Li^+) voltages from the boron-based surface coating (Figure 4.8). Similar low voltage O_2 evolution is observed from both high-Ni materials (Figure 4.2c-d). Note that no low-voltage CO_2 evolution was observed for these materials, in contrast to our prior reports on Ni 60% [29, 30, 37], due to the suppression of outgassing from surface carbonate oxidation by the boron-based surface coating. Both high-Ni materials also showed coincident evolution of O_2 and CO_2 gases after the H2 $\rightarrow$ H3 transition (Figure 4.2). The onset voltage of gas evolution was slightly different between the two materials: for Ni 85%, gas evolution started at 4.35 V vs. Li/Li^+, while for Ni 92%, gas evolution started at a slightly lower voltage of 4.30 V vs. Li/Li^+. The difference in onset voltage for gas evolution can be seen more clearly with a linear voltage sweep (Figure 4.9). Interestingly, even though the H2 $\rightarrow$ H3 phase transition is completed around 4.25 V vs. Li/Li^+, additional delithiation is necessary to trigger gas evolution for both high-Ni

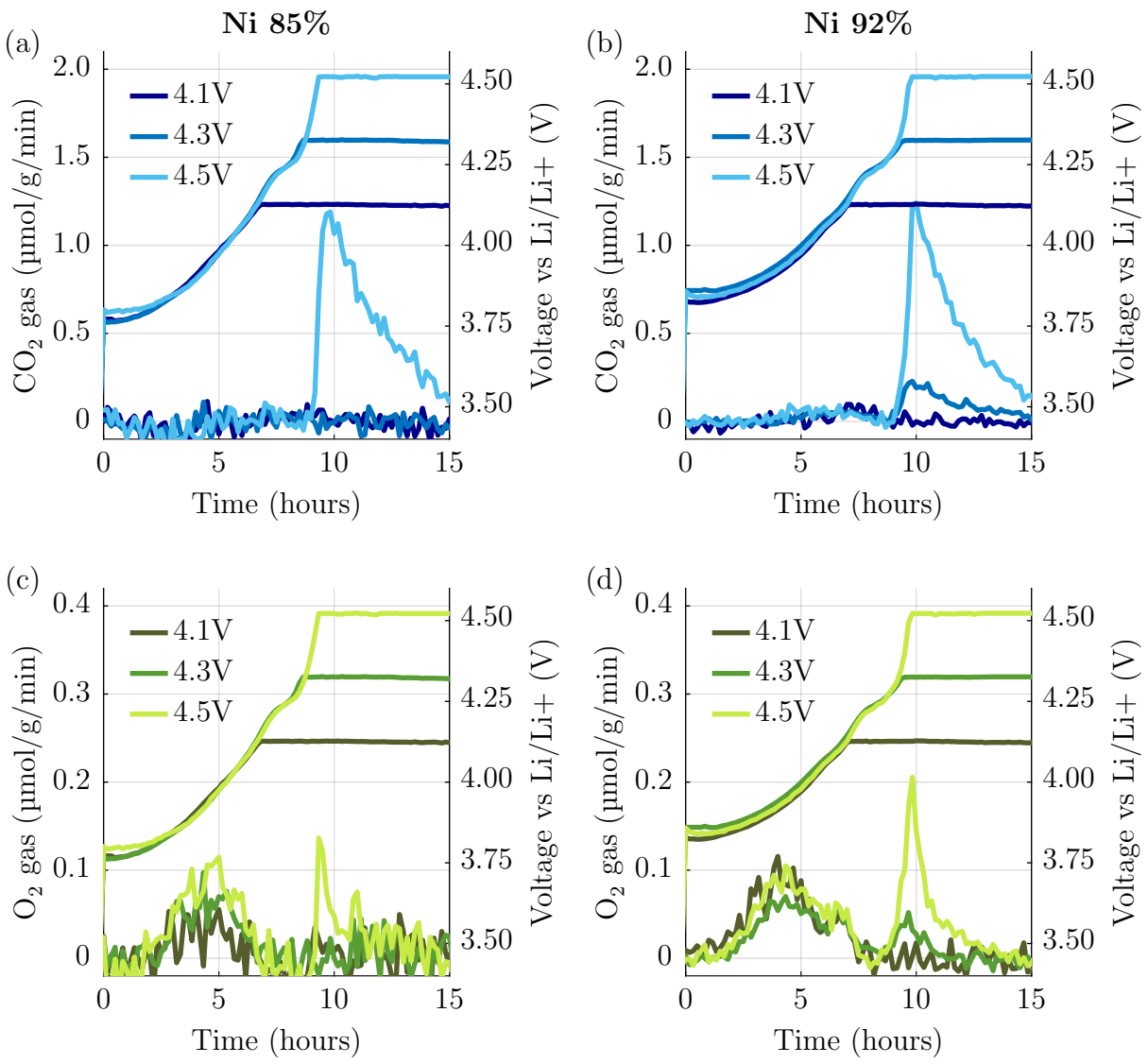

Figure 4.2: DEMS results for the first charge at 0.1C for high-Ni cathode materials Ni 85% (a,c) and Ni 92% (b,d) showing CO_2 (a,b) and O_2 (c,d) gas evolution. Aside from the low-voltage O_2 peak attributed to the surface coating, the two gases evolve together at a voltage slightly above the completion of the H2 → H3 transition for both materials.

materials. This implies that while the phase transition may destabilize the cathode structure, the degradation processes that occur during subsequent delithiation are the direct cause of outgassing.

Either residual carbonate oxidation or electrolyte decomposition could produce CO_2 gas during charge. Previous studies have clarified the source of CO_2 gas using an isotopic tag

Table 4.1: Evolved CO_2(g) isotope distribution after $Li_2C^{18}O_3$ deposition

Material	Ni 85%		Ni 92%	
Experiment	TiMS	DEMS	TiMS	DEMS
$C^{16,16}O_2$ (µmol/g)	13.7 (63%)	16.8 (75%)	38.7 (90%)	25.8 (91%)
$C^{16,18}O_2$ (µmol/g)	4.6 (21%)	3.7 (17%)	2.7 (6.3%)	1.9 (6.9%)
$C^{18,18}O_2$ (µmol/g)	3.6 (16%)	1.9 (8.3%)	1.5 (3.5%)	0.5 (1.9%)
% ^{18}O *	27%	17%	6.6 %	5.3%

* Calculated by dividing the number of ^{18}O-labeled oxygen atoms by the total number of oxygen atoms in the evolved CO_2.

[29, 30, 37]; however, in this case, the high temperature required for isotopic exchange decomposes the surface coating, resulting in a large increase in CO_2 evolution as well as the disappearance of the low-voltage O_2 peak (Figure 4.10). Instead, the material was exposed to isotopically tagged $C^{18,18}O_2$ gas at room temperature, resulting in deposition of a very small amount of isotopically tagged carbonates ($Li_2C^{16,18,18}O_3$) as measured by TiMS and DEMS (Table 4.1). We note that due to the effectiveness of the boron surface coating in suppressing CO_2 reactivity, it was very difficult to deposit carbonates on these materials as compared to uncoated cathode materials [57], and the tiny amount that was successfully deposited is likely located just under the surface coating as a result of small imperfections in the coating or CO_2 diffusion through it. Table 4.1 presents the overall ^{18}O isotopic enrichment of carbonates, as measured by CO_2 evolution after acid exposure, on an uncharged cathode after this procedure (TiMS columns), as well as the distribution of the various CO_2 isotopes evolved during the first charge of the $C^{18,18}O_2$-exposed high-Ni samples to 4.5 V vs. Li/Li^+ (DEMS columns). There is a smaller percentage of ^{18}O-tagged oxygen in the CO_2 gas evolved during charge than would be expected from carbonates alone (Table 4.1, final row), so CO_2 must be evolved due to a combination of carbonate oxidation and electrolyte decomposition. Dividing the percentage of ^{18}O-tagged oxygen atoms observed via TiMS by that observed via DEMS, we conclude that 62 ± 8% of the CO_2 evolved is attributed to carbonate oxidation for Ni 85%, while 81 ± 15% is attributed to carbonate oxidation for Ni 92%.

The coincident onset of O_2 and CO_2 outgassing for both high-Ni materials (Figure 4.2) implies that the processes causing each gas to evolve are coupled in some way. Since the H2 → H3 phase transition is thought to be triggered by charge transfer from oxygen to nickel, [16] it may result in destabilized lattice oxygen, increasing the likelihood that oxygen will evolve as gas, but since additional current is passed after the phase transition before gas is evolved, the observed O_2 and CO_2 evolution cannot be explained by this effect alone. In the next section, we show that internal cracks reach the particle surface concurrently with high voltage O_2 and CO_2 outgassing, suggesting that the two are intrinsically linked.

4.4.2 Particle cracking

In order to observe the extent of micro-cracking and its relationship with gas evolution, cathodes were extracted from DEMS cells at various upper cutoff voltages and examined using surface and cross-sectional SEM. For each experiment, at least three particles were examined, with the images shown here representative of all of the particles imaged.

Surface SEM images show a very strong correlation between the appearance of micro-cracks and the evolution of gas for all materials studied. For the Ni 65% control, no cracks were observed at any voltage (Figure 4.11). Surface cracks were absent from the high-Ni materials before the onset of gas evolution, even after the completion of the H2 → H3 transition (Figure 4.12), but became evident at voltages at which gas evolved (Figure 4.3a-b). Interestingly, the micro-cracks were observed both between and through primary particles (Figure 4.3c-d) as seen in previous work [58]. This correlation provides strong evidence that surface cracking, rather than the H2 → H3 transition, directly causes gas evolution.

High-Ni samples charged to 4.1 V, 4.25 V, and 4.4 V vs. Li/Li^+ as well as a pristine sample were chosen for cross-sectioning to investigate internal cracking. There are no cracks in the pristine material (Figure 4.4a), but a few small voids are visible which may be nucleation points for the cracks that form during charge [59]. In agreement with previous studies, [15, 17] images of charged samples show a complex network of micro-cracks inside the particle. Notably, at 4.1 V and 4.25 V vs. Li/Li^+ (Figure 4.4b-c), the cracks do not reach the particle surface, in agreement with surface SEM images. At 4.4 V vs. Li/Li^+ (Figure 4.4d), the micro-cracks extend throughout the entire particle to the surface. Only once the cracks are exposed to the electrolyte do the gas-evolving processes (aside from the low-voltage O_2 evolution from the surface coating) begin, showing that gas evolution is caused by either (i) the release of gases that were trapped inside the particle or (ii) the production of gases via reaction between the newly exposed cathode particle surface and the electrolyte.

Despite the presence of internal micro-cracks and the completion of the H2 → H3 transition, these surface-modified high-Ni materials maintain stability against gas evolution on the first charge at 4.25 V vs. Li/Li^+. Gas is only evolved after further charge and propagation of micro-cracks to the particle surface as shown at 4.4 V vs. Li/Li^+. These results provide evidence that further delithiation after the completion of the H2 → H3 phase transition is necessary to cause internal micro-cracks to reach the particle surface and gas to evolve.

4.4.3 Acid titrations

In order to better understand the condition of the cathode before and after gas evolution, titration mass spectrometry (TiMS) was used to analyze cathodes extracted from DEMS cells at the upper cutoff voltage. This technique provides information about the amount of carbonates and peroxo-like oxidized oxygen present in the particle. See the Experimental methods section for equations describing the reaction that produces gas from each of these types of species.

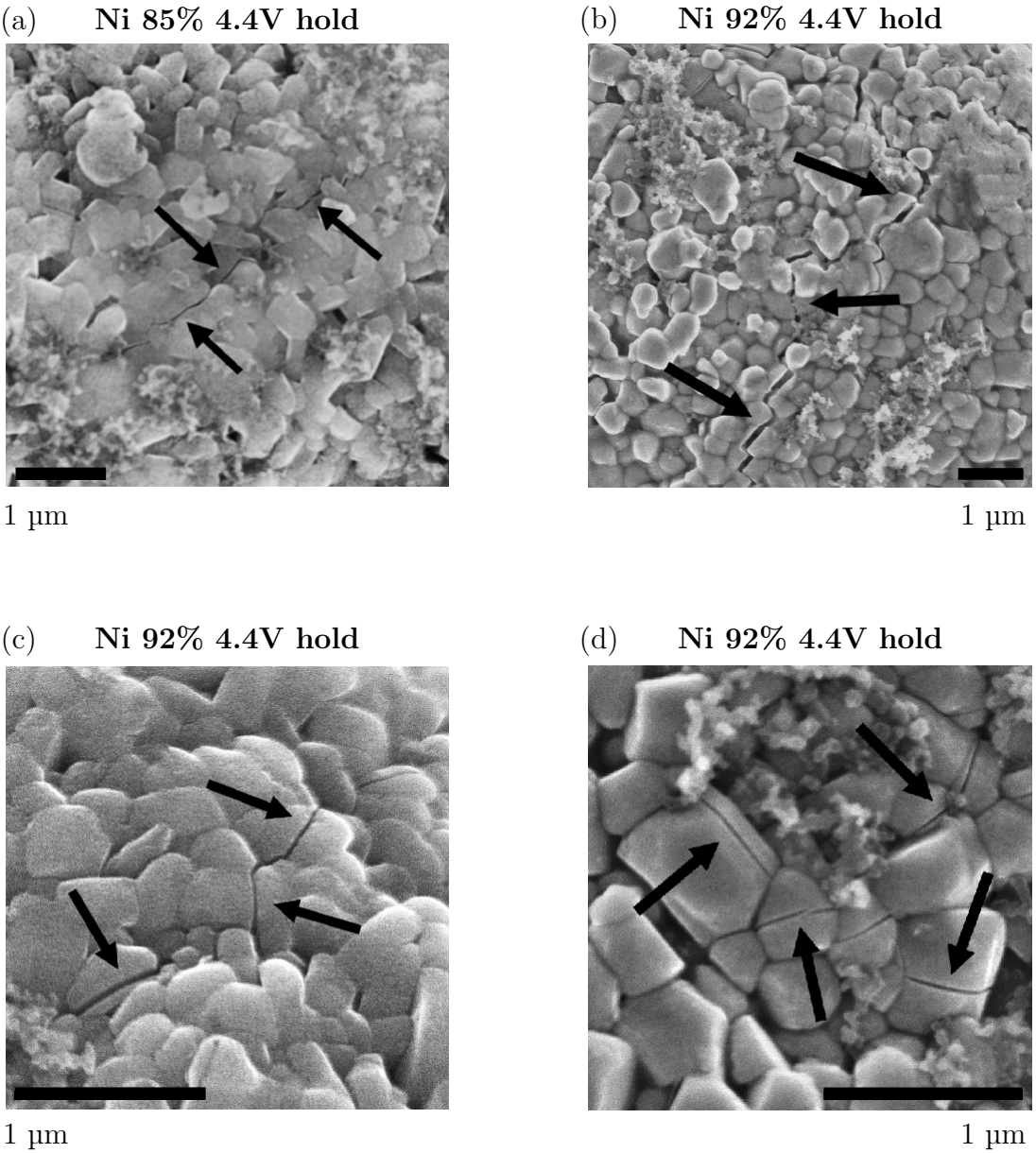

Figure 4.3: Surface SEM images of high-Ni materials Ni 85% (a,c) and Ni 92% (b,d) after first charge at 0.1C to an upper cutoff voltage of 4.4 V vs. Li/Li^+ with a 4-hour voltage hold at a magnification of 10,000X (a,b) or 30,000X (c,d) showing micro-cracks across primary and secondary particles.

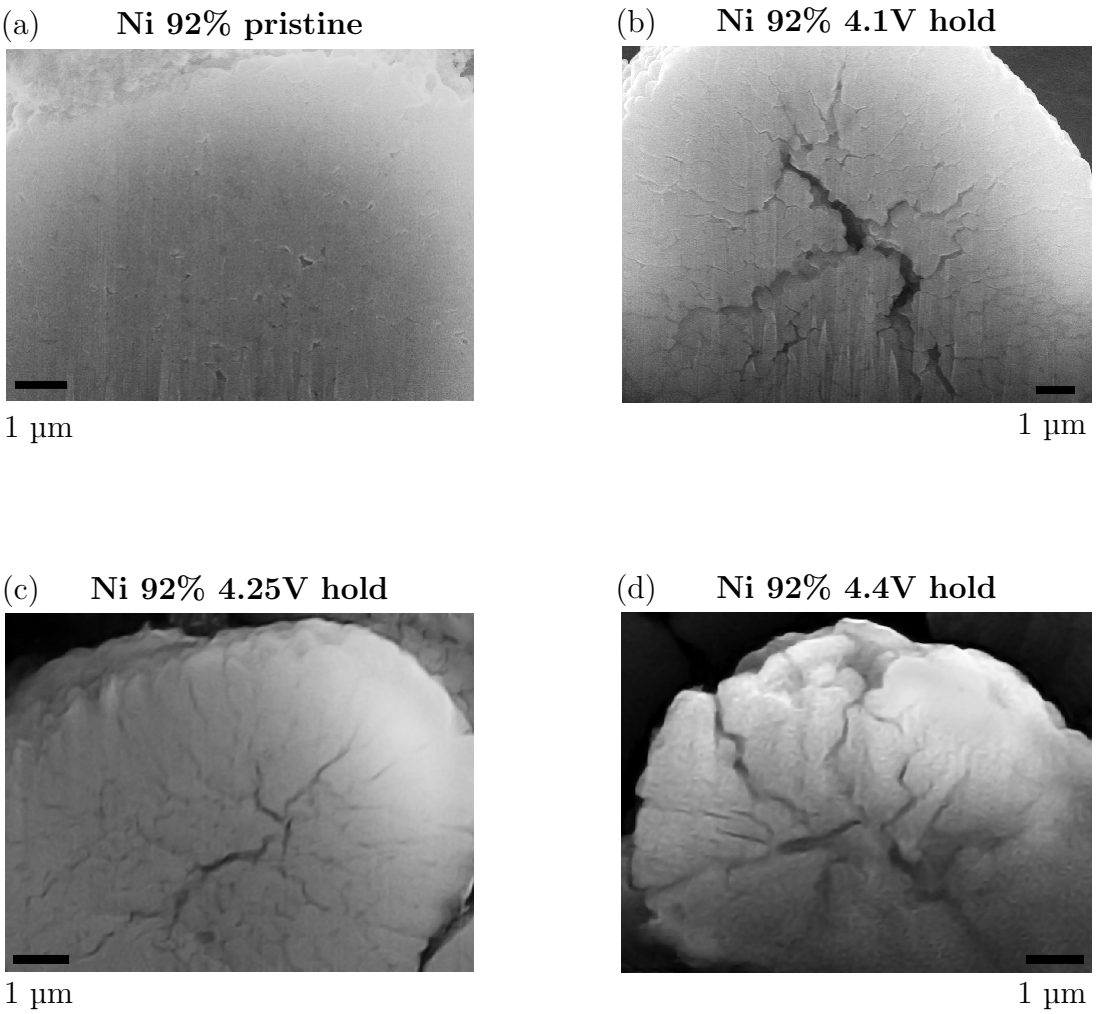

Figure 4.4: FIB-SEM cross-sectional images of Ni 92% cathodes, either pristine (a) or charged to an upper cutoff voltage of 4.1 V (b), 4.25 V (c), or 4.4 V vs. Li/Li^+ (d), showing that an internal network of micro-cracks forms and extends to the surface on the first charge.

Table 4.2: Metals dissolved from an uncharged Ni 92% cathode after 24h in 10M H_2SO_4

Metal	Initial (mg) *	Dissolved (mg) **	% Dissolved
Cobalt	0.146	0.103	71 ± 9%
Manganese	0.054	0.053	98 ± 11%
Nickel	2.67	2.37	89 ± 3%

* Calculated based on the cathode mass and stoichiometry
** Detected by the ICP and scaled to account for dilution

While TiMS was originally intended as a surface technique, ICP results for the solution remaining 24 hours after adding acid to an extracted cathode show that as a result of acid exposure, the particles of active material almost entirely dissolve into solution within 24 hours regardless of the cathode state of charge (Table 4.2). Thus, instead of reporting the total amount of gas evolved during the titration as a single value, we report titration data as a function of time within the first few hours after acid injection.

Interestingly, carbonate titration data (as measured by TiMS using 10M H_2SO_4) not only shows a peak immediately after acid injection corresponding to near-surface or easily accessible carbonates, but a second, broader peak is observed as well (Figure 4.5a). This peak fluctuates as a function of cathode state of charge and also shows some variation between repeated samples, likely due to differences in cathode thickness and porosity. The second peak can be suppressed by using more dilute acid (Figure 4.5b), which also limits active material dissolution as observed by SEM and ICP (Figure 4.14, Table 4.3). Based on the timescale of particle breakdown shown by SEM (Figure 4.6), the appearance of the second peak coincides with the dissolution of particles, implying that there are carbonates buried deep inside the particle that can only react with the acid solution once the particle has been substantially broken down.

For Ni 92% cathodes, a trend is apparent in the second peak during the first cycle. In the pristine cathode, the second peak can be attributed to residual carbonates from cathode synthesis that are located deep inside the particle. During the first charge, the second peak slowly disappears (Figure 4.7a), and during the subsequent discharge, it reappears (Figure 4.7b). Together, these data imply a cycle of carbonate oxidation and deposition on internal surfaces of the particle during charge and discharge, respectively. Continued CO_2 evolution over the first few cycles (Figure 4.15) supports this theory. Note that the disappearance of the second peak occurs slightly earlier on charge than the onset of CO_2 outgassing, implying that CO_2 produced by internal carbonate oxidation accumulates inside micro-cracks until they reach the particle surface, at which point the CO_2 gas is released.

Putting these results together with the carbonate oxidation and deposition cycle and the outgassing and particle cracking results presented earlier, we hypothesize that the extension of internal cracks to the particle surface at high voltage results in the release of trapped CO_2 from buried carbonate oxidation as well as deposition of new carbonates inside the opened

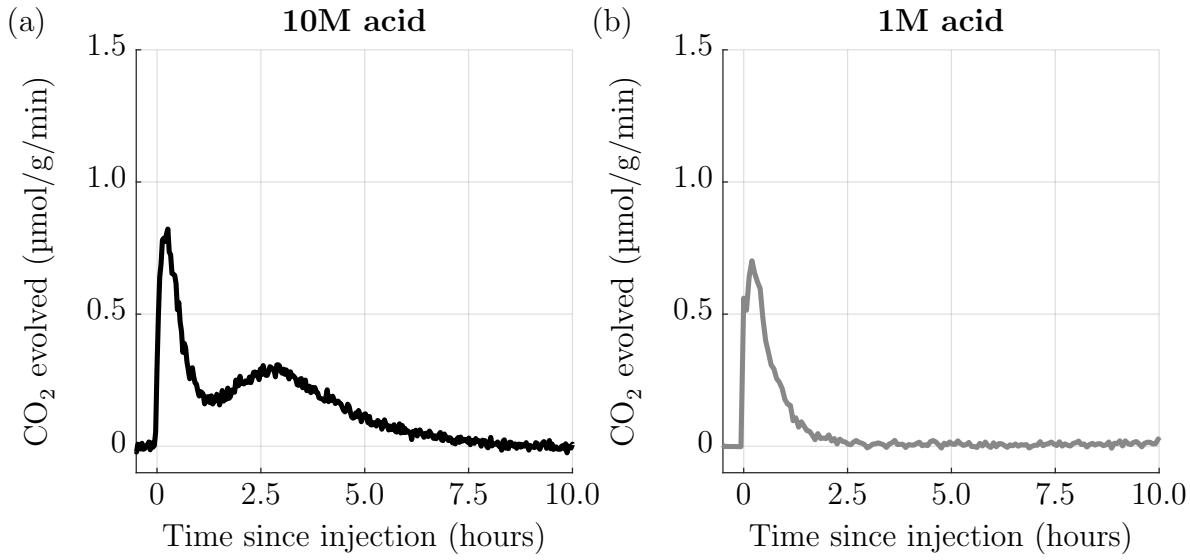

Figure 4.5: TiMS data for a pristine Ni 92% cathode in 10M H_2SO_4 (a) showing an initial peak and a second, broader peak and in 1M H_2SO_4 (b) showing only an initial peak. The increased amount of particle dissolution in the stronger 10M acid as compared to the weaker 1M acid explains the presence or absence of the second peak representing buried carbonates.

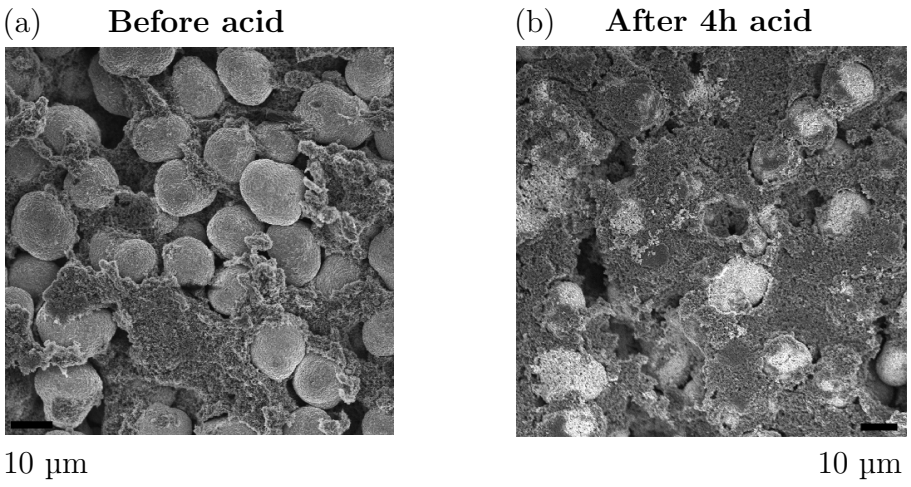

Figure 4.6: SEM images of Ni 92% cathodes cycled to an upper cutoff voltage of 4.2 V vs. Li/Li^+ before (a) and after (b) four hours of exposure to 10M sulfuric acid showing breakdown and dissolution of particles of active material from the cathode by the acid.

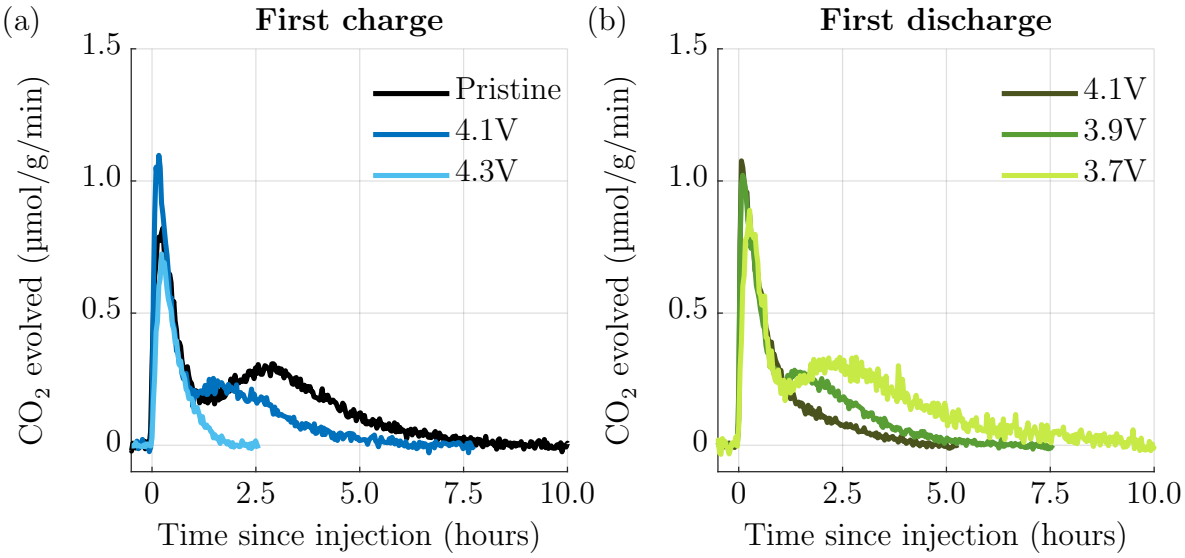

Figure 4.7: TiMS data for a Ni 92% cathode extracted and titrated in 10M H_2SO_4 at various voltages during the first charge to 4.5 V vs. Li/Li^+ (a) and the subsequent discharge to 2.5 V vs. Li/Li^+ (b). The second, broader peak representing buried carbonates disappears on charge and reappears on discharge, showing the oxidation and deposition of carbonates deep inside particles of active material during the first cycle.

cracks due to reaction with the electrolyte. During discharge, the cracks re-seal [17] (Figure 4.13), making the newly deposited carbonates inaccessible to the acid solution during a TiMS titration until significant particle dissolution has occurred and resulting in the redevelopment of the second carbonate peak. An open question remains as to whether buried carbonates might destabilize their local environment, either by physically blocking complete re-sealing of the previous cracks or by creating pressurized internal voids when they oxidize to produce CO_2, thereby encouraging re-formation of the same cracks on subsequent cycles.

In contrast to the ever-evolving carbonate oxidation and deposition process, there is a stark absence of peroxo-like oxidized oxygen in the cathode for every material and cutoff voltage tested in this study. Upon acid injection, an extremely small O_2 peak is observed along with an N_2 peak four times as large, with the ratio between the two corresponding to their ratio in air (Figure 4.16). These signals are attributed to a slight breach of the air-tight vessel that occurs during the acid injection process. Since no peroxo-like oxidized oxygen is detected, the mechanism of oxygen release must be different than that previously observed for lithium-rich materials [57], in which peroxo-like oxygen builds up in the cathode prior to oxygen release. Note that this result does not rule out electron transfer from oxygen to nickel; it simply means that no oxidized oxygen is formed, in agreement with prior work which shows that excess lithium is necessary to stabilize peroxo-like O-O bonds [60]. However, it does rule out trapped oxygen gas [61], which, if formed inside the particle, would be detected shortly after the particles were broken apart by acid during the titration. Therefore, oxygen may

participate in charge compensation via increased covalency with nickel [62], but no trapped oxygen gas or oxidized oxygen species are formed.

4.5 Conclusion

In this work, we used gas evolution techniques to investigate the degradation processes occurring at high voltage for high-Ni cathode materials. While previous studies have focused on the H2 $\rightarrow$ H3 phase transition at 4.2 V vs. Li/Li^+ as the primary cause of degradation in these materials, we do not observe gas evolution until further delithiation after the phase transition is completed. Notably, SEM images show that the onset voltage of gas evolution coincides with the extension of internal micro-cracks to the cathode surface. The ability of internal micro-cracks to breach the particle surface may be related to (i) severe volume change associated with the H2 $\rightarrow$ H3 transition; (ii) pressure buildup inside the micro-cracks as a result of CO_2 evolution from buried carbonate oxidation; or a combination of both. These results support the conclusion of previous work [63] that electrolyte reactivity with the cathode surface, not bulk structural changes, are the main cause of degradation in high-Ni cathode materials. However, the H2 $\rightarrow$ H3 phase transition clearly plays a role in the degradation mechanism that results in gas evolution, as demonstrated by the absence of both in the Ni 65% material included as a control.

Further investigation using acid titrations of extracted cathodes shows complex behavior of carbonates in these materials, with CO_2 gas released both immediately after acid injection and after a few hours of acid exposure, with the onset of the second peak of CO_2 evolution coincident with the dissolution of particles of active material from the carbon and binder matrix into the acid solution. The evolving nature of this second peak throughout the first cycle implies that it is related to the opening and closing of micro-cracks and electrolyte reactivity, although additional work is needed to better characterize this relationship.

Lastly, we showed that oxygen anionic behavior in high-Ni materials differs significantly from that in Li-rich materials, with a distinct absence of oxidized oxygen in high-Ni materials. While this finding does not rule out electron transfer from nickel to oxygen at high voltage, it demonstrates that the formation of oxygen gas in high-Ni materials does not occur through a peroxo-like intermediate as in Li-rich materials. The coincident onset of O_2 and CO_2 gas for all materials studied implies that a single mechanism is responsible for the production of both gases, but additional work is needed to better understand this mechanism.

Although the boron-based surface coating applied to these commercial grade materials is beneficial in reducing CO_2 outgassing, micro-cracks expose new, unprotected surfaces to the electrolyte, limiting the usefulness of the coating in preventing outgassing at high voltages where internal cracks reach the particle surface. In order to more effectively address this issue, the mechanism by which cracks propagate to the particle surface needs to be better understood in order to develop methods to reinforce the particle surface against cracking.

4.6 Supporting Information

4.6.1 First charge gas evolution

In order to demonstrate that cathode materials which are not considered high-Ni ($LiNi_x TM_{(1-x)}O_2$ where x < 0.8) do not evolve gas up to 4.5 V vs. Li/Li^+ on first charge, experiments analogous to those run on high-Ni materials Ni 85% and Ni 92% in the main text (Figure 4.2) were also run on a control material, Ni 65%. Both the gas evolution observed for the high-Ni materials and the 4.2 V plateau characteristic of the H2 → H3 transition are absent for this control material (Figure 4.8).

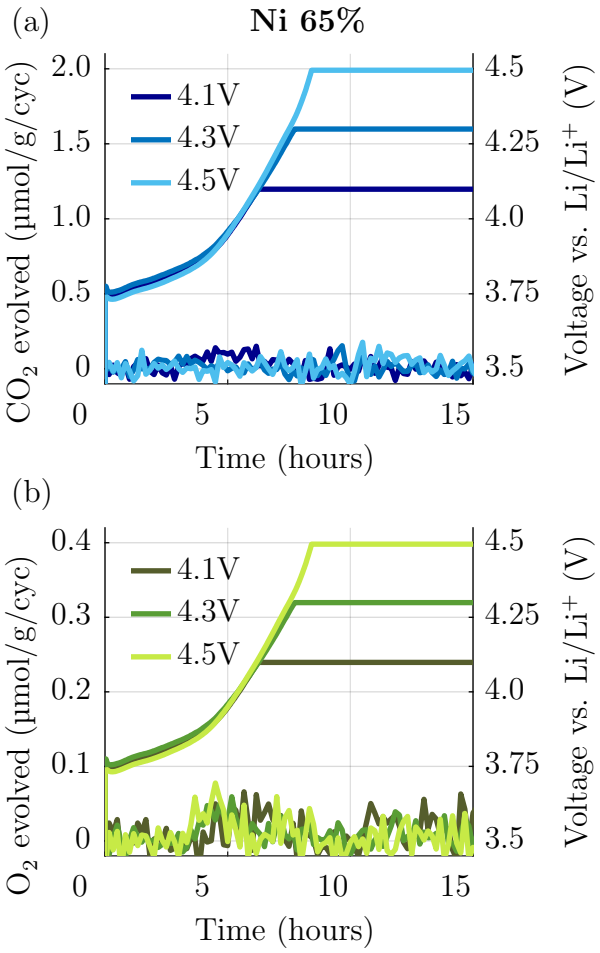

Figure 4.8: DEMS results for the first charge at 0.1C to various cutoff voltages for control material Ni 65% showing no CO_2 (a) or O_2 (b) gas evolution aside from a small amount of O_2 evolved at low voltage, which is attributed to the boron-based surface coating.

To clarify that the two high-Ni materials tested in this study, Ni 85% and Ni 92%, begin to evolve gas at slightly different voltages during the first charge, a linear voltage sweep was

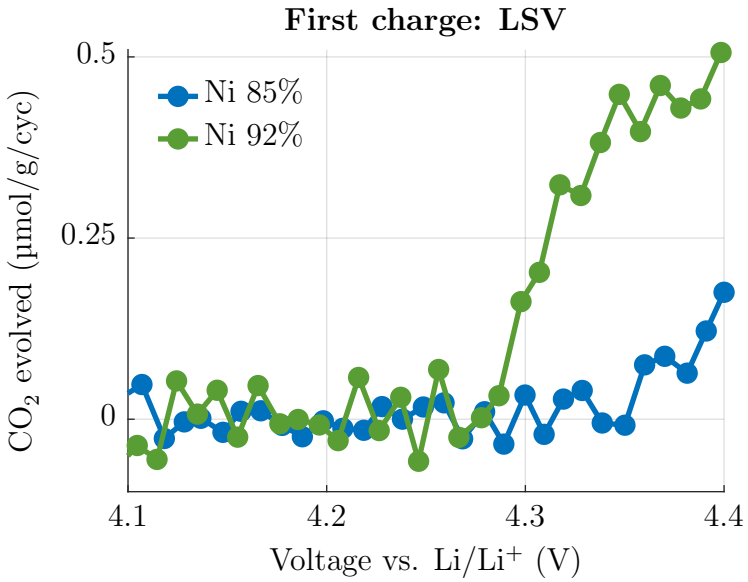

Figure 4.9: DEMS result for the first charge with a linear sweep rate of 1 mV/s to 4.4V vs. Li/Li^+ showing a clear difference in CO_2 onset between Ni 85% (blue) and Ni 92% (green). In both cases, CO_2 evolution begins at a higher voltage than the H2 → H3 transition.

run under the same conditions as the constant current experiments shown in Figure 4.2 for both materials. Since more data is collected in the voltage range of interest with this charge method, the difference in onset voltage of CO_2 gas between the two materials can be seen more clearly (Figure 4.9).

As mentioned in the main text, isotopic tagging methods that involve exposure to high temperature could not be used for these materials because the boron-based surface coating was found to decompose at such conditions. Nevertheless, the attempted isotope tagging experiment at high temperature was useful because it demonstrated that the coating mitigates CO_2 evolution (Figure 4.10a) and evolves a small amount of O_2 gas at low voltage (Figure 4.10b). However, as the surface coating was not the main focus of this study, these results were not studied further and this procedure was replaced with a room-temperature procedure for isotopic tagging.

4.6.2 Particle cracking

In contrast to the two high-Ni materials studied (Figure 4.3), SEM images of control material Ni 65% showed no surface cracking up to 4.4 V vs. Li/Li^+ (Figure 4.11). The striking difference between the surfaces of the high-Ni materials and that of the control material implies that the H2 → H3 transition, which only occurs in high-Ni materials, contributes to crack formation.

While extensive surface cracks are evident at 4.4 V vs. Li/Li^+ for both high-Ni materials

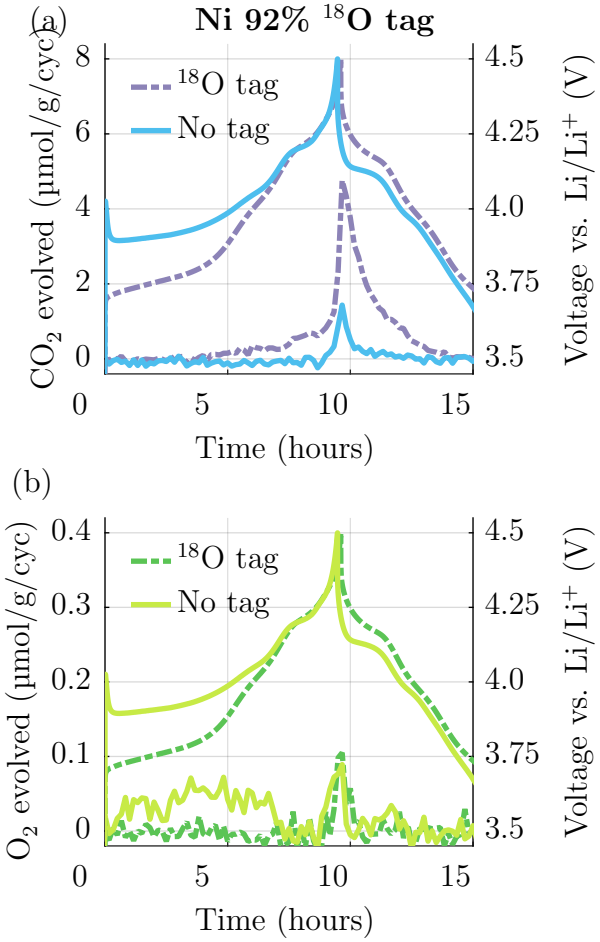

Figure 4.10: DEMS results for the first charge at 0.1C for high-Ni material Ni 92% with and without exposure to $^{18,18}O_2$ gas at 800 °C to produce an isotopically tagged material. The large increase in CO_2 evolution (a) as well as the disappearance of the initial O_2 peak (b) show that the high temperature has decomposed the boron-based surface coating.

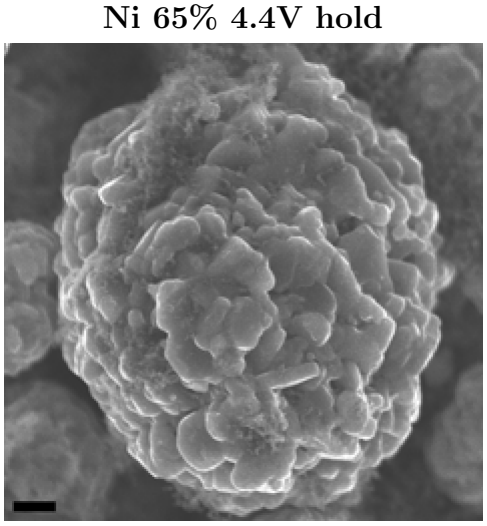

Figure 4.11: SEM image of a Ni 65% particle after a 0.1C charge to 4.4 V vs. Li/Li^+ followed by a 4-hour hold. In contrast to the high-Ni materials, the Ni 65% control material does not show surface cracking at any of the voltages tested.

(Figure 4.3), samples charged to upper cutoff voltages (with a 4-hour voltage hold) below the onset of gas evolution did not show any surface cracking (Figure 4.12). Interestingly, there was no obvious change between the 4.1 V and 4.25 V samples despite being on opposite sides of the H2 $\rightarrow$ H3 transition. While the phase transition likely destabilizes the active material structure in some way, this data shows that that surface cracking is not an immediate result of that destabilization.

Even after surface cracking occurs at high voltage (Figure 4.3), SEM images taken during the first discharge show that the cracks re-seal such that they are no longer visible on the particle surface (Figure 4.13). For these experiments, a 4-hour hold was applied at 4.5 V vs. Li/Li^+ to ensure that surface cracks would form before discharging and applying an additional 4-hour hold at the lower cutoff voltage.

4.6.3 Acid titrations

Additional titration experiments were performed with more dilute (1M) acid than the usual 10M acid to better understand how acid exposure affects the cathode structure. Note that the strong acid was originally chosen to prevent isotopic exchange between the cathode and the acidic solution by reacting faster than the isotope exchange rate [30]. After 24h of dilute acid exposure, both the acidic solution and the cathode were analyzed via ICP and SEM, respectively (Table 4.3 and Figure 4.14). Both techniques showed significantly less active

(a) **Ni 85% 4.1V hold**

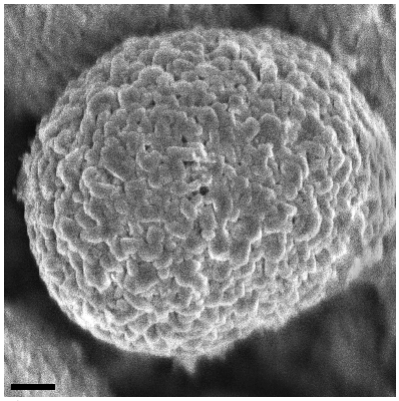

(b) **Ni 92% 4.1V hold**

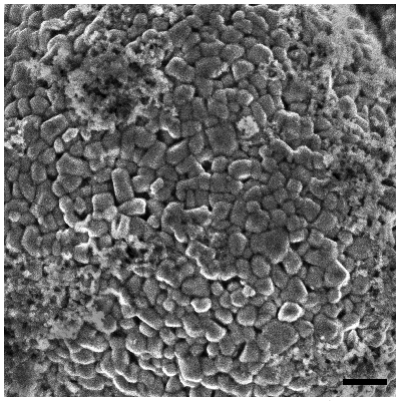

(c) **Ni 85% 4.25V hold**

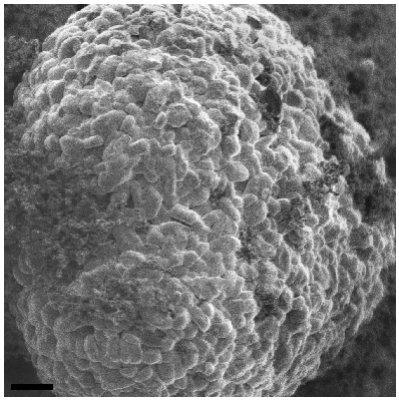

(d) **Ni 92% 4.25V hold**

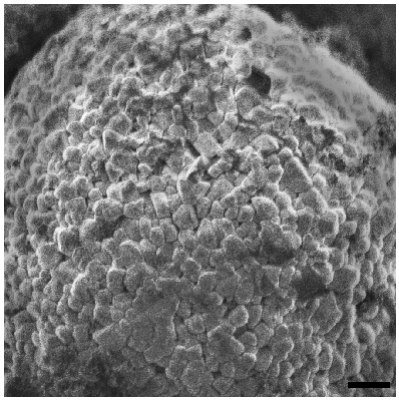

Figure 4.12: Surface SEM images of high-Ni materials Ni 85% (a,c) and Ni 92% (b,d) charged to an upper cutoff voltage of 4.1 V vs. Li/Li^+ (a,b) or 4.25 V vs. Li/Li^+ (c,d) followed by a 4-hour hold. Despite the completion of the H2 $\rightarrow$ H3 transition at 4.25 V, no surface cracking (or gas evolution) is evident at this voltage.

(a) **Ni 92% 4.1V discharge**

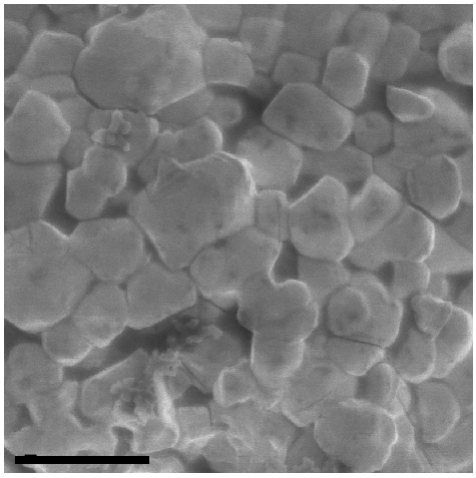

1 µm

(b) **Ni 92% 3.9V discharge**

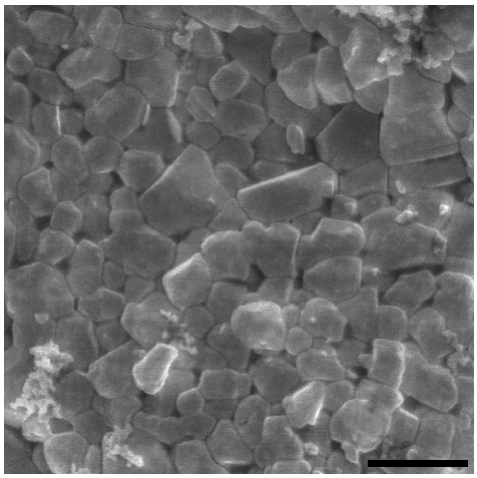

1 µm

Figure 4.13: Surface SEM images of high-Ni material Ni 92% charged at 0.1C to an upper cutoff voltage of 4.5 V vs. Li/Li^+, held for 4 hours, discharged at 0.1C to a lower cutoff voltage of 4.1 V (a) or 3.9 V (b) vs. Li/Li^+, and held for another 4 hours. In contrast to the obvious cracks observed in the charged state, after partial discharge the cracks appear to have re-sealed.

Table 4.3: Metals dissolved from an uncharged Ni 92% cathode after 24h in 1M H_2SO_4

Metal	Initial (mg) *	Dissolved (mg) **	% Dissolved
Cobalt	0.133	0.046	34 ± 4%
Manganese	0.050	0.010	20 ± 6%
Nickel	2.43	1.13	46 ± 2%

* Calculated based on the cathode mass and stoichiometry
** Detected by the ICP and scaled to account for dilution

material dissolution for the more dilute acid, supporting the hypothesis that the second peak in CO_2 evolution observed only for 10M acid samples (Figure 4.6) is related to the carbonates located deep inside the particle rather than near the particle surface.

A three-cycle DEMS experiment was performed for the Ni 85% and Ni 92% materials to determine whether gas evolution and the accompanying degradation processes continue over subsequent cycles. While no O_2 evolution was observed after the first cycle, continued CO_2 evolution (Figure S8) supports the theory that carbonates deposited onto the cathode at high voltage via electrolyte degradation oxidize on the subsequent charge to produce additional CO_2. Interestingly, a lower voltage CO_2 peak is evident for Ni 92%, implying that carbonates have been deposited on top of the surface coating.

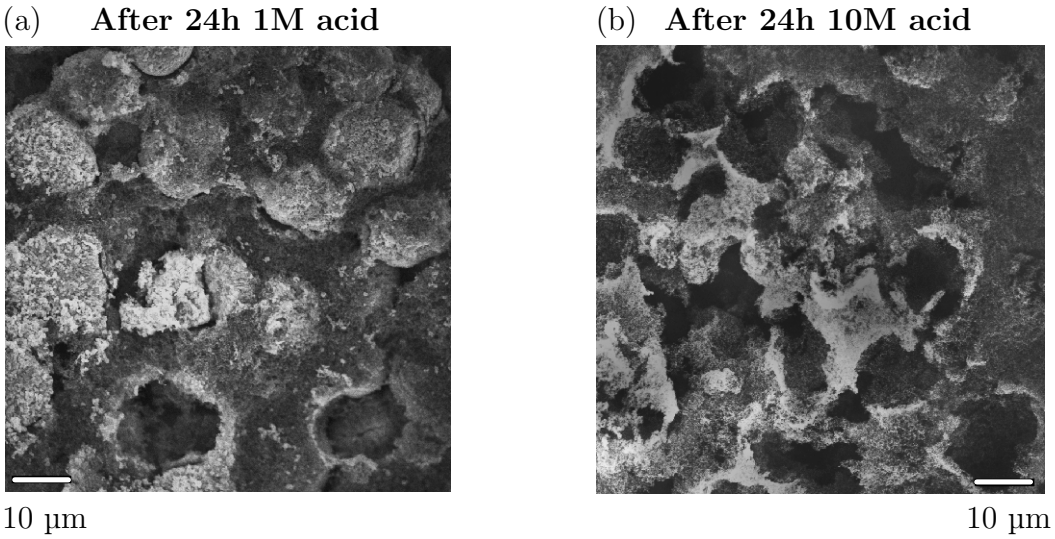

Figure 4.14: SEM images of pristine Ni 92% cathodes after 24h of exposure to 1M (a) or 10M (b) sulfuric acid showing less severe particle breakdown for the more dilute acid.

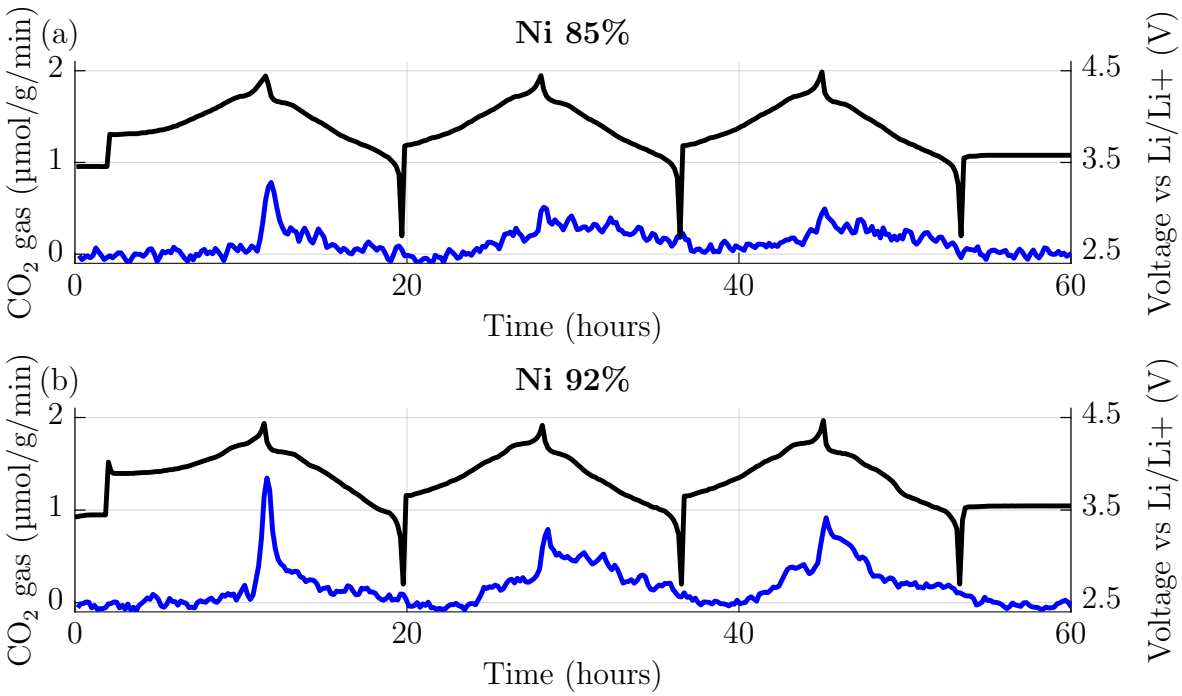

Figure 4.15: CO_2 gas evolution over the first three cycles from 2.7 to 4.5 V vs. Li/Li^+ for Ni 85% (a) and Ni 92% (b) showing continued outgassing.

A signal at mass channel m/z = 32 observed during acid titration is typically attributed to the reaction of acid with peroxo-like oxygen present in the active material to form O_2 gas. However, a small amount of air is unavoidably let into the sealed vessel in the moment of acid injection, which also produces a small signal at m/z = 32. In order to clarify that the signal observed in this study is attributable to air, not to peroxo-like oxygen, a signal attributed only to nitrogen, m/z = 14, is scaled to show that the N_2 and O_2 gas signals exactly overlap (Figure 4.16) with their ratio equal to that between N_2 and O_2 in air. This same ratio was maintained for every titration in this study, confirming the absence of peroxo-like oxygen in this system.

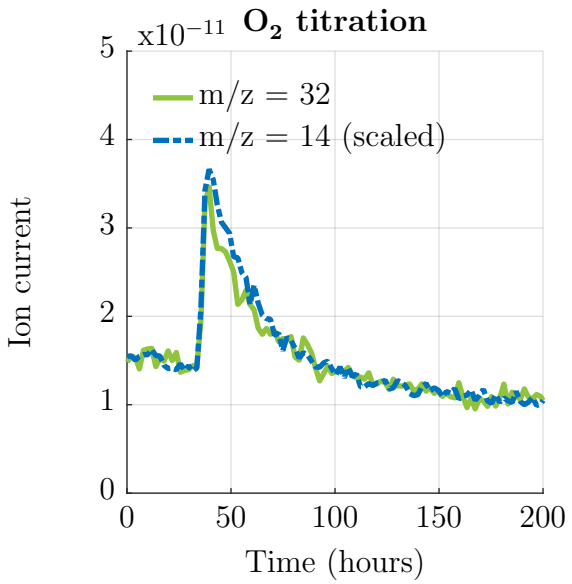

Figure 4.16: Ion current detected at mass channels m/z = 32 (oxygen gas) and m/z = 14 (nitrogen gas) during an acid titration for a Ni 92% cathode charged to 4.1 V vs. Li/Li^+. After scaling by the ratio of nitrogen to oxygen in air, the two signals completely overlap, showing that all the oxygen present is from air, not peroxo-like oxygen in the cathode.

5 Single crystal high-nickel materials show crack propagation from grain boundaries in particle agglomerates

5.1 Abstract

Single crystal particles are of great interest in the field of high-nickel cathode materials because the primary degradation mechanism of polycrystalline particles is a result of structural instability, a drawback that single crystal morphologies are intended to address by eliminating grain boundaries. The change in morphology has been shown to increase capacity retention and decrease outgassing from high-nickel materials, but at the cost of a more difficult synthesis process. In this work, we compare single crystal and polycrystalline high-nickel cathode materials with similar nickel content to determine which degradation mechanisms are suppressed by the change in morphology and which remain. Contrary to the accepted belief that the change in morphology prevents particle cracking, we observe crack propagation along the grain boundary of single crystal particles that have agglomerated. This observation implies that the same degradation mechanism as in polycrystalline materials, in which particle cracking and outgassing are linked, is still active but to a lesser extent in single crystal materials. Therefore, more work is needed to optimize single crystal high-nickel materials to produce cathodes in which active material particles are well-dispersed rather than aggregated.

5.2 Introduction

Single crystal high-Ni cathode materials are cathode materials with similar chemical formulas to polycrystalline materials but with a significantly altered morphology. Unlike the polycrystalline structure in which larger secondary particles (around 10 µm diameter) contain many smaller primary particles, single crystal materials are made up of large primary particles (3-5 µm diameter) with no secondary particles. Single crystal materials have been the subject of recent research because their simpler micro-structure partially mitigates the outgassing and capacity fading observed in polycrystalline high-Ni cathode materials [64, 65]. This improvement is thought to be attributable to the absence of grain boundaries, which in polycrystalline materials are the site of inter-granular cracking at higher voltages ($\geq$ 4.3 V vs. Li/Li$^+$). As described in the previous chapter, particle cracking is strongly correlated with gas evolution in polycrystalline materials, so it follows that the decreased gas evolution observed in single crystal materials is likely due to the lack of inter-granular cracking in single crystal morphologies.

While inter-granular cracking has only been observed in polycrystalline materials, intra-granular cracking may still occur in single crystal materials when charged to very high

Table 5.1: Particle size comparison between polycrystalline and single crystal materials

Material	Polycrystalline	Single crystal	
	Ni 92%	Ni 93%	Ni 96%
D50 *	12-13 µm	4.2 µm	4.0 µm

* D50 data from LG Energy Solution.

voltages ($\geq$ 4.7 V vs. Li/Li$^+$) [58, 66]. However, this type of cracking cannot explain the outgassing observed from single crystal materials at a similar voltage to polycrystalline materials ($\geq$ 4.3 V vs. Li/Li$^+$), nor the capacity fade when cycled to more reasonable upper cutoff voltages [64, 65]. Although these indicators of cathode degradation are lessened in the case of single crystal materials, their similar effect on both morphologies implies that the degradation processes in polycrystalline materials may also be active in single crystal materials but to a lesser extent.

In this work, we present gas evolution studies on three high-Ni NMC materials under development for commercial use: polycrystalline Ni 92% ($LiNi_{0.92}Mn_{0.02}Co_{0.04}Al_{0.02}O_2$), used as a comparison; and single crystal Ni 93% ($LiNi_{0.934}Mn_{0.023}Co_{0.043}O_2$) and Ni 96% ($LiNi_{0.96}Mn_{0.01}Co_{0.03}O_2$). Consistent with previous reports, the single crystal material shows a much larger primary particle size, only a few times smaller than the secondary particle size of the polycrystalline material (Table 5.1). In agreement with previous studies, we show decreased gas evolution from single crystal materials as compared to their polycrystalline analogues. However, we observe by SEM that grain boundaries still exist in single crystal materials within those particles that are agglomerated together. Not only do these interfaces seem to expand during charge, but they also form nucleation points for further cracking within the monolithic single crystals themselves. This work highlights the importance of particle dispersion within the carbon-binder matrix in order to fully realize the advantage of single crystal materials in terms of cracking and outgassing.

5.3 Experimental methods

5.3.1 Materials and cell construction

Both single crystal and polycrystalline high-Ni materials were synthesized by LG Energy Solution and received in powder form. While the polycrystalline materials have a complex microstructure of primary and secondary particles (see SEM images from Chapter 4), the single crystal materials are composed of larger primary particles only (Figure 5.1).

Swagelok-type cells [12, 57] were assembled with cathodes composed of 90 wt% active material (polycrystalline Ni 92% or single crystal Ni 93% or 96% powder), 5 wt% carbon black (Super P), and 5 wt% polyvinylene fluoride binder coated onto stainless steel mesh. The electrolyte used was 1 M $LiPF_6$ in a 1:1 mixture by weight of ethylene carbonate and diethyl carbonate (Gotion). Cells were assembled with two separators, one polypropylene

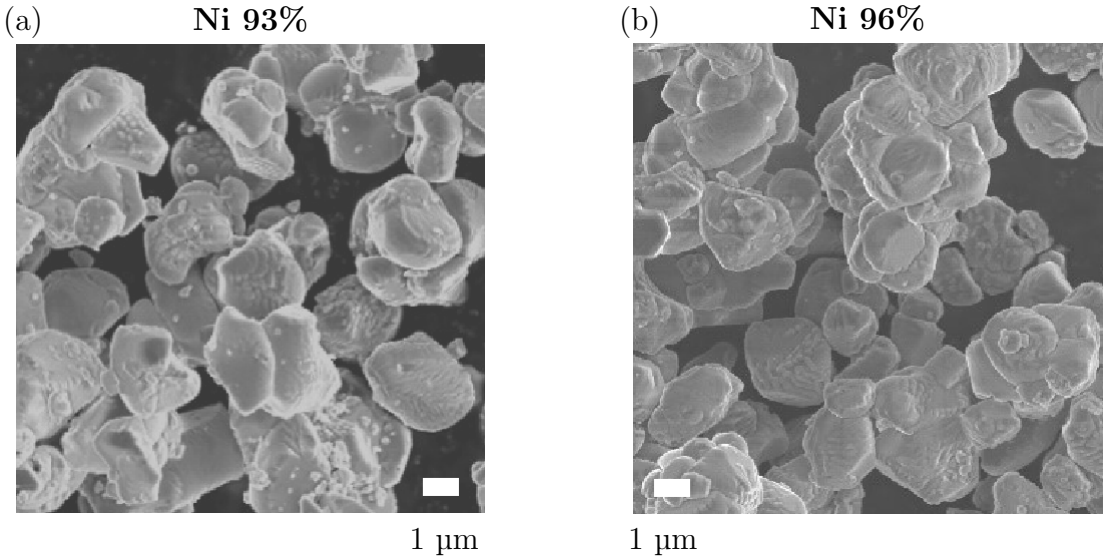

Figure 5.1: SEM images of pristine single crystal materials Ni 93% and Ni 96% showing primary particles of around 4 µm. Images provided by LG Energy Solution.

(Celgard 2500) and one glass fiber (Whatman), with the Celgard in direct contact with the cathode. Lithium metal (FMC) was used as the anode.

5.3.2 Analysis techniques

DEMS, TiMS, and SEM analysis techniques were used as described in previous chapters. See Chapter 2 for detailed information on gas evolution techniques DEMS and TiMS and Chapter 4 for SEM analysis parameters.

5.4 Results and Discussion

5.4.1 First charge gas evolution

In order to probe the effect of changing from polycrystalline to single crystal morphology, the same CCCV charging protocol was applied to polycrystalline Ni 92% and single crystal Ni 93%. Both materials were charged at a rate of C/10 to 4.5 V vs. Li/Li^+, followed by a four-hour voltage hold, while gas evolution was monitored using DEMS. Note that all of the materials studied have been treated with coatings designed to prevent outgassing from surface carbonates as described in Chapter 4. A notable difference in CO_2 evolution is evident between the two morphologies (Figure 5.2a), with considerably less CO_2 evolving from the single crystal Ni 93% as compared to the polycrystalline Ni 92%. This result cannot be attributed to differences in surface area, as both materials have coatings designed to prevent outgassing from the surface and therefore outgassing is expected only from newly exposed surface due to particle cracking. As observed for polycrystalline high-Ni materials in Chapter

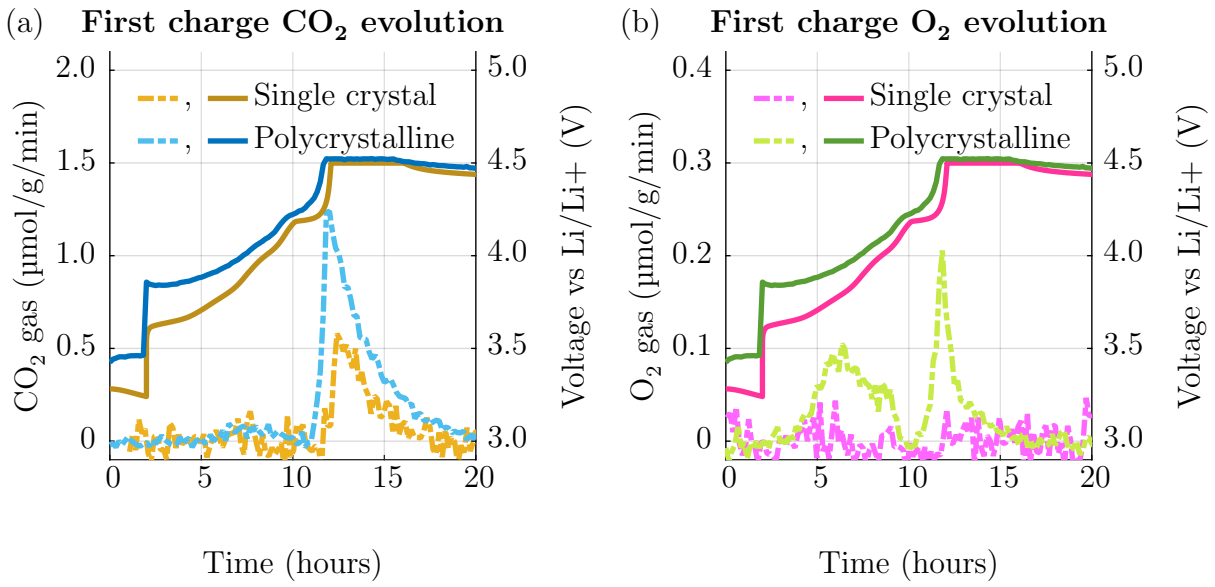

Figure 5.2: First charge CO_2 (a) and O_2 (b) outgassing for polycrystalline Ni 92% and single crystal Ni 93% showing reduced outgassing for the single crystal material.

Table 5.2: First cycle gas evolution for polycrystalline Ni 92% and single crystal Ni 93%

Material	Ni 92% (polycrystal)	Ni 93% (single crystal)
CO_2 evolved	20 umol/g	7.5 umol/g
O_2 evolved	1.5 umol/g	0 umol/g
Onset voltage	4.30 V	4.23 V

4, there is a sudden onset of gas evolution after the voltage plateau characteristic of the H2 → H3 phase transition, implying that the phase transition plays a role in destabilizing the cathode particle and allowing cracks to percolate through it.

Consistent with the lower overpotential observed throughout the first charge, the H2 → H3 voltage plateau is lower and more pronounced for single crystal Ni 93% than for polycrystalline Ni 92%. As a result, the onset voltage of CO_2 evolution is also lower (Table 5.2) although the state-of-charge at which CO_2 evolution begins (about 85% delithiated) is similar for both materials. In addition to the reduction in CO_2 outgassing, the single crystal Ni 93% shows no O_2 outgassing (Figure 5.2b), a reduction from the already small amount of O_2 evolved from the polycrystalline Ni 92%. These results confirm that the change in morphology results in reduced outgassing; however, the similar CO_2 outgassing behavior implies that the same mechanism is occurring in both cases.

Together with the DEMS data presented above, TiMS experiments show that the difference in surface carbonate content before and after the first charge matches closely with the

Table 5.3: Carbonate content during the first charge for single crystal materials

Material	Carbonate			CO_2 gas
	Pristine	4.5V charge	Difference	4.5V charge
Ni 93% (single crystal)	22.3 umol/g	13.9 umol/g	8.4 umol/g	7.5 umol/g
Ni 96% (single crystal)	34.3 umol/g	23.6 umol/g	10.7 umol/g	9.5 umol/g

amount of CO_2 gas evolved during the first charge for both single crystal materials studied (Table 5.3). While this data does not provide as concrete evidence of the source of CO_2 gas as an isotopic labeling experiment would (see Table 4.1), it strongly implies that the surface carbonate oxidation, rather than electrolyte decomposition, is more or less exclusively responsible for CO_2 evolution in single crystal materials, in contrast to the mix of sources of CO_2 seen for polycrystalline materials. Not only does this result support the idea that electrolyte penetration and reaction with the cathode surface is greatly reduced in single crystal materials as compared to polycrystalline materials, but it also indicates that the O_2 evolution observed in polycrystalline materials must be a result of electrolyte reactivity with the cathode surface since it is clearly not produced via carbonate oxidation.

5.4.2 Observation of cracking by SEM

In the previous chapter, surface cracking was shown to be correlated with outgassing for polycrystalline high-Ni materials. Since we see a significant reduction in CO_2 outgassing in single crystal materials as compared to polycrystalline materials, we would expect particle cracking to still occur, but to a much lesser extent, in single crystal materials were the same mechanism to be active in both cases.

SEM images confirm that some cracks are visible in charged single crystal materials. Remarkably, the cracks are inter-granular and only develop along grain boundaries where single crystal particles are agglomerated together. As seen from Figure 5.1, groups of two or more agglomerated particles are fairly common and easily identified among the lone particles. Since the crystallographic planes are not aligned between the agglomerated particles, grain boundaries are present at the interface between the particles (Figure 5.3a). Interestingly, these interfaces appear to expand slightly during the first charge to 4.5 V vs. Li/Li^+ to create space between the agglomerated particles as shown in Figure 5.3b. In order to determine whether the expansion seen from the grain boundaries is significant, charged cathodes were cross-sectioned for further study.

As expected, cross-sectional SEM images of lone particles taken after the first charge to 4.5 V vs. Li/Li^+ show an extremely smooth surface with no visible cracks or voids (Figure 5.4a). Remarkably, cross-sectional SEM images of agglomerated particles from the same cathode show hairline cracks emanating from the expanded interface between the particles (Figure 5.4b). The hairline cracks are clearly related to the stacking faults not only because they intersect but because the angles of intersection are aligned with the hexagonal shape

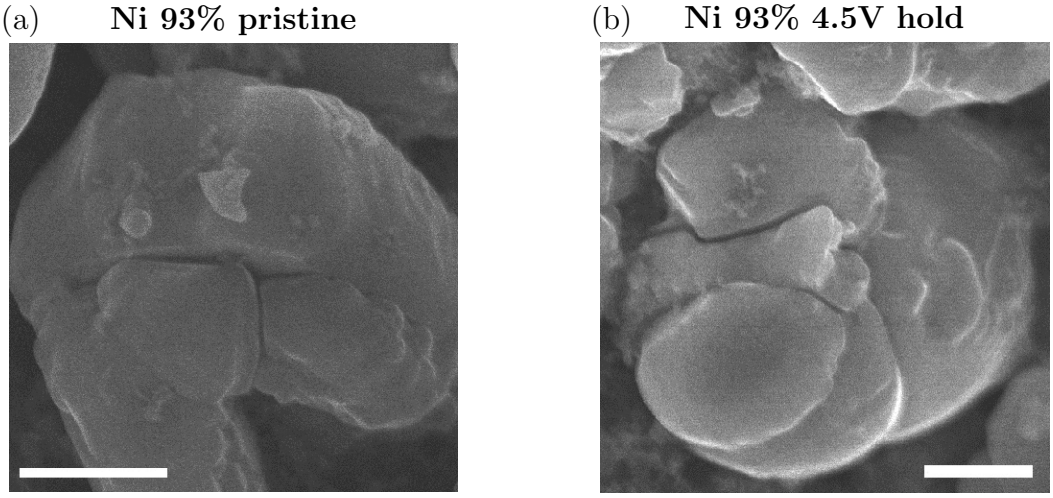

Figure 5.3: Surface SEM image of the interface between particles for pristine (a) and charged (4.5 V vs. Li/Li^+) (b) single crystal Ni 93% showing that stacking faults at the interface appear to expand to create space between the particles during charge.

of the particles. This surprising effect shows that inter-particle cracking can in fact occur in single crystal materials before 4.5 V vs. Li/Li^+, a lower voltage than the intra-granular cracking observed by others at 4.7 V vs. Li/Li^+ [58, 66].

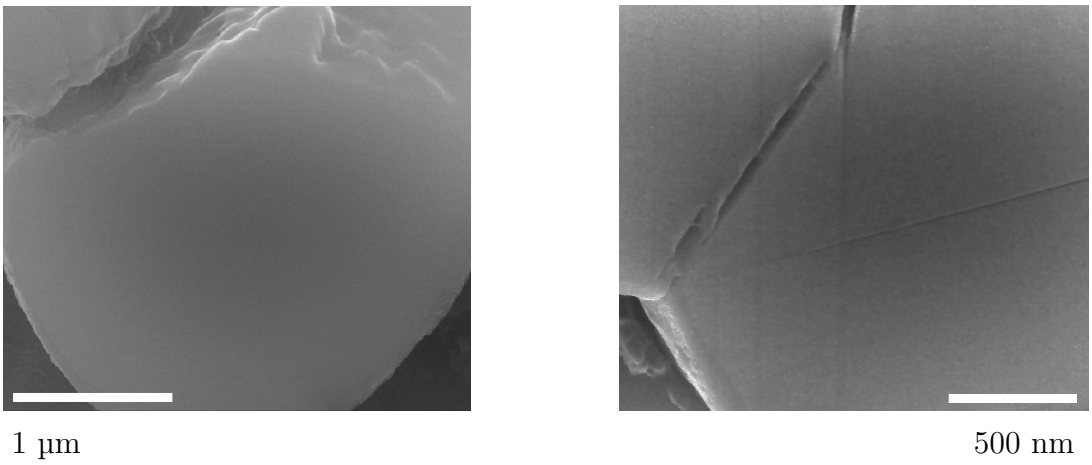

Figure 5.4: Cross-sectional SEM images of charged (4.5 V vs. Li/Li^+) single crystal Ni 96% showing that no cracks develop for lone particles (a) but that a network of hairline cracks originating at the expanded interface appears for agglomerated particles (b).

Based on the results from Chapter 4, it is expected that the cracks in fact begin at

the same voltage as outgassing begins (around 4.3 V vs. Li/Li^+), but only 4.5 V samples were tested in the interest of time. These inter-particle cracks likely expand into more complex crack networks over many cycles, exposing new surfaces to the electrolyte and evolving gas via the same mechanism as polycrystalline materials. In order to fully realize the advantage of the single crystal morphology, then, methods must be developed to prevent particle agglomeration and encourage isolation of active material particles in the carbon-binder matrix.

5.5 Conclusion

While single crystal morphologies have been a hot topic recently in high-Ni cathode studies due to the suppression of outgassing and cracking that they show as compared to analogous polycrystalline materials, much remains to be learned about the degradation mechanisms that still remain active for this morphology. This work demonstrates that the decreased outgassing from single crystal materials is due to the greatly reduced particle cracking compared to polycrystalline materials. However, cracks are still possible and propagate from grain boundaries between agglomerated particles at high voltage.

Despite their advantages, single crystal high-Ni materials need further improvement to prevent outgassing from surface carbonates as well as cracking from the intersection of agglomerated particles. Various surface coating materials such as boron [53, 54] are currently being investigated to stabilize the surface and prevent outgassing, but synthesis methods that yield well-dispersed active material particles have only been sparsely studied [67]. As the synthesis of these materials is notoriously complex already, much work remains to be done to bring single crystal high-Ni cathode technology to the industrial scale.

5.6 Supporting Information

For industrial applications, batteries undergo formation cycles to allow for outgassing before the battery is closed. As a result, the long-term effects of first-cycle outgassing as described throughout this chapter are mitigated in commercial cells to some extent. However, while removing gas from the system prevents that gas from remaining in the cell and possibly reacting with cell components, the changes caused by outgassing processes on the cathode surface remain. To learn more about the extent by which outgassing processes are mitigated by formation cycling, the CO_2 evolution on the first charge as tabulated in Tables 5.1 and 5.2 was compared to the CO_2 evolution on the fourth cycle, also to 4.5 V vs. Li/Li^+, after three formation cycles at C/10 to 4.25 V vs. Li/Li^+ (Table 5.4).

Interestingly, the formation cycling resulted in increased CO_2 evolution on the fourth cycle. While the reason for this is not obvious, it is possible that the inter-particle cracking seen for agglomerated particles causes a cycle of carbonate oxidation and deposition via electrolyte reaction with newly exposed cathode surface analogous to that observed in polycrystalline materials,. Since cracking occurs to a much lesser extent on the first charge in

Table 5.4: Effect of formation cycling on CO_2 evolution for single crystal materials

Cycle number	First *	Fourth **
Ni 93% (single crystal)	7.5 umol/g	30.3 umol/g
Ni 96% (single crystal)	9.5 umol/g	21.5 umol/g
Onset voltage	4.23 V	4.25 V

* With an upper cutoff voltage of 4.5 V vs. Li/Li^+
** With an upper cutoff voltage of 4.5 V vs. Li/Li^+ after three formation cycles to 4.25 V vs. Li/Li^+

single crystal materials as compared to polycrystalline materials, these processes may occur much more slowly and over many more cycles before an equilibrium of sorts is reached. As a result, formation cycling may be effective if continued until a stable surface is formed, which clearly requires more than the three cycles tested here. Further cycling studies are needed to determine whether this is the case.

6 Conclusions

This dissertation explored the degradation mechanisms that present obstacles in the path to commercialization in lithium-excess and high-nickel cathode materials. Gas evolution studies on these materials, as well as those that involve more drastic changes to the cathode structure, provide a scientific depth of knowledge which is essential to support the progression of these technologies from ideas to practice.

In Chapter 2, controlled addition of lithium carbonate to Li-excess NMC cathodes via exposure to isotopically tagged CO_2 gas was used to decouple bulk oxygen redox from cathode/electrolyte reactions triggered by a reactive oxygen species produced via lithium carbonate oxidation. This reactive oxygen species was shown to participate in degradation reactions mostly through an indirect route also involving lattice oxygen. As a result, this mechanism is likely unique to cathode materials that undergo bulk oxygen redox activity. Previous studies have already demonstrated that the removal of surface lithium carbonate from Li-excess cathode materials via washing has a beneficial effect on outgassing and cyclability; this work provides a scientific basis to understand why such procedures are necessary.

In Chapter 3, the effect of ball milling on the surface reactivity of Li_2MnO_3 was explored to determine whether stable cycling of this cathode material is achievable via stabilization of the cathode/electrolyte interface. While the typically quite large amount of O_2 outgassing was effectively suppressed by ball-milling with a graphitic fluoride coating, the continued CO_2 evolution as a result of carbonate oxidation and deposition is still a major concern for the long-term surface stability. However, some capacity cannot be attributed to degradation process that evolve gas, leaving open the possibility of reversible manganese redox. The ability of Li_2MnO_3 to undergo stable cycling based on manganese redox remains heavily debated, but future modifications that provide even beter surface stabilization would help to clarify this, revealing whether Li_2MnO_3 could be effective as a cathode material.

In Chapter 4, high voltage degradation processes for surface-passivated, polycrystalline high-Ni cathode materials were investigated. The onset voltage of gas evolution was found to coincide with the extension of internal micro-cracks to the cathode surface, clearly showing that electrolyte reactivity with the cathode surface (especially unprotected surfaces exposed due to cracking), not bulk structural changes, are the main cause of degradation in high-Ni cathode materials. In addition, there is complex behavior of carbonates in these materials, with buried carbonates undergoing a cycle of oxidation and deposition along with the opening and closing of micro-cracks when a voltage cutoff above the threshold of gas evolution is used. There is a distinct absence of oxidized oxygen in these materials, prompting questions about the mechanism of the coincident onset of O_2 and CO_2 gas for all materials studied. Careful analysis of oxygen activity in high-Ni materials may reveal how charge transfer between nickel and oxygen, which is proposed to occur during the H2 $\rightarrow$ H3 phase transition, could fill in some of the gaps in knowledge about high-Ni cathode materials.

In Chapter 5, single crystal high-Ni cathode materials are analyzed in comparison to the traditional polycrystalline materials studied in Chapter 4. This work demonstrates decreased outgassing from single crystal materials due to the greatly reduced particle cracking compared to polycrystalline materials; however, cracks are still possible and propagate from grain boundaries between agglomerated single crystal particles at high voltage. As a result, much work remains to be done to optimize particle dispersion within the carbon-binder matrix during the already complex synthesis of single crystal materials to fully realize the advantage of the change in morphology.

In addition to the cathode materials studied here, which represent relatively minor modifications to the standard commercial NMC cathode, materials with considerable structural changes are also under development. For example, materials that forego the layered structure in favor of a spinel or completely disordered structure effectively mitigate many of the degradation processes presented in this dissertation, but they also face unique obstacles which are being actively studied. While it is unclear how the mix of cathode technologies currently under intense study will make the transition to industry, gas evolution studies provide a deeper scientific understanding of how these materials function and thus remain a crucial part of the research and development process.

Bibliography

1. Goodenough, J. B. & Kim, Y. Challenges for rechargeable lithium batteries. *Chem. Mater.* **22,** 587–603. doi:10.1021/cm901452z (2010).
2. Tarascon, J.-M. & Armand, M. Issues and challenges facing rechargeable lithium batteries. *Nature* **414,** 359–367. doi:10.1038/35104644 (2001).
3. Goodenough, J. B. & Park, K.-S. The rechargeable Li-ion battery: a perspective. *J. Electrochem. Soc.* **135,** 1167–1176. doi:10.1021/ja3091438 (2013).
4. Jain, A. *et al.* The materials project: a materials genome approach to accelerating materials innovation. *APL Materials* **1.** doi:10.1063/1.4812323 (2013).
5. Papp, J. K. *et al.* A comparison of high voltage outgassing of $LiCoO_2$, $LiNiO_2$, and Li_2MnO_3 layered Li-ion cathode materials. *Electrochim. Acta* **368.** doi:10.1016/j.electacta.2020.137505 (2021).
6. Clément, R. J., Lun, Z. & Ceder, G. Cation-disordered rocksalt transition metal oxides and oxyfluorides for high energy lithium-ion cathodes. *Energy Environ. Sci.* **13,** 345–373. doi:10.1039/c9ee02803j (2020).
7. Hong, J., Gwon, H., Jung, S.-K., Ku, K. & Kang, K. Review—lithium-excess layered cathodes for lithium rechargeable batteries. *J. Electrochem. Soc.* **162,** A2447–A2467. doi:10.1149/2.0071514jes (2015).
8. Hy, S. *et al.* Performance and design considerations for lithium excess layered oxide positive electrode materials for lithium ion batteries. *Energy Environ. Sci.* **9,** 1931–1954. doi:10.1039/c5ee03573b (2016).
9. Luo, K. *et al.* Charge-compensation in 3d-transition-metal-oxide intercalation cathodes through the generation of localized electron holes on oxygen. *Nat. Chem.* **8,** 684–691. doi:10.1038/nchem.2471 (2016).
10. Hong, J. *et al.* Critical role of oxygen evolved from layered Li-excess metal oxides in lithium rechargeable batteries. *Chem. Mater.* **24,** 2692–2697. doi:10.1021/cm3005634 (2012).
11. Koga, H. *et al.* Different oxygen redox participation for bulk and surface: a possible global explanation for the cycling mechanism of $Li_{1.20}Mn_{0.54}Co_0.13Ni_{0.13}O_2$. *J. Power Sources.* **236,** 250–258. doi:10.1016/j.jpowsour.2013.02.075 (2013).
12. McCloskey, B. D., Bethune, D. S., Shelby, R. M., Girishkumar, G. & Luntz, A. C. Solvents' critical role in nonaqueous lithium-oxygen battery electrochemistry. *J. Phys. Chem. Lett.* **2,** 1161–1166. doi:10.1021/jz200352v (2011).
13. McCloskey, B. D. *et al.* Twin problems of interfacial carbonate formation in nonaqueous Li–O_2 batteries. *J. Phys. Chem. Lett.* **3,** 997–1001. doi:10.1021/jz300243r (2012).
14. Schipper, F. *et al.* Recent advances and remaining challenges for lithium ion battery cathodes. *J. Electrochem. Soc.* **164,** A6220–A6228. doi:10.1149/2.0351701jes (2017).

15. Ryu, H.-H., Park, K.-J., Yoon, C. S. & Sun, Y.-K. Capacity fading of Ni-rich Li[Ni_xCo_y Mn_{1-x-y}]O_2 ($0.6 \leq x \leq 0.95$) cathodes for high-energy-density lithium-ion batteries: bulk or surface degradation? *Chem. Mater.* **30,** 1155–1163. doi:10.1021/acs.chemmater.7b05269 (2018).

16. Kondrakov, A. O. *et al.* Charge-transfer-induced lattice collapse in Ni-rich NCM cathode materials during delithiation. *J. Phys. Chem. C* **121,** 24381–24388. doi:10.1021/acs.jpcc.7b06598 (2017).

17. Nam, G. W. *et al.* Capacity fading of Ni-rich NCA cathodes: effect of microcracking extent. *ACS Energy Lett.* **4,** 2995–3001. doi:10.1021/acsenergylett.9b02302 (2019).

18. Renfrew, S. E. *Tracing interfacial reactivity of lithium transition metal oxides through outgassing* PhD thesis (2019).

19. Papp, J. K. *High voltage reactivity in lithium batteries* PhD thesis (2020).

20. Muhammad, S. *et al.* Evidence of reversible oxygen participation in anomalously high capacity Li- and Mn-rich cathodes for Li-ion batteries. *Nano Energy* **21,** 172–184. doi:10.1016/j.nanoen.2015.12.027 (2016).

21. Sathiya, M. *et al.* Reversible anionic redox chemistry in high-capacity layered-oxide electrodes. *Nat. Mater.* **12,** 827–835. doi:10.1038/nmat3699 (2013).

22. Saubanére, M., McCalla, E., Tarascon, J.-M. & Doublet, M.-L. The intriguing question of anionic redox in high-energy density cathodes for Li-ion batteries. *Energy Environ. Sci.* **9,** 984–991. doi:10.1039/C5EE03048J (2016).

23. Gent, W. E. *et al.* Coupling between oxygen redox and cation migration explains unusual electrochemistry in lithium-rich layered oxides. *Nat. Commun.* **8,** 2091. doi:10.1038/s41467-017-02041-x (2017).

24. Xu, J. *et al.* Elucidating anionic oxygen activity in lithium-rich layered oxides. *Nat. Commun.* **9,** 947. doi:10.1038/s41467-018-03403-9 (2018).

25. Armstrong, A. R. *et al.* Demonstrating oxygen loss and associated structural reorganization in the lithium battery cathode Li[$Ni_{0.2}Li_{0.2}Mn_{0.6}$]O_2. *J. Am. Chem. Soc.* **128,** 8694–8698. doi:10.1021/ja062027+ (2006).

26. Gauthier, M. *et al.* Electrode-electrolyte interface in Li-ion batteries: current understanding and new insights. *J. Phys. Chem. Lett.* **6,** 4653–4672. doi:10.1012/acs.jpclett.5b01727 (2015).

27. Manthiram, A., Knight, J. C., Myung, S.-T., Oh, S.-M. & Sun, Y.-K. Nickel-rich and lithium-rich layered oxide cathodes: progress and perspectives. *J. Electrochem. Soc.* **6,** 1501010. doi:10.1002/aenm.201501010 (2016).

28. Yabuuchi, N., Yoshii, K., Myung, S.-T., Nakai, I. & Komaba, S. Detailed studies of a high-capacity electrode material for rechargeable batteries, Li_2MnO_3–$LiCo_{1/3}Ni_{1/3}Mn_{1/3}O_2$. *J. Am. Chem. Soc.* **133,** 4404–4419. doi:10.1021/ja108588y (2011).

29. Renfrew, S. E. & McCloskey, B. D. Residual lithium carbonate predominantly accounts for first cycle CO_2 and CO outgassing of Li-stoichiometric and Li-rich layered transition-metal oxides. *J. Am. Chem. Soc.* **139,** 17853–17860. doi:10.1021/jacs.7b08461 (2017).

30. Renfrew, S. E. & McCloskey, B. D. Quantification of surface oxygen depletion and solid carbonate evolution on the first cycle of $LiNi_{0.6}Mn_{0.2}Co_{0.2}O_2$ electrodes. *ACS Appl. Energy. Mater.* **2,** 3762–3772. doi:10.1021/acsaem.9b00459 (2019).

31. Ramakrishnan, S., Park, B., Wu, J., Yang, W. & McCloskey, B. D. Extended interfacial stability through simple acid rinsing in a Li-rich oxide cathode material. *J. Am. Chem. Soc.* **142,** 8522–8531. doi:10.1021/jacs.0c02859 (2020).

32. Gowda, S. R., Brunet, A., Wallraff, G. M. & McCloskey, B. D. Implications of CO_2 contamination in rechargeable nonaqueous Li–O_2 batteries. *J. Phys. Chem. Lett.* **4,** 276–279. doi:10.1021/acsaem.9b00459 (2013).

33. Mahne, N., Renfrew, S. E., McCloskey, B. D. & Freunberger, S. A. Electrochemical oxidation of lithium carbonate generates singlet oxygen. *Angew. Chem. Int. Ed.* **57,** 5529–5533. doi:10.1002/anie.201802277 (2018).

34. Freiberg, A. T. S., Roos, M. K., Wandt, J., de Vivie-Riedle, R. & Gasteiger, H. A. Singlet oxygen reactivity with carbonate solvents used for Li-ion battery electrolytes. *J. Phys. Chem. A* **122,** 8828–8839. doi:10.1021/acs.jpca.8b08079 (2018).

35. Bryantsev, V. S. & Blanco, M. Computational study of the mechanisms of superoxide-induced decomposition of organic carbonate-based electrolytes. *J. Phys. Chem. Lett.* **2,** 379–383. doi:10.1021/jz1016526 (2011).

36. Freiberg, A. T. S., Sicklinger, J., Solchenbach, S. & Gasteiger, H. A. Li_2CO_3 decomposition in Li-ion batteries induced by the electrochemical oxidation of the electrolyte and of electrolyte impurities. *Electrochim. Acta* **346,** 136271. doi:10.1016/j.electacta.2020.136271 (2020).

37. Renfrew, S. E., Kaufman, L. A. & McCloskey, B. D. Altering surface contaminants and defects influences the first-cycle outgassing and irreversible transformations of $LiNi_{0.6}Mn_{0.2}Co_{0.2}O_2$. *ACS Appl. Mater. Interfaces* **11,** 34913–39421. doi:10.1021/acsami.9b09992 (2019).

38. Santhanam, R. & Rambabu, B. Improved high rate cycling of Li-rich $Li_{1.10}Ni_{1/3}Co_{1/3}Mn_{1/3}O_2$ cathode for lithium batteries. *Int. J. Electrochem. Sci.* **4,** 1770–1778 (2009).

39. Nam, K.-M., Kim, H.-J., Kang, D.-H., Kim, Y.-S. & Song, S.-W. Ammonia-free coprecipitation synthesis of a Ni-Co-Mn hydroxide precursor for high-performance battery cathode materials. *Green Chem.* **17,** 1127–1135. doi:10.1039/c4gc01898b (2015).

40. Cao, X. *et al.* Synthesis and characterization of $LiNi_{1/3}Co_{1/3}Mn_{1/3}O_2$ as cathode materials for Li-ion batteries via an efficacious sol-gel method. *Int. J. Electrochem. Sci.* **11,** 5267–5278. doi:10.20964/2016.06.93 (2016).

41. Zhang, Y. *et al.* Revealing electrolyte oxidation via carbonate dehydrogenation on Ni-based oxides in Li-ion batteries by in situ Fourier transform infrared spectroscopy. *Energy Environ. Sci.* **13,** 183–199. doi:10.1039/C9EE02543J (2020).

42. Jung, R. *et al.* Effect of ambient storage on the degradation of Ni-rich positive electrode materials (NMC811) for Li-ion batteries. *J. Electrochem. Soc.* **165,** A132–A141. doi:10.1149/2.0401802jes (2018).

43. Hatsukade, T., Schiele, A., Hartmann, P., Brezesinski, T. & Janek, J. Origin of carbon dioxide evolved during cycling of nickel-rich layered NCM cathodes. *ACS Appl. Mater. Interfaces* **10,** 38892–38899. doi:10.1021/acsami.8b13158 (2018).

44. Houchins, G., Pande, V. & Viswanathan, V. Mechanism for singlet oxygen production in Li-ion and metal-air batteries. *ACS Energy Lett.* **5,** 1893–1899. doi:10.1021/acsenergylett.0c00595 (2020).

45. Qiu, B. *et al.* Gas–solid interfacial modification of oxygen activity in layered oxide cathodes for lithium-ion batteries. *Nat. Commun.* **7,** 12108. doi:10.1038/ncomms12108 (2016).

46. Zhu, Z. *et al.* Gradient Li-rich oxide cathode particles immunized against oxygen release by a molten salt treatment. *Nat. Energy* **4,** 1049–1058. doi:10.1038/ncomms12108 (2019).

47. Cooper, S. Mixed indicator bromocresol green-methyl red for carbonates in water. *Ind. Eng. Chem. Anal. Ed.* **13,** 466–470. doi:10.1021/i560095a011 (1941).

48. Rana, J. *et al.* Quantifying the capacity contributions during activation of Li_2MnO_3. *ACS Energy Lett.* **5,** 634–641. doi:10.1021/acsenergylett.9b02799 (2020).

49. Guerrini, N. *et al.* Charging mechanism of Li_2MnO_3. *Chem. Mater.* **32,** 3733–3740. doi:10.1021/acs.chemmater.9b04459 (2020).

50. Zhuo, Z. *et al.* Cycling mechanism of Li_2MnO_3: Li-CO_2 batteries and commonality on oxygen redox in cathode materials. *Joule* **5,** 975–997. doi:10.1016/j.joule.2021.02.004 (4 2021).

51. Kim, J.-H., Ryu, H.-H., Kim, S. J., Yoon, C. S. & Sun, Y.-K. Degradation mechanism of highly Ni-rich $Li[Ni_xCo_yMn_{1-x-y}]O_2$ cathodes with x ¿ 0.9. *ACS Appl. Mater. Interfaces* **11,** 30926–30942. doi:10.1021/acsami.9b09754 (2019).

52. Kim, U.-H., Kuo, L.-Y., Kaghazchi, P., Yoon, C. S. & Sun, Y.-K. Quaternary layered Ni-rich NCMA cathode for lithium-ion batteries. *ACS Energy Lett.* **4,** 576–582. doi:10.1021/acsenergylett.8b02499 (2019).

53. Zhu, Z. *et al.* Optimizing the interface engineering and structural stability of nickel-rich layered oxide cathode by dual-function modification. *Chem. Eng. J.* **430,** 132908. doi:10.1016/j.cej.2021.132908 (2022).

54. Ryu, H.-H. *et al.* A highly stabilized Ni-rich NCA cathode for high-energy lithium-ion batteries. *Mater. Today* **36,** 73–82. doi:10.1016/j.mattod.2020.01.019 (2020).

55. Li, X. *et al.* Removing lithium residues via H_2BO_3 washing and concurrent in-situ formation of a lithium reactive coating on Ni-rich cathode materials towards enhanced electrochemical performance. *Electrochim. Acta* **406.** doi:10.1016/j.electacta.2022.139879 (2022).

56. Chen, J., Wang, X. L., Jin, E. M., Moon, S.-G. & Jeong, S. M. Optimization of B_2O_3 coating process for NCA cathodes to achieve long-term stability for application in lithium ion batteries. *Energy J.* **222.** doi:10.1016/j.energy.2021.119913 (2021).

57. Kaufman, L. A. & McCloskey, B. D. Surface lithium carbonate influences electrolyte degradation via reactive oxygen attack in lithium-excess cathode materials. *Chem. Mater.* **33,** 4170–4176. doi:10.1021/acs.chemmater.1c00935 (2021).

58. Yan, P. *et al.* Intragranular cracking as a critical barrier for high-voltage usage of layer-structured cathode for lithium-ion batteries. *Nat. Commun.* **8.** doi:10.1038/ncomms14101 (2017).

59. Ahmed, S. *et al.* The role of intragranular nanopores in capacity fade of nickel-rich layered $Li(Ni_{1-x-y}Co_xMn_y)O_2$ cathode materials. *ACS Nano* **13,** 10694–10704. doi:10.1021/acsnano.9b05047 (2019).

60. Seo, D.-H. *et al.* The structural and chemical origin of the oxygen redox activity in layered and cation-disordered Li-excess cathode materials. *Nat. Chem.* **8,** 692–697. doi:10.1038/nchem.2524 (2016).

61. Yan, P. *et al.* Coupling of electrochemically triggered thermal and mechanical effects to aggravate failure in a layered cathode. *Nat. Commun.* **9.** doi:10.1038/s41467-018-04862-w (2018).

62. Lebens-Higgins, Z. W. *et al.* Revisiting the charge compensation mechanisms in $LiNi_{0.8}Co_{0.2-y}Al_yO_2$ systems. *Mater. Horiz.* **6,** 2112–2123. doi:10.1039/c9mh00765b (2019).

63. Li, J., Downie, L. E., Ma, L., Qiu, W. & Dahn, J. R. Study of the failure mechanisms of $LiNi_{0.8}Mn_{0.1}Co_{0.1}O_2$ cathode material for lithium ion batteries. *J. Electrochem. Soc.* **162,** A1401–A1408. doi:10.1149/2.1011507jes (2015).

64. Oswald, S., Bock, M. & Gasteiger, H. A. Elucidating the implications of morphology on fundamental characteristics of nickel-rich NCMs: cracking, gassing, rate capability, and thermal stability of poly- and single-crystalline NCM622. *J. Electrochem. Soc.* **169.** doi:10.1149/1945-7111/ac5f7f (2022).

65. Hu, J. *et al.* Locking oxygen in lattice: a quantifiable comparison of gas generation in polycrystalline and single crystal Ni-rich cathodes. *Energy. Storage Mater.* **47,** 195–202. doi:10.1016/j.ensm.2022.02.025 (2022).

66. Qian, G. *et al.* Single-crystal nickel-rich layered-oxide battery cathode materials: synthesis, electrochemistry, and intra-granular fracture. *Energy. Storage Mater.* **27,** 140–149. doi:10.1016/j.ensm.2020.01.027 (2020).

67. You, B. *et al.* Research progress of single-crystal nickel-rich cathode materials for lithium ion batteries. *Small Methods* **5.** doi:10.1002/smtd.202100234 (2021).